Uncertainty Quantification of Tightly Integrated LiDAR/IMU Localization Algorithms

Ali Hassani

Dissertation submitted to the Faculty of the
Virginia Polytechnic Institute and State University
in partial fulfillment of the requirements for the degree of

Doctor of Philosophy
in
Aerospace Engineering

Mathieu Joerger, Chair
Mark L. Psiaki
Craig Woolsey
Hesham A. Rakha

May 2, 2023
Blacksburg, Virginia

Keywords: LiDAR/IMU Integration, Data Association, Integrity Risk Evaluation

Uncertainty Quantification of Tightly Integrated LiDAR/IMU Localization Algorithms

Ali Hassani

(ABSTRACT)

Safety risk evaluation is critical in autonomous vehicle applications. This research aims to develop, implement, and validate new safety monitoring methods for navigation in Global Navigation Satellite System (GNSS)-denied environments. The methods quantify uncertainty in sensors and algorithms that exploit the complementary properties of light detection and ranging (LiDAR) and inertial measuring units (IMU). This dissertation describes the following four contributions. First, we focus on sensor augmentation for landmark-based localization. We develop new IMU/LiDAR integration methods that guarantee a bound on the integrity risk, which is the probability that the navigation error exceeds predefined acceptability limits. IMU data improves LiDAR position and orientation (pose) prediction and LiDAR limits the IMU error drift over time. In addition, LiDAR return-light intensity measurements improve landmarks recognition. As compared to using the sensors individually, tightly-coupled IMU/LiDAR not only increases pose estimation accuracy but also reduces the risk of incorrectly associating perceived features with mapped landmarks. Second, we consider algorithm improvements. We derive and analyze a new data association method that provides a tight bound on the risk of incorrect association for LiDAR feature-based localization. The new data association criterion uses projections of the extended Kalman filter's (EKF) innovation vector rather than more conventional innovation vector norms. This method decreases the integrity risk by improving our ability to predict the risk of incorrect association. Third, we depart from landmark-based approaches. We develop a spherical grid-based localization method that

leverages quantization theory to bound navigation uncertainty. This method is integrated with an iterative EKF to establish an analytical bound on the vehicle's pose estimation error. Unlike landmark-based localization which requires feature extraction and data association, this method uses the entire LiDAR point cloud and is robust to extraction and association failures. Fourth, to validate these methods, we designed and built two testbeds for indoor and outdoor experiments. The indoor testbed includes a sensor platform installed on a rover moving on a figure-eight track in a controlled lab environment. The repeated figure-eight trajectory provides empirical pose estimation error distributions that can directly be compared with analytical error bounds. The outdoor testbed required another set of navigation sensors for reference truth trajectory generation. Sensors were mounted on a car to validate our algorithms in a realistic automotive driving environment.

Uncertainty Quantification of Tightly Integrated LiDAR/IMU Localization Algorithms

Ali Hassani

(GENERAL AUDIENCE ABSTRACT)

Advances in computing and sensing technologies have enabled large scale demonstrations of autonomous vehicle operations including pilot programs for self-driving cars on public roads. However, a key question that has yet to be answered is about how safe these vehicles really are. "Autonomously" driving millions of miles (with a trained safety driver taking over control to prevent potential collisions) is insufficient to prove fatality rates matching human performance, i.e., lower than 1 per 100,000,000 miles driven. The safety of an autonomous vehicle depends on the safety of its individual subsystems, components, connected infrastructure, etc. In this research, we evaluate the safety of the navigation subsystem which uses sensor information to determine the vehicle's location and orientation. We focus on light detection and ranging (LiDAR)and inertial measuring units (IMU). A LiDAR provides a point cloud representation of the environment by measuring distances to surrounding objects using beams of infrared light (laser beams) sent at regular angular intervals. An IMU measures the acceleration and angular velocity of the vehicle. We assume that a map of the environment is available. In the first part of this research, we extract recognizable objects from the LiDAR point cloud and match them with those in the map: this process helps estimate the vehicle's position and orientation. We identify the process' limitations that include incorrectly matching sensed and mapped landmarks. We develop new methods to quantify their impacts on localization errors, which we then reduce by incorporating additional IMU data. In the second part of this dissertation, we design and evaluate a new approach specifically aimed at provably increasing

confidence in landmark matching, thereby improving vehicle navigation safety. Third, instead of isolating individual landmarks, we use the LiDAR point cloud as a whole and match it directly with the map. The challenge with this approach was in efficiently and accurately quantifying the confidence that can be placed in the vehicle's navigation solution. We tested these navigation methods using experimental data collected in a controlled lab environment and in a real-world scenario.

Dedication

I dedicate my dissertation work to my family. A special feeling of gratitude to my loving parents, Abbasali and Masoumeh Hassani whose words of encouragement and their endless love brought the infinite power of light to darkness. My sister Maryam and my brother-in-law Iman have never left my side and always believed in me and are very special. Finally, I dedicate this work to myself for completing a seven and a half years journey with everyday hard work and not giving up when it was the most feasible option.

Acknowledgments

I would like to express my deepest appreciation to my advisor and chair of the committee Dr. Mathieu Joerger for his guidance and patience. I also would like to express my profound gratitude to Professor Mark L. Psiaki who generously shared his Knowledge and expertise with me. Additionally, I'm extremely grateful to Professors Craig Woolsey and Hesham A. Rakha for their constructive feedback and criticisms which improved the quality of this work. I sincerely thank the National Science Foundation (NSF) and the NSF program directors Dr. Jordan Berg and Dr. Irina Dolinskaya for sponsoring parts of this work.

I am also thankful to my colleagues, especially Danielle Racelis and Sandeep K. Jada, for their moral support and inspiration. Thanks should also go to Jaeyeok Kim, Casey Smith, and Brandon Medellin for their assistance in conducting experiments.

Lastly, I would be remiss in not mentioning my family, especially my parents and sister. Their belief in me has kept my spirits and motivation high during this process. I would also like to thank my partner Lindsey Kingrey for all the practical and emotional support.

Contents

List of Figures xiii

List of Tables xviii

1 Dissertation Introduction 1

1.1 Navigation Safety for Autonomous Vehicles 1

1.2 Navigation in GNSS-denied Environments 2

1.3 Gaps in Uncertainty Quantification for LiDAR/IMU Localization 3

1.3.1 Data association in landmark-based localization 3

1.3.2 Grid-based localization 3

1.3.3 PC matching localization 4

1.4 Research Objectives 4

1.4.1 Leveraging additional data to improve data association 6

1.4.2 Deriving new algorithms to improve data association 7

1.4.3 Avoiding data association altogether by exploring PC-matching and grid-based methods 7

1.5 Manuscript Format Dissertation 7

1.6 Summary of Manuscripts and Research Contributions 8

1.6.1 Measurement-level IMU/LiDAR integration. 9
1.6.2 Indoor experimental validation of tightly integrated IMU/LiDAR. 9
1.6.3 Data association using innovation projections. 9
1.6.4 LiDAR spherical grid-based localization and quantization theory to bound navigation uncertainty. 9
1.6.5 Outdoor experimental validation of tightly integrated IMU/LiDAR. 10

2 Analytical and Empirical Navigation Safety Evaluation of Tightly-Integrated LiDAR/IMU Using Return-Light Intensity 11

2.1 Introduction for Landmark-Based IMU/LiDAR Localization Integrity 12
2.2 High-Integrity IMU and LiDAR Measurement Models 15
2.2.1 IMU measurement equations 15
2.2.2 LiDAR range and bearing angle measurement equations 16
2.2.3 Linearization and discretization of IMU and LiDAR equations 21
2.3 Integrated LiDAR/IMU Estimation Process 23
2.3.1 EKF initialization and IMU-based pose prediction process 24
2.3.2 Data association criterion and EKF measurement update 26
2.3.3 Integrity risk bound 30
2.4 Integrity Risk Evaluation Using Simulated Data 32
2.4.1 Covariance analysis and integrity risk bound (analytical vs direct simulation) 33

2.5 Experimental Integrity Risk Evaluation 35
2.5.1 Experimental testbed 35
2.5.2 Using LiDAR range, bearing, intensity and IMU measurements 38
2.5.3 Repeated trajectories 39
2.6 Conclusion for Landmark-Based IMU/LiDAR Localization Integrity 41

3 A New Data Association Method Using Kalman Filter Innovation Vector Projections 43

3.1 Introduction for Data Association Using Innovation Projections 44
3.2 Prior Work on Navigation Integrity Evaluation Using Normalized Innovations Squared 49
3.2.1 Data association using NIS 49
3.2.2 One-dimensional two-target DA example using NIS 51
3.2.3 Example application: integrity risk bound using NIS 53
3.3 A New Approach Using Innovation Vector Projections 55
3.3.1 New data association criteria using IP 55
3.3.2 Analytical bound on the probability of CA using IP 56
3.3.3 One-dimensional two-target DA example using IP 61
3.4 Risk Bound Analysis Using Simulated Data 62
3.5 Testing and Performance Analysis 64
3.6 Conclusion for Data Association Using Innovation Projections 67

4 Spherical Grid-Based IMU/LiDAR Localization and Uncertainty Evaluation Using Signal Quantization **69**

4.1 Introduction to Spherical Grid-Based IMU/LiDAR Localization 70

4.2 Spherical Gridding Using Signal Quantization 72

4.2.1 Quantization theory 72

4.2.2 Spherical grid design 75

4.2.3 Quantization error 77

4.2.4 Applying a spherical grid to the map 78

4.3 Localization and Analytical Uncertainty Quantification 79

4.3.1 Vehicle linearized state propagation model 80

4.3.2 Measurement models 82

4.3.3 Model-based estimator design 84

4.3.4 Pose error due to quantization 86

4.4 Experimental Evaluation of Spherical Grid-Based Localization 88

4.4.1 Indoor testing for experimental validation in a structured environment . 89

4.4.2 Outdoor testing in a realistic automotive environment 93

4.5 Conclusion for Spherical Grid-Based IMU/LiDAR Localization 98

5 Conclusions and Future Work **100**

5.1 Dissertation Conclusion 100

5.2 Summary of Achievements 101

5.3 Future Work 102

Bibliography **105**

Appendices **120**

A - IMU and LiDAR Measurements and Coefficients 121

B - Discrete-Time Equations of IMU 122

C - Overbounding of Measurement Error Distributions 125

D - LiDAR intensity measurements distribution 127

E - Time evolution of biases and estimator coefficients 129

List of Figures

1.1 LiDAR Localization research graph (contributions of the research are highlighted in blue). 6

2.1 LiDAR point cloud showing return-light intensity (color-coded from blue to red, from low intensity to high intensity). 17

2.2 (a) 3D segmentation of LiDAR point cloud - (b) circle fitting and point-feature measurement extraction 18

2.3 LiDAR/IMU integration block diagram (prediction, estimation, and integrity risk evaluation processes). 24

2.4 Initialization and EKF prediction process using IMU 25

2.5 Data Association and KF estimation processes using LiDAR 26

2.6 ADS positioning error covariance ellipses using LiDAR-Only and IMU/LiDAR for a two-Landmark scenario 33

2.7 Lateral positioning integrity risk using LiDAR-Only and IMU/LiDAR for a two-landmark scenario: analytical bound versus Monte-Carlo (MC) simulations over 50,000 trials. 34

2.8 Automated testbed setup with sensor platform repeatedly moving on a figure-Eight track. 37

2.9 (a) IR Camera; (b) IR markers on sensor platform; (c) LiDAR -VLP-16 Puck; (d) IMU-IGM-A1 37

2.10 Covariance ellipses using IMU/LiDAR with intensity measurements 39

2.11 Integrity risk bounds using LiDAR-Only versus LiDAR+, IMU/LiDAR, IMU/LiDAR + ... 40

2.12 Cross track error of ADS for a hundred laps 41

3.1 Illustrative one-dimensional example of a sensor (at location x in reference $\boldsymbol{R}$) providing observations to two landmarks (at locations p_A and p_B). Sensor to landmark measurements are noted z_1 and z_2. 52

3.2 Two-dimensional normalized innovation-space representation of the association process. The ratio of blue-and-cyan samples over the total number of samples is the actual probability of correct association (CA). Only cyan samples are accounted for in the NIS lower-bound on the probability of CA. 52

3.3 Integrity risk for automotive applications. The integrity risk is the probability of the car being outside the alert limit requirement box (blue shaded area) when it was estimated to be inside the box. When the lateral deviation is of primary concern, then the alert limit is the distance l between the edge of the car and the edge of the lane. 53

3.4 Three-dimensional normalized innovation-space representation of the association process. The ratio of blue-and-cyan samples over the total number of samples is the actual probability of correct association (CA). Only cyan samples are accounted for in the NIS lower-bound on the probability of CA, whereas both blue and cyan samples are accounted for using IP. A few maroon data points (bottom left of the sample ball) are double-counted using the IP bound. 61

3.5 Vehicle and landmark positioning covariance analysis Using LiDAR/IMU in EKF-based simultaneous localization and mapping (SLAM) for the two-Landmark scenario. 63

3.6 Integrity risk bounds using NIS versus IP-based data association for the two-landmark scenario. 65

3.7 Testbed setup (VICON cameras at the ceiling are not shown). 66

3.8 Estimated trajectory and covariance ellipses Using LiDAR/IMU. 68

3.9 Integrity risk bounds for the NIS versus IP data association criteria using LiDAR/IMU. 68

4.1 Scalar quantizer parameters 73

4.2 LiDAR scanned and quantized range measurements 75

4.3 Quantizer parameter definition for LiDAR range vs. bearing angle measurements 76

4.4 LiDAR scan and quantized signals (at 0-degree elevation; other elevation bins are not shown for clarity of exposition, but are quantized using the same process.) 77

4.5 Quantization error and error bound for 360-degree measurements 78

4.6 Applying the spherical grid to the map and selecting the points 79

4.7 IEKF spherical grid-based localization diagram 85

4.8 Indoor testbed overview 89

4.9 IEKF spherical grid-based localization performance for a single lap estimation of rover position 91

4.10 IEKF spherical grid-based localization errors and error bounds for the rover's (a) cross-track and (b) heading angle estimation performance 92

4.11 Outdoor test equipment overview 94

4.12 Three-dimensional point cloud map used in the outdoor experiment 96

4.13 LiDAR/IMU-based IEKF spherical grid-based vehicle localization performance during testing in an outdoor environment 97

4.14 IEKF spherical grid-based localization error bounds for the vehicle (a) cross-track positioning error (b) heading angle estimation error estimation 98

C.1 Quantile-to-Quantile Plots of the LiDAR PC's Extracted Feature Error Distribution and Gaussian Overbounding Model for the (a) Range Measurement (b) Bearing Angle Measurement (4250 data points) 126

D.1 Intensity Measurement Error Distribution and Gaussian Overbounding Model for the Retro-Reflective Surface with a 70-Degree Incidence Angle (17,500 data points) 127

D.2 Mean and Overbounding Standard Deviations ($\pm 1\sigma$ and $\pm 3\sigma$) of Intensity Measurements for Black, White and Retro-Reflective Surfaces at 0-Degree, 30-Degree, and 70-Degree Incidence Angles (total of 166,334 data points, approximately 18,480 data points per configuration over the nine configurations) 128

E.1 Time variation of biases coefficients for the first three timesteps 130

E.2 Impact of previous and current quantization biases on IEKF SGL analytical cross track error bound 130

E.3 Copmarison of the impact of quantization biases on IEKF SGL analytical cross track error bound 131

List of Tables

2.1 LiDAR and IMU simulation settings 32

2.2 LiDAR and IMU parameters and test settings 36

3.1 LIDAR and IMU simulation parameters 64

3.2 Test settings and parameters 67

4.1 Indoor experiment settings 90

4.2 Comparison of the 16%-to-84% quantile deviation bounds in cross-track and computation times over a single lap for three different localization algorithms. . 93

4.3 Outdoor experiment settings 95

List of Abbreviations

ADS	Autonomous Driving System
BF	Brute Force
CA	Correct Association
CDF	Cumulative Distribution Function
DA	Data Association
EKF	Extended Kalman Filter
FE	Feature Extraction
GMP	Gauss Markov Process
GMRP	Gauss Markov Random Process
GNSS	Global Navigation Satellites System
HMI	Hazardously Misleading Information
IA	Incorrect Association
IEKF	Iterative Extended Kalman Filter
IMU	Inertial Measurement Unit
IP	Innovation Projection
IR	Infra red

JPDA Joint Probabilistic Data Association

LiDAR Light Detection And Ranging

LL Landmark-based Localization

LNN Local Nearest Neighbor

MC Monte Carlo

NIS Normalized Innovation Squared

OGM Occupancy Grid Map

PC Point cloud

PDF Probability Density Function

PHD Probability Hypothesis Density

PIA Propability of Incorrect Association

Pose Position and orientation

RFS Random Finite Set

SGL Spherical Grid-based Localization

WA Wrong Association

Chapter 1

Dissertation Introduction

1.1 Navigation Safety for Autonomous Vehicles

Localization is a key functionality of autonomous vehicles: when traveling from point 'A' to point 'B', an autonomous vehicle must localize itself accurately, continuously, and with high confidence. In safety-critical applications such as general aviation and autonomous driving, uncertainty quantification of localization algorithms is crucial [Pullen and Joerger (2020)].

Rigorous uncertainty quantification is achieved and implemented in Global Navigation Satellite System (GNSS)-based aviation navigation, where safety is assessed in terms of integrity. Integrity is a measure of trust in sensor information [International Civil Aviation Organization (2006)]. Unfortunately, aviation safety methods do not directly apply to autonomous driving systems because ground vehicles operate in sky-obstructed areas where GNSS signals can be altered or blocked by buildings and trees. This research focuses on the design of navigation uncertainty quantification algorithms for autonomous driving systems in GNSS-denied environments. The objective is to expand uncertainty quantification and integrity evaluation methods to non-GNSS-based navigation.

1.2 Navigation in GNSS-denied Environments

GNSS-denied navigation requires sensors such as inertial measuring unit (IMU), light detection and ranging (LiDAR), camera, and RADAR. Their measurements can be combined in advanced navigation algorithms to determine absolute vehicle pose (position and orientation) using a pre-established map. This research focuses on LiDAR and IMU because of their prevalence in autonomous driving systems. We assume that an a-priori map is available in the form of a detailed point cloud (PC) or of a parametric representation of geometric features (planes for walls, cylinders for lamp poles, etc.).

There are three main categories of map-based LiDAR localization algorithms. (a) *Landmark-based methods* require feature extraction (FE) to recognize landmarks, and data association (DA) to assign the observed landmarks with the corresponding mapped landmarks. (b) *Grid-based methods* represent the PC's spatial information in a probabilistic and tessellated format. (c) *Scan-matching or PC-matching methods*, including the widely-implemented iterative closest point (ICP) algorithm, which matches successive three-dimensional (3D) PCs over time.

Once a data grid is obtained in (b), matching or correlation operations are need to determine vehicle displacement over time or vehicle pose in map. The algorithm developed in this dissertation will combine elements of (b) and (c).

If, for any algorithm categories (a), (b), or (c), one could rigorously predict the impact of sensor and algorithm errors on localization uncertainty, then reliable, high-integrity localization in GNSS-denied areas becomes possible.

1.3 Gaps in Uncertainty Quantification for LiDAR/IMU Localization

LiDAR-based localization methods are prone to algorithmic faults in cluttered environments and in the presence of sensor uncertainty. Localization uncertainty quantification methods present the following major research gaps if they are to be employed in safety-critical applications.

1.3.1 Data association in landmark-based localization

Multi-target tracking methods can be used to evaluate the probability of correct association in LiDAR localization. However, such methods are not suitable for safety-critical applications because they rely on approximations rather than rigorous bounds, they are computationally expensive, and they lack the risk-prediction capability that is key to deciding whether or not to proceed with or abort a safety-critical operation. High-integrity LiDAR localization methods developed in prior work [Joerger et al. (2016)] provide an upper bound for the risk of wrong association but this bound is either too large due to insufficient sensor information, or too loose due to overly-conservative approximations.

1.3.2 Grid-based localization

There are no rigorous analytical methods to determine grid-based pose estimation error distribution. In particular, to our knowledge, there is no efficient way to rigorously but tightly bound localization errors when the sensed information is captured in a finite number of grid cells.

1.3.3 PC matching localization

PC-matching methods are computationally expensive, especially using new LiDAR technology which provides hundreds of thousands of data points over a fraction of a second. There are no rigorous analytical methods to compute the pose error distribution for PC matching algorithms. Sensed and mapped PCs are challenging to match because LiDAR beams on moving vehicles do not hit the same point twice.

1.4 Research Objectives

LiDAR-based navigation is an active research area that builds upon LiDAR-specific localization methods as well as other algorithms that were originally intended for vision-based and RADAR-based navigation. The diagram in Figure 1.1 describes the main steps of LiDAR localization for two major families of methods (gray background), highlights the steps we implemented (black font color), and emphasizes the steps we researched with a strong focus on uncertainty quantification (blue boxes).

The process starts with the segmentation of the raw LiDAR PC. In this research, PC segmentation is used to distinguish stationary from moving objects [Rangesh and Trivedi (2019); Han et al. (2012); Dewan et al. (2016); Postica et al. (2016)]. Moving objects are excluded upfront to focus on navigation using stationary landmarks (rather than collision avoidance).

We classify LiDAR navigation methods into two main families of algorithms represented with gray backgrounds in Figure 1.1: landmark-based localization (LBL) and PC or grid-matching localization. In LBL, we extract features from segmented points of stationary objects. A single landmark typically has multiple measurable features including, for example, the position coordinates of a characteristic point (e.g., the intersection of a cylindrical lamp pole's axis with

the ground plane), or its mean surface light-return reflectivity. In the next step, we compare these extracted features either individually with the "closest" mapped features, or as a set with a subset of mapped features.

- *Individual Landmark Matching.* Gating and selection are used to match a sensed feature with its nearest neighbor in the map.
- *Landmark Set Matching.* Subsets of sensed and mapped landmark features are matched, which narrows down the matching process to find a corresponding landmark combination and ordering.

The first approach may be more intuitive, but the impacts of gating on localization integrity and continuity are difficult to quantify and existing algorithms must make heuristic choices when multiple sensed landmarks fall into a mapped landmark's validation gate [Arana et al. (2020); Hafez et al. (2020)]. The second approach is adopted in this research.

Consistency checks between mapped and measured features are crucial [Joerger et al. (2018)]. If the number of mapped and measured features is inconsistent, we have two options. First, send an alarm and terminate the operation. Second, in the set-based approach, consider all possible combinations between the two sets and all possible ordering permutations between matched-size sets. This process is performed as a part of the blue data association block in Figure 1.1.

Chapters 2 and 3 of this dissertation develop new methods to quantify and bound localization performance when matching is imperfect. Chapters 2 and 3 also evaluate sensor augmentation and algorithm refinement to reduce LBL error bounds. However, feature extraction (FE) and data association (DA) remain major sources of uncertainty in LBL. To address this issue, in Chapter 4, we investigate a grid-matching approach that does not require FE and DA (also highlighted in blue in Figure 1.1). No rigorous analytical method is available to quantify the

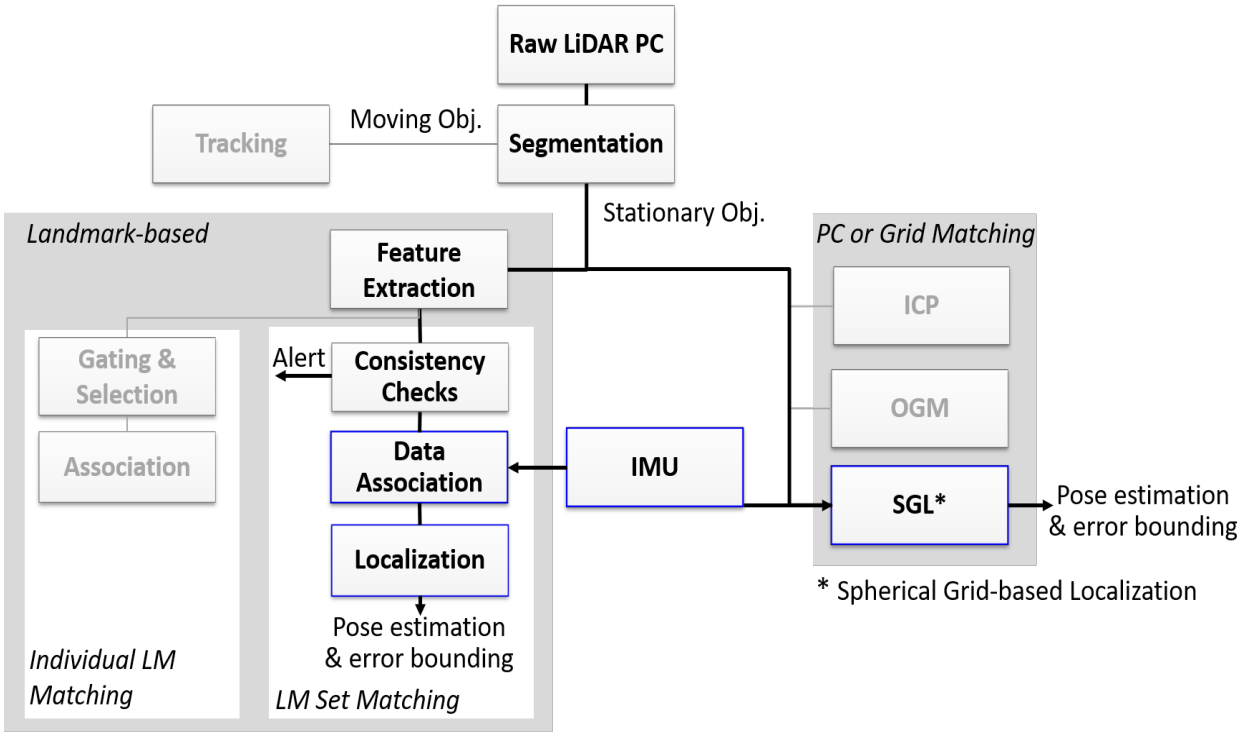

Figure 1.1: LiDAR Localization research graph (contributions of the research are highlighted in blue).

uncertainty of such a method. Therefore, we develop a novel spherical grid-based localization (SGL) algorithm that enables both localization and analytical uncertainty quantification. The algorithm leverages classical model-based filtering techniques, introduces a LiDAR PC gridding approach, and adapts quantization theory intended for signal processing to LiDAR localization.

In this dissertation, the following three major objectives are pursued:

1.4.1 Leveraging additional data to improve data association

This research aims at quantifying the reduction in LiDAR localization integrity risk provided by additional measurements. Specifically, IMU data can not only enhance pose prediction

but also reduce the risk of wrong associations. LiDAR return-light intensity measurements can also improve DA performance. This improvement must be evaluated analytically, in simulations, and to the extent possible, experimentally.

1.4.2 Deriving new algorithms to improve data association

Multi-target tracking algorithms in space and aeronautical applications use normalized innovation squared (NIS)-based methods to perform DA, i.e., to decide which currently-sensed object corresponds to a previously observed object. When predicting DA risks for safety-critical navigation, the NIS criterion causes loose risk bounds. This research explores new, non-NIS-based approaches to performing DA.

1.4.3 Avoiding data association altogether by exploring PC-matching and grid-based methods

Grid-based and matching algorithms do not require the fault-prone process of DA. However, analytical uncertainty quantification has yet to be developed and analyzed. The third objective of this dissertation is to design grid-based and/or PC-matching algorithms, or a combination thereof, specifically to enable risk assessment in LiDAR localization.

1.5 Manuscript Format Dissertation

This dissertation is presented in the Virginia Tech Graduate Schools manuscript format. In addition to the standard or traditional format for dissertations and theses, the Virginia Tech Graduate School accepts this alternative manuscript format. The manuscript thesis/disser-

tation format allows the incorporation of a students articles, book chapters, and the like to replace some of the standard chapters. Prior publication of the manuscript(s) is not a requirement for using this format. The following guidelines apply: At least one manuscript (i.e., article, chapter) is required for the Masters degree or at least two manuscripts for the Doctoral degree. The manuscript(s) should be based on research done at Virginia Tech. The manuscript(s) can be previously published, to be published, or in preparation for submission. The graduate student is the major contributor and writer of the manuscript(s), as usually represented by the sole author. In the case of multiple authorship, the contribution of each author is detailed in the Introduction or separate Attribution section.

1.6 Summary of Manuscripts and Research Contributions

This dissertation includes three manuscripts.

- Paper #1: "Analytical and Empirical Navigation Safety Evaluation of Tightly-Integrated LiDAR/IMU Using Return-Light Intensity".
- Paper #2: "A New Data Association Method Using Kalman Filter Innovation Vector Projections".
- Paper #3: "Spherical Grid-Based IMU/LiDAR Localization and Uncertainty Evaluation Using Signal Quantization".

These manuscripts are supported by conference publications not included in the dissertation for the sake of brevity.

The main contributions of this research can be described as follows:

1.6.1 Measurement-level IMU/LiDAR integration.

A novel landmark-based localization algorithm that integrates LiDAR ranging and angular measurements with IMU and LiDAR return-light intensity data was designed to improve data association and reduce integrity risk (Chapter 2).

1.6.2 Indoor experimental validation of tightly integrated IMU/LiDAR.

An automated sensor safety evaluation testbed was built and implemented to quantify the impacts on integrity risk of landmark occlusions and landmark surface properties. The testbed provides a means to analyze the localization systems performance while collecting a statistically significant number of data points over repeated trajectories in an indoor controlled environment (Chapter 2).

1.6.3 Data association using innovation projections.

A new data association method using the projections of the extended Kalman filter innovation vector was developed. As compared to conventional normalized innovation squared approaches, the new criterion provides a tighter bound on the risk of incorrect associations as demonstrated in simulations and experiments (Chapter 3).

1.6.4 LiDAR spherical grid-based localization and quantization theory to bound navigation uncertainty.

A new method was developed to enable uncertainty quantification in LiDAR grid-based localization. A spherical grid was used to process LiDAR point cloud data while limiting com-

putation and memory costs. Azimuth-elevation bins were determined using a quantization technique adapted from signal processing: the method reduces computation load, limits information loss, and provides a deterministic bound on LiDAR ranging quantization errors. This bound was used to model the impact of quantization errors on vehicle state estimation errors (Chapter 4).

1.6.5 Outdoor experimental validation of tightly integrated IMU/LiDAR.

An outdoor testbed was built and implemented to assess the performance of the localization algorithms in realistic automotive driving scenarios. In this case, the sensor platform was a car equipped with LiDAR and IMU. Carrier phase differential GNSS provided truth reference trajectory. Sensor data coming in different amounts at heterogeneous rates were time-synchronized and recorded for post-processing. Testing was conducted in a parking lot on the Virginia Tech Blacksburg campus (Chapter 4).

Chapter 2

Analytical and Empirical Navigation Safety Evaluation of Tightly-Integrated LiDAR/IMU Using Return-Light Intensity

This paper describes the design, analysis, and experimental evaluation of a new landmark-based localization method which integrates light detection and ranging (LiDAR) with inertial measurement units (IMU). We develop a tight IMU/LiDAR integration scheme, which exploits the complementary properties of the two sensors to facilitate safety risk evaluation. LiDAR localization updates limit the IMU error drift over time while IMU data improves LiDAR position and orientation (or pose) prediction, thereby reducing the risk of incorrectly associating perceived features with mapped landmarks. In addition, LiDAR return-light intensity measurements are incorporated to better distinguish landmarks, and further reduce the risk of incorrect associations. We analyze the localization algorithm's integrity performance using an automated testbed that generates analytical and empirical pose estimation error distributions.

2.1 Introduction for Landmark-Based IMU/LiDAR Localization Integrity

In this paper, we develop, analyze, and test new position and orientation (or pose) estimation and integrity monitoring methods using data from light detection and ranging (LiDAR) and inertial measurement units (IMUs). Testing is performed in a mapped laboratory environment.

This research is intended for safety evaluation in autonomous vehicles such as automated driving systems (ADS). ADS testing is necessary, but insufficient to provide navigation safety guarantees because accumulating autonomously-driven road miles does not provide a statistically significant number of traveled miles as compared to manned driving incidents [Kalra and Paddock (2016); Kalra and Groves (2017)].

In order to quantify safety risks in ADS navigation, we leverage prior analytical work in Global Navigation Satellite Systems (GNSS)-based aviation navigation, where safety is assessed in terms of integrity. Integrity is a measure of trust in sensor information [International Civil Aviation Organization (2006)]. Several methods have been established to predict aircraft GNSS integrity risk [Radio Technical Commission for Aeronautics (RTCA) Special Committee 159 (2006), Working Group C (2016)]. Unfortunately, those methods do not directly apply to ADS because ground vehicles operate under sky-obstructed areas where GNSS signals can be altered or blocked by buildings and trees.

ADS require sensors in addition to GNSS, such as IMUs, LiDAR, camera and radar. This paper focuses on IMU and LiDAR. Integrating LiDAR with IMU improves pose prediction by using IMU to coast between LiDAR pose updates and by using LiDAR updates to calibrate IMU biases [Opromolla et al. (2016)]. Prior work includes tightly-coupled implementations using the

IMU to determine the LiDARs tilt angle [Soloviev et al. (2007), Soloviev (2008)]. In Robotics, LiDAR-based localization is often achieved using odometry (e.g., from an IMU) and simultaneous localization and mapping (SLAM) [Leonard and Feder (2000), Montemerlo and Thrun (2003), Guivant et al. (2000), Nerurkar and Roumeliotis (2011), Guivant and Nebot (2001), Dryanovski et al. (2013), Bresson et al. (2015), Joerger et al. (2016), Hess et al. (2016), He et al. (2018), Zheng and Zhang (2019)]. However, SLAM is insufficient in safety-critical ADS navigation applications because localization errors drift over distance, and loop-closure is trajectory-constraining.

In this paper, we assume that an a-priori map is available. The first category of map-based LiDAR localization approaches includes matching and correlation methods. These methods aim at maximizing data point correspondences between the LiDAR point cloud (PC) and the map, whether the map itself is a PC [Pomerleau et al. (2013), Sappa et al. (2001), Guo et al. (2014)], or whether it is an occupancy grid map (OGM), i.e., a tessellated representation of the PC [Luo et al. (2020), Fan et al. (2018), Nuss et al. (2015)]. However, rigorous safety risk quantification using matching methods is an unsolved and cumbersome problem. Instead, this research uses a landmark-based localization method for which we developed an integrity risk equation in [Joerger et al. (2016), Joerger and Pervan (2017) Hassani et al. (2018), Joerger et al. (2017)]. Landmark-based localization aims at identifying landmarks in the LiDAR PC, and at matching them with mapped landmarks [Pirovano et al. (2020), Hunde and Ayalew (2018), Vosselman and Dijkman (2001)].

Landmark-based localization requires two pre-estimator procedures [Pirovano et al. (2020), Hunde and Ayalew (2018), Vosselman and Dijkman (2001)]. Fist, feature extraction (FE) aims at identifying the most consistently recognizable, viewpoint-invariant landmarks in the LiDAR PC. Then, data association (DA) matches the ordering of mapped landmarks to that of PC-extracted features over successive observations [BarShalom et al. (1990), Bailey (2002),

Cooper (2005), Joerger and Pervan (2009)]. Incorrect association (IA) is a well-known algorithmic fault that can cause a loss of navigation integrity.

This paper builds upon the multiple-hypothesis extended Kalman filter (EKF) innovation-based DA method in [Joerger et al. (2016)]. This method provides the means to evaluate the matching process' risk of IA while considering all possible combinations and permutations of sensed landmarks to mapped landmarks. The probability of IA is then used to bound the integrity risk of LiDAR-based pose estimation over successive iterations. References Joerger et al. (2016) and Joerger and Pervan (2017) showed that the probability of IA quickly grows in cluttered environments. One approach to mitigate this problem is to select a subset of the most distinguishable features in the LiDAR PC [Joerger et al. (2017)]. However, this approach reduces the number of redundant associations and lowers the ability to detect unwanted, unmapped landmarks.

In response, in this paper, we enhance DA and integrity monitoring performance by tightly integrating LiDAR with IMU and by incorporating LiDAR return-light intensity measurements. In addition, we design and implement an experimental testbed to evaluate the localization and DA performance of the IMU/LiDAR algorithm.

We first develop a tightly-integrated IMU/LiDAR process specifically to quantify integrity risk. IMU integration can reduce integrity risk not only by improving pose prediction but also by lowering the risk of IAs. Then, we derive a new method to exploit return-light intensity measurements, which LiDAR provides in addition to range and bearing angle observations. Light intensity measurements can improve the systems ability to distinguish landmarks if their surfaces have different reflectivity properties. For example, LiDAR intensity can help identify an aluminum pole from a pedestrian.

The second section of the paper describes the tightly-integrated EKF-based IMU/LiDAR algo-

rithm. Nonlinear continuous-time dynamic propagation and measurement equations are derived, linearized, and discretized. The third section of the paper is a derivation of the multiple-hypothesis DA and integrity risk bounding methods that focuses on the contributions of IMU and LiDAR intensity measurements. In the fourth section, we perform direct simulations and a covariance analysis to evaluate the risk reduction brought about by the IMU. In the fifth section, we experimentally quantify the reduction in integrity risk achieved when incorporating (a) IMU data, (b) LiDAR intensity measurements, and (c) both IMU data and LiDAR intensity.

2.2 High-Integrity IMU and LiDAR Measurement Models

2.2.1 IMU measurement equations

In this implementation, we use raw IMU accelerometer and gyroscope measurements. The IMU is fixed in the ADS body frame B, which can be approximately oriented along the vehicles principal axes of inertia. The IMU accelerometers measure inertial acceleration, i.e., second time-derivatives of position with respect to the inertial frame (labeled I), and we are interested in ADS pose expressed in a navigation frame N (for example, in the local East, North, Up directions). We also define an earth-centered, earth-fixed frame E because N may move in E. We use the Newton and Euler methods to describe the ADS translational and rotational motion. The following three equations respectively express the time-derivative of the ADS velocity with respect to N and expressed in N, the time-derivative of its position with respect to E and expressed in N, and the time-derivative of the rotation matrix from B to N as (following equation (3.26) in [Titterton et al. (2004)]):

$$ {}^{\mathrm{N}}\dot{\mathbf{v}}^{\mathrm{E}}_{ADS} = \frac{{}^{\mathrm{N}}d\,{}^{\mathrm{N}}\mathbf{v}^{\mathrm{E}}_{ADS}}{d\,t} = \mathbf{C}^{\mathrm{N}}_{\mathrm{B}}\,{}^{\mathrm{B}}\tilde{\mathbf{f}} - (2\,{}^{\mathrm{N}}\boldsymbol{\omega}^{\mathrm{IE}} + {}^{\mathrm{N}}\boldsymbol{\omega}^{\mathrm{EN}}) \times {}^{\mathrm{N}}\mathbf{v}^{\mathrm{E}}_{ADS} + {}^{\mathrm{N}}\mathbf{g} \tag{2.1} $$

$$ {}^{\mathrm{N}}\dot{\mathbf{x}}^{\mathrm{E}}_{ADS} = \frac{{}^{\mathrm{E}}d\,{}^{\mathrm{N}}\mathbf{x}_{ADS}}{d\,t} = {}^{\mathrm{N}}\mathbf{v}^{\mathrm{E}}_{ADS} \tag{2.2} $$

$$ \dot{\mathbf{C}}^{\mathrm{N}}_{\mathrm{B}} = \mathbf{C}^{\mathrm{N}}_{\mathrm{B}}[{}^{\mathrm{B}}\bar{\boldsymbol{\omega}}^{\mathrm{IB}}\times] - \left([{}^{\mathrm{N}}\boldsymbol{\omega}^{\mathrm{IE}}\times] + [{}^{\mathrm{N}}\boldsymbol{\omega}^{\mathrm{EN}}\times]\right)\mathbf{C}^{\mathrm{N}}_{\mathrm{B}} \tag{2.3} $$

where

${}^{\mathrm{N}}\mathbf{v}^{\mathrm{E}}_{ADS}$ is the 3×1 ground speed vector, i.e., the vehicle velocity vector with respect to E expressed in N,

${}^{\mathrm{A}}d/d\,t$ is a time-derivative with respect to frame 'A', where A may stand for B, E, I, or N,

$\mathbf{C}^{\mathrm{N}}_{\mathrm{B}}$ is the 3×3 rotation matrix from B to N [Titterton et al. (2004)],

${}^{\mathrm{N}}\mathbf{x}_{ADS}$ is the 3×1 vehicle position vector expressed in N,

${}^{\mathrm{B}}\bar{\mathbf{f}}$ is the 3×1 IMU measured and corrected specific force vector expressed in B and derived in Appendix B,

${}^{\mathrm{N}}\boldsymbol{\omega}^{\mathrm{IE}}$ is the angular velocity vector of E w.r.t I expressed in N,

${}^{\mathrm{N}}\boldsymbol{\omega}^{\mathrm{EN}}$ is the angular velocity vector of N w.r.t E expressed in N; it is small for the local car navigation application described in Section 2.5

${}^{\mathrm{B}}\bar{\boldsymbol{\omega}}^{\mathrm{IB}}$ is the measured and corrected angular velocity vector of B w.r.t I expressed in B; it is derived in Appendix B,

${}^{\mathrm{N}}\mathbf{g}$ is the local gravity vector at the IMU axis center expressed in N [Rogers (2007)],

$[\mathbf{a}\times]$ is the skew-symmetric matrix of vector $\mathbf{a}$.

2.2.2 LiDAR range and bearing angle measurement equations

A raw LiDAR PC is made of thousands of data points, each of which individually does not carry useful navigation information. Raw measurements must therefore be processed before they

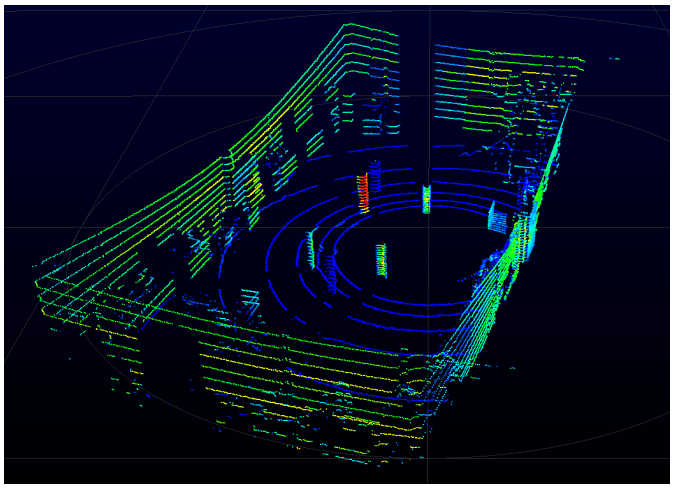

Figure 2.1: LiDAR point cloud showing return-light intensity (color-coded from blue to red, from low intensity to high intensity).

can be used for localization. FE (feature extraction) aims at consistently extracting identifiable static landmark features. Figure 2.1 shows an example of LiDAR PC collected in our laboratory testbed. Colors from red to blue respectively designate high to low levels of return-light intensity.

The experimental testbed in Figure 2.1 includes six static vertical cylinders with different surface properties, which are easy-to-distinguish landmarks that facilitate FE. We want successful FE because FE is not the primary focus of this paper. FE aims at finding the center of quasi-circular ellipses formed by the projection of the cylinders edges in the LiDAR zero-elevation angle plane. Figure 2.2 illustrates our two-step FE algorithm.

- *Segmentation*: Within an elevation cone, range differences over the azimuth-angle-sequence help distinguish cylinders from the background. Point clusters corresponding to cylinders can thus be segmented.

- *Model-fitting and feature estimation*: The segmented points are projected in the zero-elevation plane, and a two-dimensional (2D) circle-fitting algorithm is used to fit a circle to the projected points. This step assumes that cylinders are vertical and that the eleva-

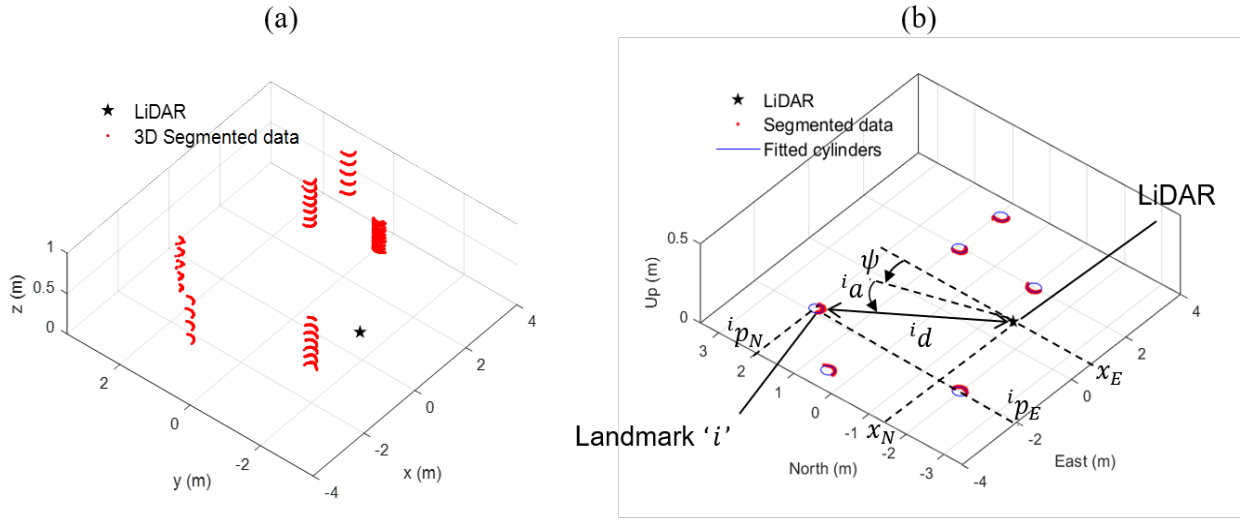

Figure 2.2: (a) 3D segmentation of LiDAR point cloud - (b) circle fitting and point-feature measurement extraction

tion plane is horizontal, which is valid in our lab environment.

The center of the fitted circle, parametrized by its range and bearing angle with respect to the LiDAR, is the extracted point-feature. Let ${}^i d$ and ${}^i a$ respectively be the range and bearing angle measurements in B for the point-feature of the landmark i, where $i = 1 \dots n_L$ and n_L is the number of extracted features. The horizontal position of the extracted point feature is time-invariant in the navigation frame N, which in this paper, is fixed in E. In addition, let ${}^i p_E$ and ${}^i p_N$ respectively be the East and North position coordinates of landmark i in N. The ADS position and orientation vectors in N, respectively $\mathbf{x}_{ADS}$ and $\mathbf{e}_{ADS}$ can be expressed as:

$$\mathbf{x}_{ADS} = \begin{bmatrix} x_E & x_N & x_U \end{bmatrix}^{\mathrm{T}} \tag{2.4}$$

$$\mathbf{e}_{ADS} = \begin{bmatrix} \phi & \theta & \psi \end{bmatrix}^{\mathrm{T}} \tag{2.5}$$

where x_E, x_N, x_U are the three-dimensional (3D) ADS position coordinates along the East, North, and Up axes, and ϕ, θ, ψ are the ADS Euler angles. Euler angles can be extracted from the rotation matrix in equation (2.3) as described in Appendix (B).

Using these notations, the non-linear LiDAR range and angular measurements are respectively given by:

$$^{i}d = \sqrt{(^{i}p_E - x_E)^2 + (^{i}p_N - x_N)^2} + \nu_d \tag{2.6}$$

$$^{i}a = \arctan\left(\frac{^{i}p_N - x_N}{^{i}p_E - x_E}\right) - \psi + \nu_a \tag{2.7}$$

In equations (2.6) and (2.7), ν_d and ν_a are random feature measurement errors. FE error distributions are not Gaussian but can be overbounded in the cumulative distribution function (CDF)-sense using zero-mean normal CDF models as described in Appendix (C) [DeCleene (2000), Rife et al. (2006), Blanch et al. (2019)]. Throughout the paper, the function 'arctan(b/a)', for $a \in \mathbb{R}$ and $b \in \mathbb{R}$, designates a function that equals arctan(b/a) when $a > 0$, arctan$(b/a) + \pi$ when $a < 0$, $\pi/2$ when $a = 0$ and $b > 0$, $-\pi/2$ when $a = 0$ and $b < 0$.

We can stack the ranging and angular measurements for all extracted landmarks in a $2n_L \times 1$ vector and write the LiDAR nonlinear measurement equation as:

$$\hat{\mathbf{z}} = \mathbf{h}(\mathbf{x}) + \boldsymbol{\nu} \tag{2.8}$$

$$\hat{\mathbf{z}} = \begin{bmatrix} d_1 \dots d_n & a_1 \dots a_n \end{bmatrix}^{\mathrm{T}} \tag{2.9}$$

$$\boldsymbol{\nu} = \begin{bmatrix} \nu_{d_1} \dots \nu_{d_n} & \nu_{a_1} \dots \nu_{a_n} \end{bmatrix}^{\mathrm{T}} \tag{2.10}$$

where

x is the $n_s \times 1$ state vector including ADS position, velocity, orientation and 3D IMU gyro and accelerometer biases; i.e., $n_s = 15$,

$\boldsymbol{\nu}$ is the $2n_L \times 1$ feature measurement error vector.

Vector $\boldsymbol{\nu}$ is modeled as a vector of normally distributed random variables with zero mean and covariance matrix $\mathbf{V}$. We use the notation: $\boldsymbol{\nu} \sim \mathrm{N}(\mathbf{0}, \mathbf{V})$. Non-zero elements of the diagonal matrix $\mathbf{V}$ are derived in Appendix (C). In equation (2.8), the vector function $\mathbf{h}(\mathbf{x})$ is made of stacked nonlinear equations (2.6) and (2.7) arranged as indicated in (2.9).

In addition, the LiDAR provides return intensity measurements for each PC point. We evaluate the mean intensity measurement for landmark i by averaging intensity values for all points in a point cluster associated with landmark i. The $n_L \times 1$ return-light intensity measurement vector is modeled as:

$$\hat{\mathbf{s}} = \mathbf{s} + \boldsymbol{\nu}_s \text{ and } \hat{\mathbf{s}} \sim \mathrm{N}(\mathbf{s}, \mathbf{V}_s) \tag{2.11}$$

where we use the overbounding distribution derivation in Appendix D to model $\mathbf{s}$ as normally distributed with mean $\mathbf{s}$ and diagonal covariance matrix $\mathbf{V}_s$. Vector $\boldsymbol{\nu}_s$ is an $n_L \times 1$ intensity measurement error vector modeled as $\boldsymbol{\nu}_s \sim \mathrm{N}(0, \mathbf{V}_s)$ as described in Appendix D.

2.2.3 Linearization and discretization of IMU and LiDAR equations

First, we linearize the IMU measurement equations. The continuous-time model is linearized using a first-order Taylor series expansion about reference state parameter values. We use the notation δ to indicate deviations of state parameters relative to the reference values. Using equations (2.1-2.3) and accelerometer and gyroscope measurement equations in Appendix B, we can write a continuous-time linearized state propagation model as:

$$\delta\dot{\mathbf{x}} = \mathbf{F}\delta\mathbf{x} + \delta\mathbf{w} \tag{2.12}$$

$$\delta\mathbf{x} = \begin{bmatrix} \delta\mathbf{x}_{ADS}^{\mathrm{T}} & \delta\mathbf{v}_{ADS}^{\mathrm{T}} & \delta\mathbf{e}_{ADS}^{\mathrm{T}} & \delta\mathbf{b}_{gy}^{\mathrm{T}} & \delta\mathbf{b}_{ac}^{\mathrm{T}} \end{bmatrix} \tag{2.13}$$

$$\mathbf{F} = \begin{bmatrix} \mathbf{0} & \mathbf{I} & \mathbf{0} & \mathbf{0} & \mathbf{0} \\ \mathbf{F}_{\mathrm{H2V}} & \mathbf{0} & [{}^{\mathrm{N}}\bar{\mathbf{f}}\times] & \mathbf{0} & \mathbf{C}_{\mathrm{B}}^{\mathrm{N}} \\ \mathbf{0} & \mathbf{F}_{\mathrm{V2T}} & -[{}^{\mathrm{N}}\boldsymbol{\omega}^{\mathrm{IN}}\times] & -\mathbf{C}_{\mathrm{B}}^{\mathrm{N}} & \mathbf{0} \\ \mathbf{0} & \mathbf{0} & \mathbf{0} & -\tau_{gy}^{-1}\mathbf{I} & \mathbf{0} \\ \mathbf{0} & \mathbf{0} & \mathbf{0} & \mathbf{0} & -\tau_{ac}^{-1}\mathbf{I} \end{bmatrix} \tag{2.14}$$

$$\delta\mathbf{w} = \begin{bmatrix} \mathbf{0} \\ -\mathbf{C}_{\mathrm{B}}^{\mathrm{N}}\left((\delta\mathbf{S}_{ac} + \delta\mathbf{M}_{ac})\,{}^{\mathrm{B}}\bar{\mathbf{f}} + \mathbf{C}_{\mathrm{B}}^{\mathrm{N}}\boldsymbol{\nu}_{ac}\right) \\ \mathbf{C}_{\mathrm{B}}^{\mathrm{N}}\left((\delta\mathbf{S}_{gy} + \delta\mathbf{M}_{gy})\,{}^{\mathrm{B}}\bar{\boldsymbol{\omega}}^{\mathrm{IB}} + \boldsymbol{\nu}_{gy}\right) \\ \mathbf{n}_{gy} \\ \mathbf{n}_{ac} \end{bmatrix} \tag{2.15}$$

where $\mathbf{b}_{gy}$ and $\mathbf{b}_{ac}$ are bias vectors of the IMU accelerometers and gyroscopes, $\mathbf{I}$ is the 3×3

identity matrix, ${}^{\mathrm{N}}\boldsymbol{\omega}^{\mathrm{IN}}$ is the angular velocity vector of I with respect to N expressed in N (which can be defined as: ${}^{\mathrm{N}}\boldsymbol{\omega}^{\mathrm{IN}} = {}^{\mathrm{N}}\boldsymbol{\omega}^{\mathrm{IE}} + {}^{\mathrm{N}}\boldsymbol{\omega}^{\mathrm{EN}}$, and ${}^{\mathrm{N}}\bar{\mathbf{f}}$ is the corrected specific force expressed in N. Matrices $\mathbf{F}_{\mathrm{H2V}}$ and $\mathbf{F}_{\mathrm{V2T}}$ are defined in Appendix A, and $\mathbf{S}$, $\mathbf{M}$, τ, $\mathbf{n}$ and $\boldsymbol{\nu}$ are defined in Appendix B for both the accelerometers and gyroscopes.

The discrete-time form of equation (2.12) can be written as:

$$\delta\mathbf{x}_k = \boldsymbol{\Phi}_{k-1}\delta\mathbf{x}_{k-1} + \delta\mathbf{w}_{k-1} \tag{2.16}$$

where k is a discrete-time step, $\boldsymbol{\Phi}_{k-1}$ is the $n_s \times n_s$ state transition matrix over the IMU sampling interval, i.e., between time steps $k-1$ and k. The discrete-time IMU measurement equations and the method for computing $\boldsymbol{\Phi}_{k-1}$ are found in Appendix B. Then, we linearize the LiDAR measurement equations. We can linearize equation (2.8) about our best prediction of the vehicle pose $\bar{\mathbf{x}}_k$. Considering both the LiDARs angular and ranging measurements, the total number of extracted feature measurements is $n = 2n_L$. Let $\hat{\mathbf{z}}_k$ be the $n \times 1$ feature measurement vector in equation (2.8). We use the overbounding distribution derivation in Appendix C to model $\hat{\mathbf{z}}_k$ as: $\hat{\mathbf{z}}_k \sim \mathrm{N}(\mathbf{z}_k, \mathbf{V}_k)$. Using a first-order Taylor series approximation, the linear measurement equation can be written in terms of the predicted state vector $\bar{\mathbf{x}}_k$ under the correct association (CA) hypothesis at time step k as:

$$\hat{\mathbf{z}}_k - \mathbf{h}_k(\bar{\mathbf{x}}_k) = \mathbf{H}_k\delta\mathbf{x}_k + \boldsymbol{\nu}_k \tag{2.17}$$

$$\begin{bmatrix} \delta\mathbf{d} \\ \delta\mathbf{a} \end{bmatrix}_k = \begin{bmatrix} \mathbf{F}_{d,x} & \mathbf{0} & \mathbf{0} & \mathbf{0} & \mathbf{0} \\ \mathbf{F}_{a,x} & \mathbf{0} & -\mathbf{F}_{a,e} & \mathbf{0} & \mathbf{0} \end{bmatrix}_k \begin{bmatrix} \delta\mathbf{x}_{ADS} \\ \delta\mathbf{v}_{ADS} \\ \delta\mathbf{e}_{ADS} \\ \delta\mathbf{b}_{gy} \\ \delta\mathbf{b}_{ac} \end{bmatrix}_k + \begin{bmatrix} \boldsymbol{\nu}_d \\ \boldsymbol{\nu}_a \end{bmatrix}_k$$

where the observation matrix $\mathbf{H}_k$ is a linearized measurement-to-state coefficient matrix. The linearized range and bearing angle measurement vectors and their measurement error vectors are respectively noted $\delta\mathbf{d}$, $\delta\mathbf{a}$ and $\boldsymbol{\nu}_d$, $\boldsymbol{\nu}_a$. The coefficient matrices $\mathbf{F}_{d,x}$, $\mathbf{F}_{a,x}$ and $\mathbf{F}_{a,e}$ are determined using the state prediction vector and assuming correct association as described in Appendix A. It is worth noting that subscript k is used in both equations (2.16) and (2.17). However, equation (2.17) is only relevant when LiDAR measurements are available, typically at regular 0.1s interval (for a 360° azimuth scan), whereas the IMU sampling interval is 10 to 20 times smaller.

2.3 Integrated LiDAR/IMU Estimation Process

In this section, we use an EKF to tightly integrate the LiDAR and IMU, and then, we derive an analytical upper bound on the ADS pose integrity risk that accounts for IA. The block diagram in Figure 2.3 outlines the three main steps of this process, which are color coded and described in detail in sections 3.1 to 3.3. The inputs to the block diagram are the IMU and LiDAR measurements and the map; the outputs are the pose estimation and integrity risk bound. Section 3.1 describes the IMU-based prediction process and includes the EKF initialization. Section 3.2 shows the EKF measurement update requiring data association; its output feeds into the state propagation equation. Section 3.3 describes the integrity risk bounding process, that

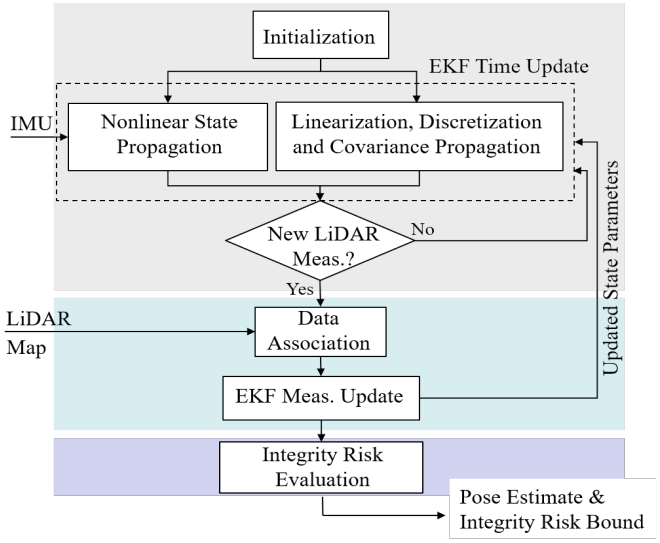

Figure 2.3: LiDAR/IMU integration block diagram (prediction, estimation, and integrity risk evaluation processes).

accounts for the impact of incorrect association.

2.3.1 EKF initialization and IMU-based pose prediction process

Figure 2.4 shows EKF initialization and prediction of the state vector $\mathbf{x}_k$ using IMU measurements input. It also shows the initialization of components of the integrity risk bound or probability of hazardous misleading information (HMI). The IMU specific force and angular velocity measurements are employed in two parallel processes. (a) *Nonlinear state propagation:* We use the discrete-time forms of nonlinear equations (2.1) to (2.3), the derivation of attitude using the rotation matrix from B to N, and the IMU measurements described in Appendix B to predict the state vector at each time step [Titterton et al. (2004)]. (b) *Linearization, discretization and covariance propagation:* We apply Van Loan's algorithm with the linearized equation (2.12) to compute the discrete-time transition matrix $\mathbf{\Phi}_{k-1}$ and the process noise covariance matrix $\mathbf{W}_{k-1}$. Let $\bar{\mathbf{x}}$ be the predicted state estimate and $\bar{\mathbf{P}}$ be the state prediction covariance matrix. The other parameters in Figure 2.4 are defined as:

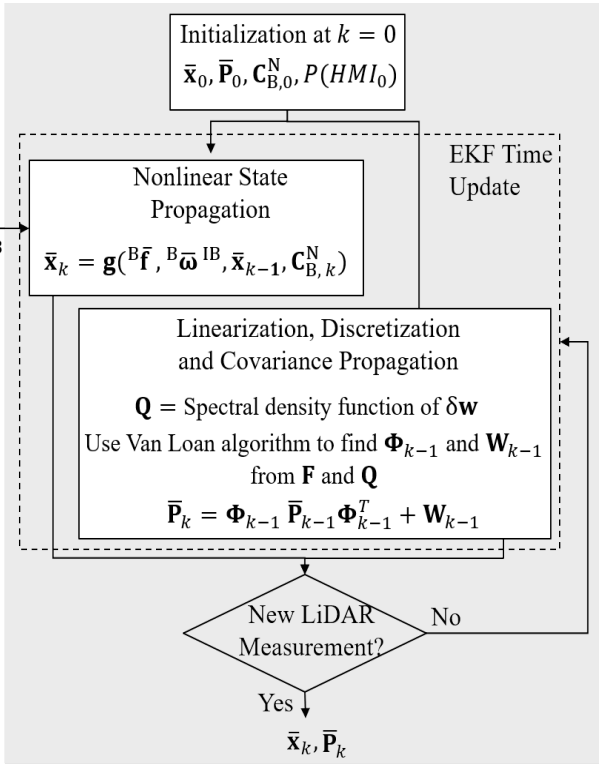

Figure 2.4: Initialization and EKF prediction process using IMU

$\bar{\mathbf{x}}_0$	is the $n_s \times 1$ initial predicted state estimate vector,
$\bar{\mathbf{P}}_0$	is the $n_s \times n_s$ initial EKF state prediction covariance matrix,
$P(HMI_0)$	is the initial value of the probability of hazardous misleading information (HMI),
$\mathbf{W}_k$	is the $n_s \times n_s$ process noise covariance at time step k,
$\bar{\mathbf{x}}_k$	is the $n_s \times 1$ predicted state estimate vector at time step k,
$\bar{\mathbf{P}}_k$	is the $n_s \times n_s$ prediction of EKF covariance matrix at time step k,
$\mathbf{g}$	is the discrete-time form of equations (2.1) to (2.3), defined in Appendix B.

We propagate the state vector $\mathbf{x}_k$ using nonlinear equations (2.1) to (2.3). After each iteration in the EKF dynamic propagation update, we check to see if there are LiDAR measurements at the current time step k or not. If there are, we implement a measurement update as described

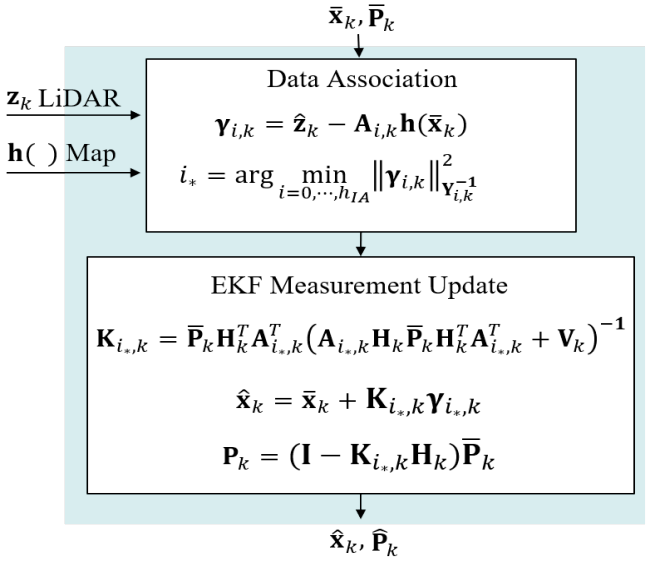

Figure 2.5: Data Association and KF estimation processes using LiDAR

in Section 3.2, otherwise, we keep iterating the dynamic propagation equations (2.1) to (2.3).

2.3.2 Data association criterion and EKF measurement update

We want to process the linearized LiDAR measurement equation (2.17) using the EKF measurement update to get a correction $\delta\mathbf{x}_k$, an estimate of the ADS state vector $\hat{\mathbf{x}}_k = \bar{\mathbf{x}}_k + \delta\mathbf{x}_k$, and covariance matrix $\hat{\mathbf{P}}_k$. This process requires that LiDAR measurements be associated with mapped landmarks correctly because their ordering is not necessarily the same.

To perform data association, we use an innovation-based approach [Joerger et al. (2016)]. The innovation vector under correct association $\boldsymbol{\gamma}_{0,k}$ is given by:

$$\boldsymbol{\gamma}_{0,k} \equiv \hat{\mathbf{z}}_k - \mathbf{A}_{0,k}\mathbf{h}_k(\bar{\mathbf{x}}_k) \tag{2.18}$$

where $\mathbf{A}_{0,k}$ is the $n \times n$ permutation matrix that corresponds to the correct association (CA).

In practice, we do not know which is the correct permutation matrix $\mathbf{A}_{0,k}$, but we can write an exhaustive set of permutation matrices.

The innovation vector can be interpreted as a measure of consistency between the extracted feature measurements $\hat{\mathbf{z}}_k$ and the measurement prediction vector $\mathbf{h}_{0,k}(\bar{\mathbf{x}}_k)$. The more accurate the state prediction is, the higher the likelihood of correct association becomes. State prediction improves, for example, by using IMU data instead of a vehicle kinematic model.

Accounting for incorrect data association

Extracted landmark feature measurements are arbitrarily ordered in vector $\hat{\mathbf{z}}_k$. In this paper, the number of measured landmarks in the LiDAR field of view (FOV) can be predicted using a reliable map and vehicle pose prediction. In the case of occlusion, if two landmarks are in a same azimuth bin, then only the landmark nearest to the LiDAR is visible. Other cases such as failed extractions or extracted-but-unmapped landmarks are addressed in prior work using combination matrices and detection [Hassani et al. (2019); Joerger et al. (2017)]. The focus of this paper is on the incorporation of IMU and intensity measurements. Let n_L be the number of extracted landmarks that are visible in the LiDAR FOV. There are $(n_L!)$ potential ways for assigning the observed landmarks to the mapped landmarks, which is the number of all possible landmark permutations.

IA occurs when the ordering of measured landmarks differs from that of mapped landmarks. There is only one correct ordering, so that the number of IAs is: $h_{IA} \equiv n_L! - 1$. For risk evaluation, we consider all possible orderings of measurements, $\bar{\mathbf{z}}_{i,k} = \mathbf{A}_{i,k}\mathbf{h}_k(\bar{\mathbf{x}}_k)$ and $\bar{\mathbf{s}}_{i,k}$ where $i = 0 \ldots h_{IA}$. In an example scenario where $n_L = 3$ landmarks (both extracted and mapped), the number of possible landmark permutations and IAs are 3! and $h_{IA} = 5$.

The innovation vector $\boldsymbol{\gamma}_{i,k}$ is zero mean only under correct association. Any other (incorrect)

association causes the mean of the innovation vector to be non-zero. Thus, the innovation vector is a good indicator of incorrect association. The innovation vector can be expressed as:

$$\boldsymbol{\gamma}_{i,k} = \hat{\mathbf{z}}_k - \mathbf{A}_{i,k}\mathbf{h}_k(\bar{\mathbf{x}}_k) \tag{2.19}$$

where $\mathbf{A}_{i,k}$ are $n \times n$ permutation matrices for $i = 0 \dots h_{IA}$.

Based on this criterion, we select the candidate association that satisfies the following equation:

$$i_* = \arg\min_{i=0\dots h_{IA}} \|\boldsymbol{\gamma}_{i,k}\|^2_{\mathbf{Y}^{-1}_{i,k}} \tag{2.20}$$

where

$$\|\boldsymbol{\gamma}_{i,k}\|^2_{\mathbf{Y}^{-1}_{i,k}} = \boldsymbol{\gamma}^{\mathrm{T}}_{i,k}\,\mathbf{Y}^{-1}_{i,k}\boldsymbol{\gamma}_{i,k}$$

$$\mathbf{Y}_{i,k} = \mathbf{A}_{i,k}\mathbf{H}_k\bar{\mathbf{P}}_k\mathbf{H}^{\mathrm{T}}_k\mathbf{A}^{\mathrm{T}}_{i,k} + \mathbf{V}_k$$

Figure 2.5 shows a detailed description of the second block in Figure 2.3. LiDAR measurements, map data, predicted states, and covariance matrix serve as inputs to the data association process in equation (2.20). Then, we proceed to the EKF measurement update, calculate the Kalman gain $\mathbf{K}_k$, and determine the $n_s \times 1$ state estimate vector $\hat{\mathbf{x}}_k$ and the $n_s \times n_s$ estimation error covariance matrix $\hat{\mathbf{P}}_k$. The state prediction vector $\bar{\mathbf{x}}_k$ in equations (2.18) and (2.19) is more accurate using a tightly integrated IMU as compared to an ADS kinematic model, which ultimately reduces the risk of incorrect association.

Integration of LiDAR return-light intensity to improve data association

The association process can be further improved using LiDAR return-light intensity. The difference between the LiDAR-extracted mean intensity measurements and that provided in the map, which is captured in the intensity-separation vector $\boldsymbol{\xi}_{i,k}$, can be expressed as:

$$\boldsymbol{\xi}_{i,k} = \hat{\mathbf{s}}_k - \mathbf{A}_{S_{i,k}} \bar{\mathbf{s}}_k \tag{2.21}$$

$$\boldsymbol{\xi}_{i,k} \sim \mathrm{N}(\mathbf{s}_k, \mathbf{A}_{S_{i,k}} \bar{\mathbf{S}}_k \mathbf{A}_{S_{i,k}}^{\mathrm{T}} + \mathbf{V}_{S,k})$$

where

$\mathbf{s}_k$ is the $n_L \times 1$ mean return-light intensity vector for all n_L visible landmarks,

$\hat{\mathbf{s}}_k$ is the $n_L \times 1$ LiDARs measured mean return-light intensity vector; we assume: $\hat{\mathbf{s}}_k \sim \mathrm{N}(\mathbf{s}_k, \mathbf{V}_{S,k})$,

$\bar{\mathbf{s}}_k$ is the mapped mean return-light intensity vector,

$\bar{\mathbf{S}}_k$ is the $n_L \times n_L$ covariance matrix capturing the uncertainty in mapped landmarks' mean intensity values,

$\mathbf{A}_{S_{i,k}}$ are $n_L \times n_L$ permutation matrices similar to the ones in equation (2.19) but for scalar permutations, for $i = 0 \ldots h_{IA}$.

Similar to the innovation vector in equation (2.18), the intensity separation vector in equation (2.21) is zero mean only if the correct association is found. Landmark intensity parameters are not included in the EKF prediction and estimation processes because they do not provide direct information on ADS states. However, we can still improve the association criterion by augmenting the innovation vector with $\boldsymbol{\xi}_{i,k}$. The resulting $3n_L \times 1$ separation vector is defined as: $\boldsymbol{\zeta}_{i,k} = \begin{bmatrix} \boldsymbol{\gamma}_{i,k}^{\mathrm{T}} & \boldsymbol{\xi}_{i,k}^{\mathrm{T}} \end{bmatrix}^{\mathrm{T}}$. The association selection criterion when incorporating the return-light

intensity is given by:

$$i_* = \arg\min_{i=0\ldots h_{IA}} \|\boldsymbol{\zeta}_{i,k}\|^2_{\mathbf{Z}^{-1}_{i,k}} \tag{2.22}$$

where

$$\mathbf{Z}_{i,k} = \begin{bmatrix} \mathbf{A}_{i,k}\mathbf{H}_k\bar{\mathbf{P}}_k\mathbf{H}_k^{\mathrm{T}}\mathbf{A}_{i,k}^{\mathrm{T}} + \mathbf{V}_k & \mathbf{0} \\ \mathbf{0} & \mathbf{A}_{S,i,k}\bar{\mathbf{S}}_k\mathbf{A}_{S,i,k}^{\mathrm{T}} + \mathbf{V}_{S,k} \end{bmatrix}$$

2.3.3 Integrity risk bound

The integrity risk $P(HMI_k)$, or probability of hazardously misleading information (HMI) at time step k, is the probability of the ADS being outside of a specified alert limit box when the vehicle position is estimated to be inside this box [Joerger and Pervan (2009), Reid et al. (2019)]. In ADS lane centering applications, lateral deviations are of primary concern, and the alert limit is defined as the distance between the edge of the car and the edge of the lane when the car is at the center of the lane [Joerger et al. (2016), Reid et al. (2019)]. An analytical bound on the integrity risk that considers all possible IAs is given in Joerger and Pervan (2019), and is expressed as:

$$P(HMI_k) \leq 1 - [1 - P(HMI_k|CA_K)] \prod_{j=1}^{k} P(CA_j|CA_{J-1}) + I_{ALLOC,k} \tag{2.23}$$

with

$$P(HMI_k|CA_K) = Q\left(\frac{l}{\sigma_k}\right) + 1 - Q\left(\frac{-l}{\sigma_k}\right) \tag{2.24}$$

$$P(CA_j|CA_{J-1}) \geq 1 - P\left(q_j^2 \geq \frac{L_j^2}{4}\right) \tag{2.25}$$

where

K designates a range of time indices: $K = \{1 \dots k\}$,

J designates a range of time indices: $J = \{1 \dots j\}$,

$Q()$ is the tail probability function of the standard normal distribution,

l is the specified alert limit that defines a hazardous situation,

σ_k is the standard deviation of the estimation error for the vehicle state of interest,

$I_{ALLOC,k}$ is a predefined integrity risk allocation for FE, chosen to be a fraction of the overall integrity risk requirement $I_{REQ,k}$,

q_j^2 is a chi-square distributed random variable with a number of degrees of freedom that is the sum of the number of measurements and of states at time step j,

L_j^2 represents the minimum value of the mean landmark feature separation, including intensity separation at time step j.

The probability of correct association (CA) in equation (2.25) is a function of L_j^2, which defines a probabilistic lower bound on the true value of ζ_k in equation (2.22). This lower-bound on landmark separation is set such that the risk of the true value of ζ_k being smaller than L_j^2 does not exceed $I_{ALLOC,k}$.

By integrating LiDAR with IMU, we can reduce positioning errors, thereby lowering the risk $P(HMI_k|CA_K)$. In addition, IMU and return-light intensity measurements are instrumental to increase the localization system's ability to distinguish landmarks. In equations (2.23-2.25), IMU and return light measurements enable greater separation L_j^2 values, which increases the probability of correct association $P(CA_j|CA_{J-1})$ and ultimately reduces $P(HMI_k)$. We will quantify this $P(HMI_k)$-reduction using simulation and experimental data in the next two sec-

Table 2.1: LiDAR and IMU simulation settings

Systems Parameters	**Values**
Standard deviation of LiDAR feature range data	0.12 m
Standard deviation of LiDAR feature angular data	4 °
LiDAR data sampling interval	0.5 s
Accelerometer velocity random walk	0.022 m/s/$\sqrt{\text{hr}}$
Gyroscope angle random walk	0.15 °/$\sqrt{\text{hr}}$
Accelerometer time constant	3600 s
Gyroscope time constant	3600 s
Standard deviation of accelerometer GMP bias	0.05 m/s^2
Standard deviation of Gyroscope GMP bias	0.2 °
Vehicle speed	1 m/s
Alert limit l	0.25 m

tions. Equations (2.23-2.25) are represented with the Integrity Risk Evaluation block in Figure 2.3, and its output is $P(HMI_k)$.

2.4 Integrity Risk Evaluation Using Simulated Data

In this section, we analyze the integrity performance of 'LiDAR-only as compared to using the IMU/LiDAR scheme described in Sections 2.3. In this two-dimensional (2D) horizontal simulation, an ADS roves between two landmarks located 10 meters apart. The initial pose of the ADS is known, and it is assumed that we have a map of landmark positions in the navigation frame N. Surface reflectivity is identical for all landmarks, and the intensity measurements are not used in this first evaluation. Simulation settings and LiDAR and IMU parameters are listed in Table 2.1.

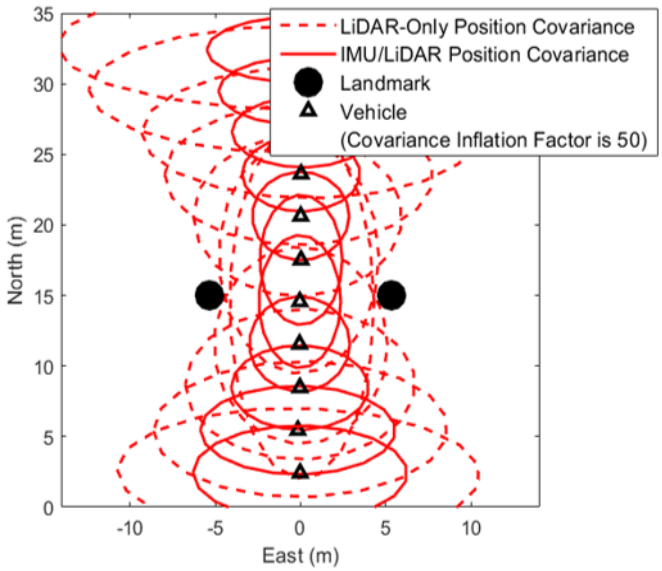

Figure 2.6: ADS positioning error covariance ellipses using LiDAR-Only and IMU/LiDAR for a two-Landmark scenario

2.4.1 Covariance analysis and integrity risk bound (analytical vs direct simulation)

In Figure 2.6, the positions of landmarks are represented with black circles, and the trajectory of the ADS is shown with black triangles. The 2D estimation error covariance ellipses which represent the spread of pose estimation error are shown in solid and dashed red lines and inflated by a factor 50 for better visualization. The size and shape of the covariance ellipses change as the sensor-to-landmark geometry changes due to ADS motion. The relative lengths of the semi-major and semi-minor axes are also related to the standard deviations of the LiDAR angular and ranging measurements as explained in Joerger (2009). This figure also shows that the integration of IMU with LiDAR improves ADS trajectory estimation.

In Figure 2.7, we evaluate the analytical integrity risk bound $P(HMI_k)$ as compared to the actual integrity risk calculated by direct simulation over 50,000 Monte Carlo (MC) trials for LiDAR-only and IMU/LiDAR. We focus on lateral deviations for integrity risk evaluation; the

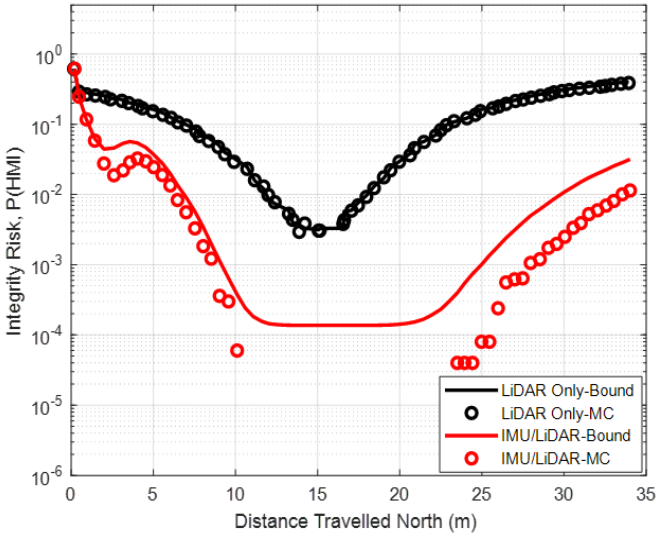

Figure 2.7: Lateral positioning integrity risk using LiDAR-Only and IMU/LiDAR for a two-landmark scenario: analytical bound versus Monte-Carlo (MC) simulations over 50,000 trials.

lateral alert limit is defined in Table 2.1. As captured in equation (2.23), $P(HMI_k)$ not only accounts for lateral covariance variations but also for the probability of correct association $P(CA_k)$.

In Figure 2.7, black and red circles represent the integrity risk curves obtained by direct simulation. In parallel, the black and red solid lines are the analytical bounds computed using equation (2.23). Both direct simulation and analytical bounds for IMU/LiDAR are orders of magnitudes lower than that for LiDAR-only between 10 and 20 meters of travel distance when the vehicle is close to the landmarks. Using IMU simultaneously improves pose estimation and DA, which results in a reduction of integrity risk. The direct simulation and analytical bounds for LiDAR-only overlap. Discrepancies occur for low risk values: these would disappear if we simulated more than 50,000 trials, but we have finite computational resources.

2.5 Experimental Integrity Risk Evaluation

In this section, we quantify navigation integrity for the multi-sensor IMU/LiDAR system described in Sections 2.2 and 2.3. We consider three configurations: LiDAR-only, LiDAR+ (incorporating mean intensity measurements to LiDAR range and bearing angle), and IMU/LiDAR+ (using all available sensor information). When using LiDAR only, state prediction $\bar{\mathbf{x}}_k$ is obtained using a coarse kinematic model to replace equation (2.12). This model propagates ADS states assuming a constant velocity vector between LiDAR measurement updates. This can be inaccurate for fast ADS dynamics. When using the IMU, we use equation (2.12) to improve state prediction $\bar{\mathbf{x}}_k$, but also to enhance DA. We performed an experimental test to quantify risk reductions brought about by incorporating LiDAR intensity and IMU measurements as compared to LiDAR-only. An automated sensor platform was moving on a figure-eight track next to a predefined set of landmarks, some of which were occluded over segments of the trajectory. Landmark occlusions can cause a heightened risk of incorrect association.

Additional testing results and performance comparisons using different sensor combinations can be found in [Hassani et al. (2019)]. In this paper, we focus on using LiDAR with intensity measurements and IMU data. Table 2.2 lists the parameters and settings of the test. In Figure 2.10, we use four landmarks, each identified by a number ranging from 1 to 4. The landmarks surface properties are not all the same: we use cylinders with a retro-reflective surface for Landmark 1, black surfaces for Landmarks 2 and 4, and a white surface for Landmark 3.

2.5.1 Experimental testbed

We designed and built an automated sensor safety evaluation testbed to quantify the impact of IA on the integrity risk $P(HMI_k)$. The testbed pictured in Figure 2.8 is composed of a rover housing a sensor platform on a figure-eight track. The rover can operate for many hours unat-

Table 2.2: LiDAR and IMU parameters and test settings

Systems Parameters	**Values**
Standard deviation of feature extraction ranging measurement	0.15 m
Standard deviation of feature extraction angular measurement	3°
Laser data sampling interval	0.1 s
Accelerometer velocity random walk	30 m/s/$\sqrt{\text{hr}}$
Gyroscope angle random walk	100 °/$\sqrt{\text{hr}}$
Accelerometer GMP bias correlation time constant	3600 s
Gyroscope GMP bias correlation time constant	3600 s
Standard deviation of accelerometer GMP bias	0.67 m/s^2
Standard deviation of gyroscope GMP bias	10°
IMU sampling time	0.01 s
Vehicle speed	0.6 m/s
Alert limit l	0.35 m

tended to collect large amounts of LiDAR and IMU data. This testbed provides a means to analyze a navigation system's performance over repeated trajectories, over a significant number of such trajectories, and in a controlled environment where we can focus, for example, on the integrity impacts of landmark occlusions, and of landmarks with varying surface properties. As compared to only using LiDAR range and angle measurements, this approach helps assess the relative performance improvement brought about by additional IMU and light-intensity data. Other experiments using sensors mounted on a car's roof rack will be carried out in future work.

In this experiment, cardboard cylinders serve as landmarks to facilitate FE from LiDAR PC. These cylinders are covered with white and black felt and retro-reflective straps (Landmark 1, first cylinder from the left) to provide different surface reflectivity. As the rover moves, the left-most landmark (Landmark 1) is periodically occluded behind another (Landmark 2), which tests the DA processs ability to dynamically distinguish landmarks.

The sensor platform mounted on the rover includes the LiDAR and IMU stacked vertically to minimize lever arms calibration errors. We use Velodyne's VLP-16 Puck LTE LiDAR and

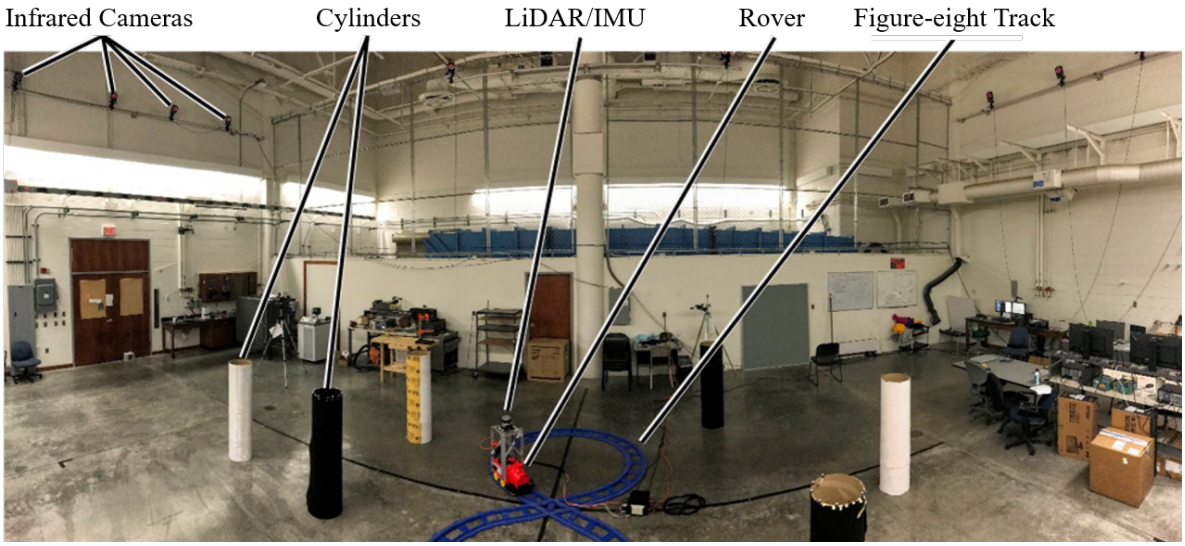

Figure 2.8: Automated testbed setup with sensor platform repeatedly moving on a figure-Eight track.

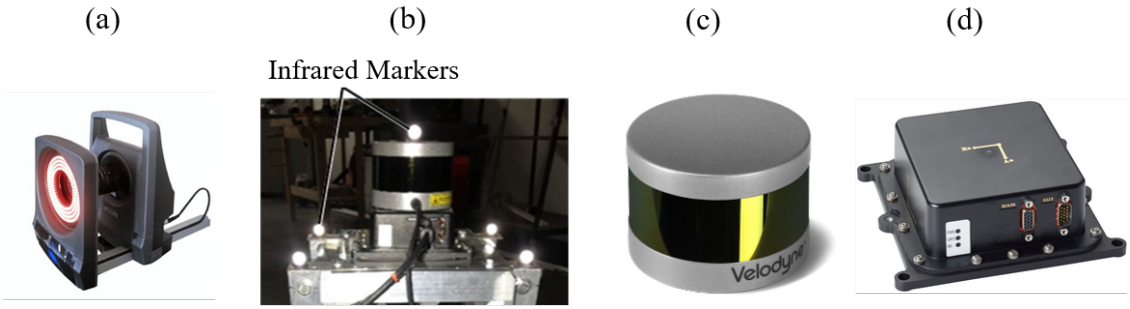

Figure 2.9: (a) IR Camera; (b) IR markers on sensor platform; (c) LiDAR -VLP-16 Puck; (d) IMU-IGM-A1

NovAtel's IMU-IGM-A1 coupled with NovAtel's ProPak6. The IMU is set to record at a 100 Hz sampling rate. Additionally, an infrared (IR) camera motion capture system (by VICON) provides reference truth values for the position and orientation of the moving platform and of the static landmarks in the navigation frame. Twelve cameras, four VICON MX-T20s and eight Vantage 5s, record small retro-reflective markers placed on the sensors and landmarks, providing sub-centimeter level positioning. All three sensors (IR cameras, LiDAR, and IMU) are time-tagged using the same computer clock.

2.5.2 Using LiDAR range, bearing, intensity and IMU measurements

The integrated solution using IMU, LiDAR range, angle, and intensity measurements is referred to as the IMU/LiDAR+ configuration. In Figure 2.10, four landmarks are used. The LiDAR range limit is such that all landmarks are continuously in view of the LiDAR except where Landmark 2 occludes Landmark 1. The estimated trajectory is represented with a blue line and the true trajectory with a black line. Estimated and true trajectories overlap. The black arrow shows the direction of motion at the starting point. Background colors help identify segments of the rover trajectory when presenting results over time: the rover follows straight line paths in the dark gray area, is in the top loop when in the white area, and in the bottom loop when in the light gray area. The purple area represents ADS locations where Landmark 1 is occluded by Landmark 2 in the upper-loop of the figure-eight track. This arrangement makes DA challenging because Landmarks 1 and 2 can be mistaken for one-another when Landmark 1 comes in and out of sight.

Figure 2.10 also shows red covariance ellipses representing two-dimensional positioning uncertainty for ADS locations taken at regular 0.8 s intervals. Covariance ellipses are inflated by a factor of five to facilitate visualization. Ellipses grow when Landmark 1 is hidden (purple area).

In addition, we derived a bound on the risk of the cross-track positioning error exceeding an example alert limit of 0.35 m Reid et al. (2019). This integrity risk bound is predictable. The event of the risk bound exceeding the risk requirement causes loss of availability. Thus, in this paper, we want the integrity risk bound to be as low as possible to achieve high availability performance. Both the actual integrity risk itself and our ability to analytically upper-bound this risk determine the value of the predicted risk bound. Thus, as compared to using LiDAR ranges, additional information from IMU and LiDAR intensity not only helps reduce the actual

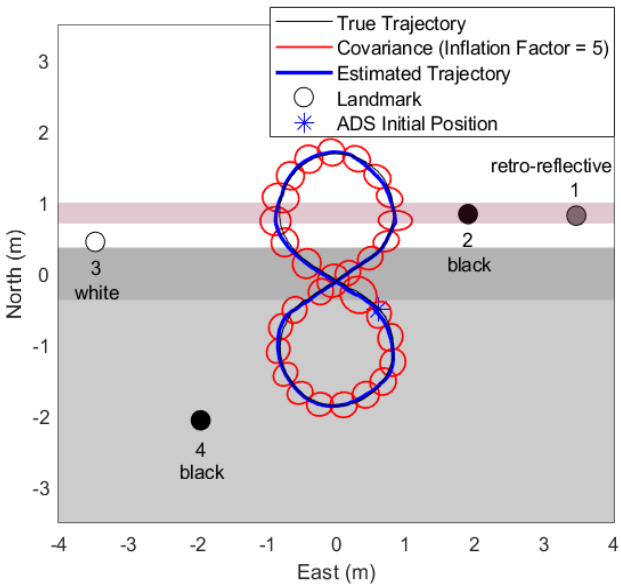

Figure 2.10: Covariance ellipses using IMU/LiDAR with intensity measurements

$P(HMI)$ but also helps tighten the predicted $P(HMI)$-bound. Figure 2.11 shows $P(HMI)$-curves for LiDAR-only, LiDAR+, and IMU/LiDAR+. We find the highest risk bound values in the purple regions because the occlusion of landmark 1 causes relatively poor landmark geometry. LiDAR-only performs relatively poorly, with a $P(HMI)$-bound approaching 1 as soon as the first difficult-to-identify landmark geometry is encountered. LiDAR+ is consistently better except when Landmark 1 is occluded because fewer measurements are available and the risk of IA increases. Finally, IMU/LiDAR+ expectedly outperforms all other configurations, and our tests show that the resulting $P(HMI)$-bound is at least four orders of magnitude lower than in the other cases, remaining below 10^{-10} throughout the test.

2.5.3 Repeated trajectories

Figure 2.12 shows the ADS cross track positioning error and covariance envelopes over 100 laps. The figure-eight track helps evaluate navigation system performance repeatability. The

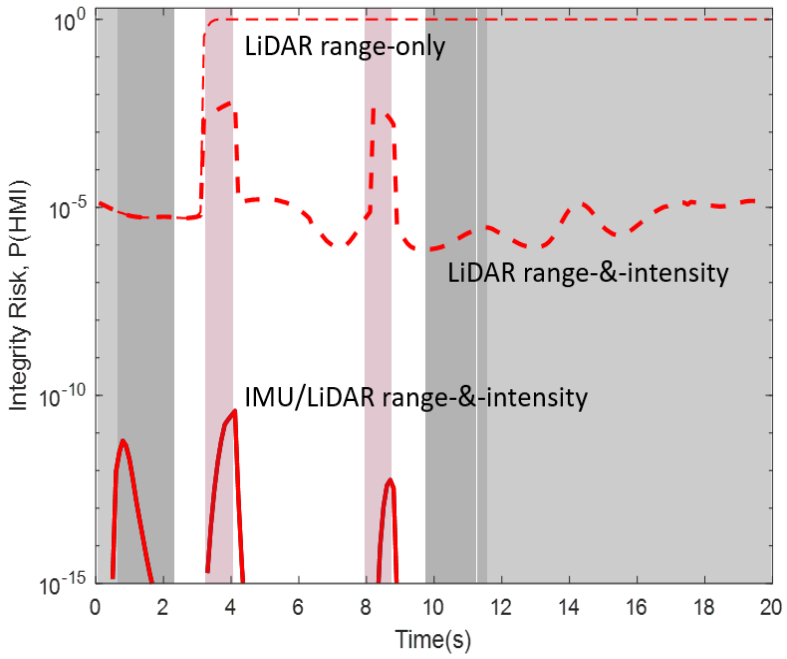

Figure 2.11: Integrity risk bounds using LiDAR-Only versus LiDAR+, IMU/LiDAR, IMU/LiDAR +

1σ one-dimensional envelope represents the boundary within which 68% of the error samples are expected to lie, assuming zero mean error.

The solid red line in Figure 2.12 is the analytical covariance envelope. The analytical covariance determines the contribution of $P(HMI_k|CA_K)$ to $P(HMI_k)$ in equation (2.23). The dashed red line is the sample covariance envelope, which is smaller than the analytical envelope over the entire 20-second long trajectory –by designed using overbounding theory, we want the analytical error bound to be larger than the sample envelope. Cross track positioning error curves are color-coded from light blue to dark blue as the rover travels from the first to the last lap. Small discrepancies can be observed between early and late laps (e.g., between Times 12 to 14 seconds), which are due to imperfections in the testbed including a warm-up period causing variations in vehicle speed and sensor performance [Ye and Borenstein (2002),Reina and Gonzales (1997)]. Overall we find that pose estimation error curves are conservatively

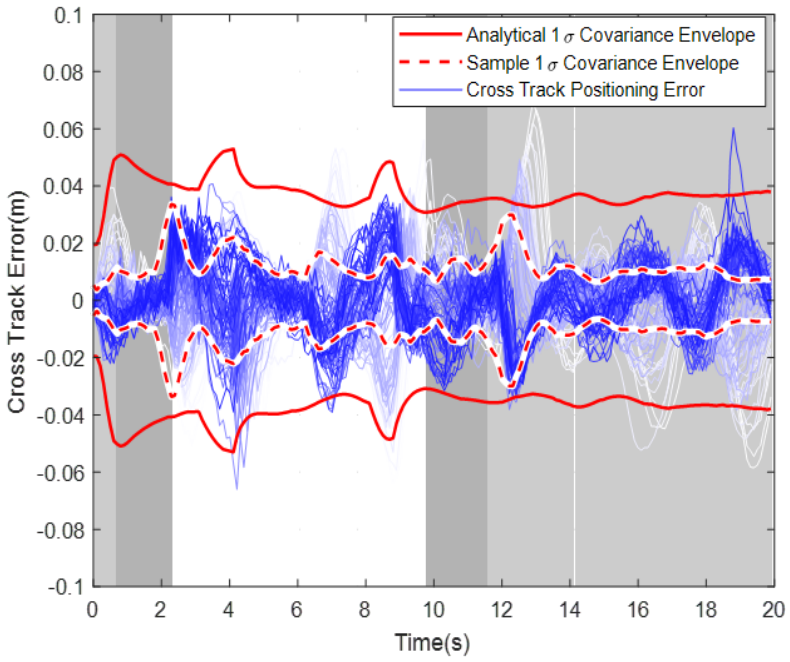

Figure 2.12: Cross track error of ADS for a hundred laps

captured by the analytical covariance envelope.

2.6 Conclusion for Landmark-Based IMU/LiDAR Localization Integrity

In this paper, we derived a new IMU/LiDAR integration method that enables integrity risk evaluation while accounting for all possible incorrect associations between observed and mapped landmarks. IMU improves state prediction and reduces incorrect association risks. Our method also incorporates LiDAR return-light intensity measurements to LiDAR range and bearing data to better distinguish landmarks, which also results in a quantifiable incorrect association risk reduction. We implemented a new analytical method to quantify the improvement in the probability of correct association. In addition, we evaluated the proposed integrity risk bound

using empirical data in a structured, well-understood environment. As compared to using LiDAR-only in this specific testing environment, the performance assessment demonstrated a reduction in integrity risk of several orders of magnitude using IMU and LiDAR intensity. Future work includes testing these methods in more realistic, unstructured environments.

Chapter 3

A New Data Association Method Using Kalman Filter Innovation Vector Projections

This paper describes the derivation, analysis, and implementation of a new data association method that provides a tight bound on the risk of incorrect association for LiDAR feature-based localization. Data association (DA) is the process of assigning currently-sensed features with ones that were previously observed. Most DA methods use a nearest-neighbor criterion based on the normalized innovation squared (NIS). They require complex algorithms to evaluate the risk of the incorrect association because sensor state prediction, prior observations, and current measurements are uncertain. In contrast, in this work, we derive a new DA criterion using projections of the extended Kalman filters innovation vector. The paper shows that innovation projections (IP) are signed quantities that not only capture the impact of an incorrect association in terms of its magnitude but also of its direction. The IP-based DA criterion also leverages the fact that incorrect associations are known and well-defined fault modes. Thus, as compared to NIS, IPs provide a much tighter bound on the predicted risk of incorrect association. We analyze and evaluate the new IP method using simulated and experimental data for autonomous inertial-aided LiDAR localization in a structured lab environment.

3.1 Introduction for Data Association Using Innovation Projections

GNSS uses code division multiple access to unambiguously identify and track multiple signals. But, landmark-based localization requires an additional data association (DA) step to recognize previously observed features, whether these features were just sensed or found in a map [BarShalom et al. (1990)]. Wrong associations (WA) can lead to large navigation errors [Joerger and Pervan (2009)] that can cause autonomous ground vehicles to collide or crash. In response, in this paper, we derive a new criterion to determine the correct association. Our approach not only mitigates occurrences of WA, but it also provides a tight bound on the risk of incorrection association. This work is primarily intended for the localization of automated driving systems (ADS) using LiDAR and inertial measurement units (IMUs). The focus is on LiDARs for their prevalence in ADS, their market availability, and our prior experience. A raw LiDAR scan is made of thousands of data points, each of which individually does not carry useful navigation information. Raw measurements must be pre-processed before they can be used for navigation [Thrun (2002); Leonard and Durrant-Whyte (1992); Williams et al. (2002); Lu and Milios (1997)].

A first class of algorithms establishes correlations between successive scans to estimate sensor changes in pose (i.e., position and orientation) [Lu and Milios (1997); Röfer (2002); Diosi and Kleeman (2005); Bengtsson and Baerveldt (2003)]. One of the most widely implemented approaches is the iterative closest point (ICP) [Lu and Milios (1997)]. Such procedures can become inaccurate or cumbersome for ADSs moving over time without loop closure unless a map is available. Occupancy grid maps (OGM) [Thrun (2002); Elfes (1989); Choi et al. (2013); Sato et al. (2010)] describe the environment using small cells, each of which either contains an object (i.e., is occupied) or does not. The environment can alternatively be interpreted

using probability hypothesis density (PHD), which captures the probability of objects being present at surrounding locations [Vo and Ma (2006)]. Combining PHDs with the random finite set (RFS) theory can help track objects in cluttered environments [Vo and Ma (2006); Mullane et al. (2011); Mahler and Martin (2003); Mullane et al. (2008)]. In the presence of repetitive patterns such as regularly spaced lamp poles or parked cars on a street, correlation-based algorithms using PHD and/or OGM that aim at minimizing pose estimation errors can converge to local minima [Mullane et al. (2008)], which can hinder localization risk evaluation.

A second class of algorithms, which is investigated in this paper, provides sensor localization by tracking recognizable, static features in the perceived environment. Two steps are needed: feature extraction (FE) and DA. FE aims at finding the few most consistently recognizable, viewpoint-invariant landmarks in the raw sensor data. DA aims at assigning landmark features to the corresponding feature parameters stored in a map. Yaakov Bar Shaloms seminal work on DA for multi-target tracking [1] has been successfully implemented, and built upon, in a wide variety of applications including landmark-based navigation [Joerger and Pervan (2009); Ruiz et al. (2001); Estrada et al. (2005); Bailey (2002)], pedestrian detection [Bicanic et al. (2019)], space situational awareness [Cai et al. (2018); Pirovano et al. (2020); Bellows (2015)], air and land surveillance and collision avoidance [Jan and Kao (2013); Jamoom et al. (2016); Lee and Joerger (2018)], for example, in traffic management [Hunde and Ayalew (2018)]. DA can be challenging in the presence of sensor uncertainty. This is why many advanced DA algorithms were developed in [Thrun (2002); Thrun et al. (1998); Maksarov and Durrant-Whyte (1995); Cooper (2005)].

Of primary concern in safety-critical autonomous vehicle navigation is the prediction of the risk of WA. Two of the most widely-used methods, the Probabilistic Data Association and the Joint Probabilistic Data Association (JPDA) [Bar-Shalom et al. (2009)], provide the means to evaluate the probability of correct association. But, these Bayesian approaches evaluate risk

given current sample data. They are not well suited for safety-critical applications due to the lack of safety risk prediction capability, and the problem of bounding the a-posteriori probability of association (a similar issue is encountered in [Chan et al. (2014)]). Another insightful approach is followed in [Areta et al. (2007)]. However, it makes approximations that do not necessarily have upper-bound risks, hence, do not guarantee safe operation. Reference [Areta et al. (2007)] also presents exact solutions that could only be evaluated using computationally expensive numerical methods, not adequate for real-time navigation.

To circumvent these issues, in our prior work, we derived an analytical upper bound on the risk of WA, which was used to predict navigation integrity [Joerger and Pervan (2019)]. We tested this method in landmark-based LiDAR localization applications [Joerger and Pervan (2019); Arana et al. (2019)]. Unfortunately, our ability to predict WA occurrences was limited, i.e., our WA risk bound was loose. Even in a structured lab environment with few, sparsely distributed landmarks, the predicted risk bound was high: we would predict that the situation was unsafe when the risk was actually low. Only when incorporating extra data from inertial measurement units (IMU) was available, we were able to achieve low-risk bounds [Hassani et al. (2019, 2018)].

Our prior work and most methods cited in the above three paragraphs are either directly based on Bar Shaloms DA criterion, which uses the normalized innovation squared (NIS), or on some variants also using a weighted norm of residuals. We describe the innovation vector upfront because it is at the heart of this paper. The innovation vector appears in the extended Kalman filter (EKF), the most widely implemented non-linear sequential estimator.

Let n_T be the number of targets in view. From each target originates a measurement set, for example, the targets position coordinates relative to the sensor. The n_T measurement sets are arranged in a measurement vector $\hat{\mathbf{z}}$. There are $(n_T!)$ possible ways that the n_T measurement sets could be arranged in $\hat{\mathbf{z}}$. The innovation vector, and its normalized expression $\boldsymbol{\gamma}_i$ defined

below, compares $\hat{\mathbf{z}}$ to a predicted version of $\hat{\mathbf{z}}$, noted $\mathbf{h}(\bar{\mathbf{x}})$. Vector $\mathbf{h}(\bar{\mathbf{x}})$ is a non-linear function of prior target observations and of the sensor state prediction $\bar{\mathbf{x}}$. Vector $\bar{\mathbf{x}}$ is typically made of the sensors location and orientation in a frame of interest (e.g., in a navigation frame East-North-Up). Simply put, vector $\mathbf{h}(\bar{\mathbf{x}})$ is a prediction of $\hat{\mathbf{z}}$ based on where the sensor is expected to be relative to mapped targets. Subscript i in $\boldsymbol{\gamma}_i$ designates a candidate association: because we do not know the actual ordering of measurements in vector $\hat{\mathbf{z}}$, we must assume that it may be permuted as compared to h($\bar{\mathbf{x}}$). Vector $\boldsymbol{\gamma}_i$ can therefore be expressed as:

$$\boldsymbol{\gamma}_i = \mathbf{W}_i(\mathbf{A}_i\hat{\mathbf{z}} - \mathbf{h}(\bar{\mathbf{x}})) \quad \text{for} \quad i = 0,\ldots,h \tag{3.1}$$

where $\mathbf{A}_i$ are permutation matrices, $\mathbf{W}_i \equiv \mathbf{Y}_i^{-1/2}$ with $\mathbf{Y}_i$ being the innovation vector covariance matrix, and $h \equiv n_T!-1$. We use the notation $i = 0$ for the correct association, which is unknown. Vector $\boldsymbol{\gamma}_i$ is zero mean if and only if $i = 0$ [Joerger and Pervan (2019)]. Thus, a sensible criterion to find the correct association is to take the minimum overall values of i of the norm squared of $\boldsymbol{\gamma}_i$, which is the NIS. The NIS-based method is effective but has limitations in safety-critical applications.

In this paper, we develop a new approach that departs from traditional NIS methods by using EKF innovation vector projections (IP). This IP approach improves DA performance predictions by providing a significantly tighter bound on the risk of WA as compared to NIS. The IP method relaxes the need for extra sensor data and for complex risk evaluation methods to reduce WA risk prediction.

Throughout the paper, we assume a known model of the measurement and sensor state parameter time-propagation. We limit the scope of the paper to cases where all sensed targets have previously been observed. Procedures for dealing with occluded targets, unwanted ob-

jects, and miss-extracted features can be found in [Joerger and Pervan (2017); Joerger et al. (2018); Duenasarana et al. (2018)] for the NIS approach. These cases will be addressed for IP-based DA in future work. The current IP approach matches targets as a set, which is sometimes referred to as a global nearest neighbor procedure [Bellows (2015); Arana et al. (2019); Duenasarana et al. (2018), as opposed to local nearest neighbor (LNN) that finds sensed targets corresponding to mapped targets one at a time [Bellows (2015); Duenasarana et al. (2018)]. The reason for this choice is that LNN requires setting thresholds, or gates, on local NIS [Bar-Shalom et al. (2009); Duenasarana et al. (2018)]. For safety analysis, we are concerned that worst-case associations occurring at the threshold would have to be accounted for, and that their impact on safety risk bounds (on missed extraction risk) would accumulate over time. The global nearest neighbor approach can be computationally more expensive, but can also be more efficient for safety evaluation than LNN.

Section 3.2 of the paper outlines our prior work and uses a one-dimensional two-target ranging example to illustrate the looseness of the NIS-based WA-risk bound. In Section 3.3, we derive the new DA criterion using IP. IP are signed quantities that not only capture the impact of a WA in terms of its magnitude, as does NIS, but also of its direction. We analyze the NIS versus IP approaches in Sections 3.4 and 3.5 using simulated and experimental data, respectively, for autonomous landmark-based inertial-aided LiDAR navigation in a structured environment.

3.2 Prior Work on Navigation Integrity Evaluation Using Normalized Innovations Squared

This section describes a DA method for autonomous landmark-based vehicle navigation in challenging environments, where GNSS is denied. For the NIS DA criterion, we provide a bound on the probability of correct association (CA), evaluate the looseness of this bound in an example two-landmark scenario, and incorporate it in an analytical integrity risk equation. Throughout the section, we point out the limitations of our previously derived NIS-based method. We label these limitations (**L1**) to (**L3**). They will motivate the development of the new IP method in section 3.3.

3.2.1 Data association using NIS

To find the most likely CA, which we label i_*, we select the association candidate that satisfies the nearest-neighbor criterion defined as (BarShalom et al., 1990):

$$i_* \equiv \arg\min_{i=0,\dots,h} \gamma_i^2 \tag{3.2}$$

with

$$\gamma_i^2 \equiv \boldsymbol{\upsilon}_i^T \boldsymbol{\upsilon}_i \tag{3.3}$$

In [Joerger and Pervan (2019)], we derived an analytical bound on the probability of CA, $P(CA)$. By definition of the DA criterion in equation 3.2, a WA occurs if the NIS γ_i^2 for any candidate

association $i \neq 0$ is smaller than γ_0^2. We derived the following $P(CA)$-bound in [Joerger and Pervan (2019)]:

$$P(CA) = 1 - P(WA) = 1 - P\left(\bigcup_{i=1}^{h} \gamma_i^2 \leq \gamma_0^2\right) \geq 1 - P\left(q^2 \geq \frac{y_{MIN}^2}{4}\right) \tag{3.4}$$

where

$$y_{MIN}^2 \equiv \min_{i=1,\ldots,h} y_i^2 \quad \text{and} \quad y_i^2 \equiv E\{\gamma_i^2\} \tag{3.5}$$

In equation 3.4, q^2 is a chi-squared random variable with $(n+m)$ degrees of freedom, where n is the number of measurements (length of $\hat{\mathbf{z}}$) and m is the number of states (length of $\hat{\mathbf{x}}$). In equation 3.5, $E\{\}$ designates the expected value operator. The last two sentences point out two limitations of this approach:

(L1) Even though $\boldsymbol{\gamma}_\mathbf{i}$ is n-dimensional, we had no choice but to consider a chi-squared random variable q^2 with $(n+m)$ degrees of freedom in order to properly account for the correlation of γ_i^2 with γ_0^2 in the second equality in equation 3.4 (details can be found in [(Joerger and Pervan, 2019)]).

(L2) y_i^2 is the mean value of γ_i^2. For $i > 0$, y_i^2 is a measure of separation between targets: the larger y_i^2 is, the better the ability to distinguish targets. y_i^2 is unknown. Our best guess for y_i^2 is the sample γ_i^2. We can use a model of the measurement and state prediction noise to derive a lower bound on y_i^2 that is guaranteed with a risk allocation drawn from the overall integrity risk requirement [Joerger and Pervan (2019)]. This extra step adds complications and contributes to the looseness of the $P(CA)$ bound. To limit the length of the paper, we do not include this step in the paper, but interested readers can find it

in [Joerger and Pervan (2019); Joerger et al. (2018)].

The $P(CA)$ bound in equation 3.4 is a compact expression. First, the factor '1/4' on the right-hand side was derived from the inverse of the sum squared of the maximum eigenvalues of two idempotent matrices [(Joerger and Pervan, 2019)]. Second, the bound accounts for all potential WA. To achieve this, we had to take the minimum value of y_i^2 over all possible WA.

(L3) The $P(CA)$ bound does not capture the individual contributions of each WA. Instead, in equation 3.5, it takes the minimum of y_i^2 for $i = 1, \ldots, h$. This limitation stems from the fact that equation 3.4 considers a union of events involving a chi-squared distributed DA statistic.

3.2.2 One-dimensional two-target DA example using NIS

To illustrate the looseness of the bound, we use the one-dimensional (1D) example displayed in figure 3.1. The problem is to estimate the scalar position x of the sensor (upward-pointing triangle) on a 1D navigation reference axis $\boldsymbol{R}$, given the positions p_A and p_B of two target landmarks (black circles), and using a set of noisy scalar measurements z_1 and z_2 between sensor and landmarks. The challenge of DA is, in the presence of sensor errors, to find the ordering of landmarks $\{p_A, p_B\}$ corresponding to the ordering of measurements $\{z_1, z_2\}$.

In this instance, the number of target landmarks is $n_T = 2$, and the number of possible permutations is $(n_T!) = 2$, i.e., we consider two innovation vectors $\boldsymbol{\gamma}_0$ and $\boldsymbol{\gamma}_1$. Let us define $\mathbf{y}_0$ and $\mathbf{y}_1$ as the mean vectors of $\boldsymbol{\gamma}_0$ and $\boldsymbol{\gamma}_1$. Because index 0 designates the CA, $\mathbf{y}_0 = 0$, but $\mathbf{y}_1 \neq 0$.

The DA criterion in equation3.2 is represented in figure 3.2 in normalized innovation space, which is two-dimensional ($n = 2$). Vectors $\mathbf{y}_0$ and $\mathbf{y}_1$ are represented with black dots, and $\mathbf{y}_0$ is at the origin. In addition, 5000 random samples of innovation vectors are displayed. The

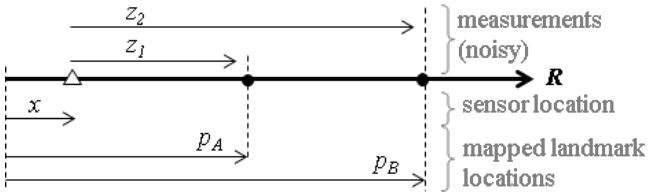

Figure 3.1: Illustrative one-dimensional example of a sensor (at location x in reference $\boldsymbol{R}$) providing observations to two landmarks (at locations p_A and p_B). Sensor to landmark measurements are noted z_1 and z_2.

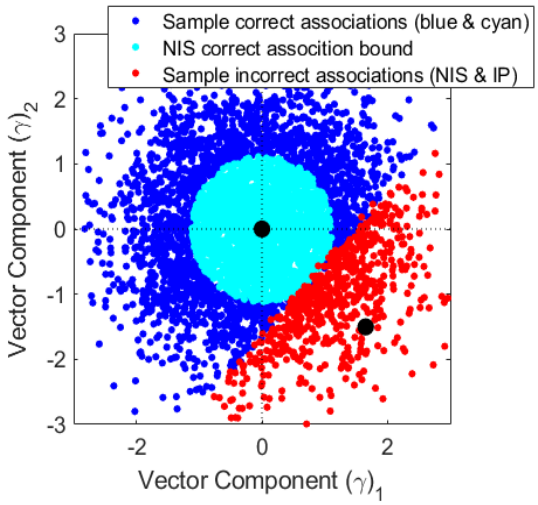

Figure 3.2: Two-dimensional normalized innovation-space representation of the association process. The ratio of blue-and-cyan samples over the total number of samples is the actual probability of correct association (CA). Only cyan samples are accounted for in the NIS lower-bound on the probability of CA.

innovation vectors are normalized, which explains the isotropic sample distribution. The criterion in equation 3.2 was directly used to distinguish correctly associated samples in blue-and-cyan, from incorrectly associated samples in red. The actual $P(CA)$ is the ratio of blue-and-cyan samples over the total number of samples. In addition, cyan dots represent correctly associated samples as counted using the bound in equation 3.4. We simulated measurement and state prediction noise with a large variance as compared to the target separation. In this particular example, the $P(CA)$ lower-bound bound only counted 26% of samples when in actuality, 87% were correctly associated. This direct simulation illustrates observation **(L3)**.

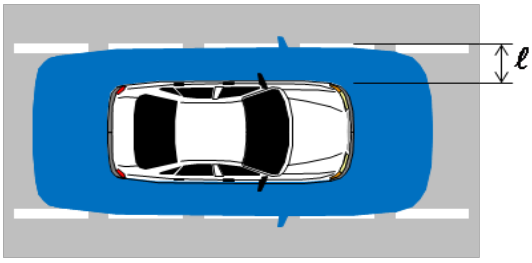

Figure 3.3: Integrity risk for automotive applications. The integrity risk is the probability of the car being outside the alert limit requirement box (blue shaded area) when it was estimated to be inside the box. When the lateral deviation is of primary concern, then the alert limit is the distance l between the edge of the car and the edge of the lane.

3.2.3 Example application: integrity risk bound using NIS

In prior work, we used the $P(CA)$-bound to quantify landmark-based navigation integrity in automotive applications [Joerger and Pervan (2019)]. The integrity risk, or probability of hazardously misleading information (HMI) at time k, is noted $P(HMI_k)$, and is defined in figure 3.3. The safety criterion is: $P(HMI_k) \leq I_{REQ,k}$ where $I_{REQ,k}$ is a predefined integrity risk requirement set by a certification authority (similar to requirements set for aviation applications in [Radio Technical Commission for Aeronautics (RTCA) Special Committee 159 (2007, 2006); International Civil Aviation Organization (2006))]. Values for $I_{REQ,k}$ that might be used in the future autonomous driving system (ADS) applications can be found in [U.S. DOT NHTSA (2017); U.S. DOT FHWA (2017); Reid et al. (2019)].

In [Joerger and Pervan (2019); Joerger et al. (2018)], we established an analytical bound on the integrity risk, which accounts for the risk of any incorrect association at any time. This bound is expressed as:

$$P(HMI_k) \leq 1 - [1 - P(HMI_k|CA_K)]\, P(CA_K) \tag{3.6}$$

with

$$P(HMI_k|CA_K) = 2Q\{l/\sigma_k\} \tag{3.7}$$

$$P(CA_K) \geq \prod_{l=1}^{k} P_{\chi^2}\left\{n_l + m_l, \frac{y_{MIN}^2}{4}\right\} \tag{3.8}$$

k is an index identifying a time step;

K designates a range of indices: $K = \{0, \ldots, k\}$ from filter initiation to time k;

CA_K is the correct association hypothesis for all landmarks, at all times $0, \ldots, k$;

$Q\{\}$ is the tail probability function of the standard normal distribution;

l is the specified alert limit that defines a hazardous situation [U.S. DOT NHTSA (2017); U.S. DOT FHWA (2017); Reid et al. (2019)] (e.g., see Figure 3.3);

σ_k is the standard deviation of the estimation error for the vehicle state of interest (or linear combination of states);

$P_{\chi^2}\{dof, T\}$ is the probability that a chi-squared-distributed random variable with dof degrees of freedom is lower than some value T;

n_l is the number of measurements at time step l;

m_l is the number of estimated state parameters at time l

In an EKF, because past-time WA can impact current-time state estimates, we must account for WA at all time steps from EKF initialization to current-time. This raises an additional concern.

Limitations **(L1)** to **(L3)** are the motivation for seeking a new approach, one that is not based on chi-square distributed random variables.

3.3 A New Approach Using Innovation Vector Projections

In order to address the limitations of the NIS-based method, we develop a new method that uses innovation projections (IP).

3.3.1 New data association criteria using IP

To avoid dealing with chi-squared variables, we project vectors $\boldsymbol{\gamma}_i$ to obtain a DA test statistic that is a linear combination of normally distributed random variables. Given that projections are signed quantities and that WA are well-structured sources of error, we will be able to leverage the direction of these errors to help identify them.

The first question is: what vector should $\boldsymbol{\gamma}_i$ be projected on? In innovation space, e.g., in Figure 3.2, the obvious direction is along $\mathbf{y}_1$. Vector $\mathbf{y}_1$ is unknown, but our best a-priori guess on $\mathbf{y}_1$, or $\mathbf{y}_j$ in general, is given by:

$$\bar{\boldsymbol{\gamma}}_j = \mathbf{W}_j(\mathbf{A}_j - \mathbf{I})\mathbf{h}(\bar{\mathbf{x}}) \quad \text{for} \quad j = 1,\ldots,h \tag{3.9}$$

where $\mathbf{I}$ is the $n \times n$ identity matrix and where we introduced the index j. We consider projections along all characteristic WA directions $\mathbf{y}_j$, or along our best guess, $\bar{\boldsymbol{\gamma}}_j$. The idea is to increase our chances of identifying WA by projecting $\boldsymbol{\gamma}_i$ along a direction that maximizes the projections magnitude, i.e., ideally along $\mathbf{y}_i$. In contrast, for the CA, projections of the zero-mean $\boldsymbol{\gamma}_0$ along any direction should be small. It is worth noticing that index j, for $j = 1,\ldots,h$, is known because we can generate the permutation matrices $\mathbf{A}_j$. But, which of index i is $i = 0$ remains unknown because the sample innovation vector is affected by measurement

and state prediction error. (We can generate a comprehensive set of permutations to $\boldsymbol{\gamma}_i$s, for $i = 0,\ldots,h$, but we do not know which of these is the CA).

The second question is: how to choose a criterion that combines all projections along $\bar{\boldsymbol{\gamma}}_j$, for $j = 1,\ldots,h$. After first considering the maximum projection, we settled on the sum of projections because it would help us evaluate a $P(CA)$-bound.

Therefore, the IP-based DA approach identifies the CA i_* using the following criterion:

$$i_* \equiv \arg\min_{i=0,\ldots,h} (\boldsymbol{\beta}^T \boldsymbol{\gamma}_i) \quad \text{where} \quad \boldsymbol{\beta} \equiv \sum_{j=1}^{h} \bar{\boldsymbol{\gamma}}_j \tag{3.10}$$

This expression involves more terms than the NIS criterion in 3.2: we compute vectors $\boldsymbol{\gamma}_i$, for $i = 0,\ldots,h$ as well as $\bar{\boldsymbol{\gamma}}_j$, for $j = 1,\ldots,h$. But the effectiveness of the resulting approach is worth the computational cost if $P(CA)$-evaluation is of interest. The next subsection provides an analytical lower bound on $P(CA)$ using IP.

3.3.2 Analytical bound on the probability of CA using IP

The starting point of the derivation is the following. A WA-event using the IP criterion in 3.10 occurs when the following inequality is always satisfied:

$$\boldsymbol{\beta}^T \boldsymbol{\gamma}_i \leq \boldsymbol{\beta}^T \boldsymbol{\gamma}_0 \quad \text{for any } i, \quad i = 1,\ldots,h \tag{3.11}$$

In order to evaluate the probability of occurrence of the WA-event, we respectively define the actual measurement and predicted measurement vectors as:

$$\hat{\mathbf{z}} = \mathbf{z} + \mathbf{v} \quad \text{and} \quad \mathbf{h}(\bar{\mathbf{x}}) = \mathbf{h}(\mathbf{x}) + \mathbf{H}\boldsymbol{\varepsilon} \tag{3.12}$$

where

$$\mathbf{z} \equiv \mathrm{E}\{\hat{\mathbf{z}}\}, \quad \mathbf{h}(\mathbf{x}) \equiv \mathrm{E}\{\mathbf{h}(\bar{\mathbf{x}})\}, \quad \mathbf{H} \equiv \left.\frac{\partial \mathbf{h}(\mathbf{x})}{\partial \mathbf{x}}\right|_{\mathbf{x}} \tag{3.13}$$

with E{} being the expectation operator. The measurement noise vector $\mathbf{v}$ is assumed normally distributed with zero mean and covariance $\mathbf{V}$. We use the notation: $\mathbf{v} \sim \mathrm{N}(\mathbf{0}, \mathbf{V})$. We assume that the state prediction error vector $\boldsymbol{\varepsilon} \equiv \bar{\mathbf{x}} - \mathrm{E}\{\bar{\mathbf{x}}\}$ satisfies: $\boldsymbol{\varepsilon} \sim \mathrm{N}(\mathbf{0}, \bar{\mathbf{P}})$. We can use these notations to express the innovation covariance matrix as: $\mathbf{Y}_i \equiv \mathbf{A}_i \mathbf{V} \mathbf{A}_i + \mathbf{H}\bar{\mathbf{P}}\mathbf{H}^T$.

The following inequalities are equivalent to (3.11):

$$\boldsymbol{\beta}^T[\boldsymbol{\gamma}_i - \boldsymbol{\gamma}_0] \leq 0$$

$$\boldsymbol{\beta}^T[\,\mathbf{W}_i(\mathbf{A}_i\hat{\mathbf{z}} - \mathbf{h}(\bar{\mathbf{x}})) - \mathbf{W}_0(\mathbf{A}_0\mathbf{v} - \mathbf{H}\boldsymbol{\varepsilon})] \leq 0$$

$$\boldsymbol{\beta}^T[\,\mathbf{W}_i(\mathbf{A}_i\mathbf{z} + \mathbf{A}_i\mathbf{v} - \mathbf{h}(\mathbf{x}) - \mathbf{H}\boldsymbol{\varepsilon}) - \mathbf{W}_0(\mathbf{A}_0\mathbf{v} - \mathbf{H}\boldsymbol{\varepsilon})] \leq 0 \tag{3.14}$$

By definition of a CA (subscript $i = 0$), $\mathrm{E}\{\boldsymbol{\gamma}_0\} = 0$, which is equivalent to:

$$\mathbf{A}_0\mathbf{z} = \mathbf{h}(\mathbf{x}), \quad \text{or} \quad \mathbf{z} = \mathbf{A}_0^T\mathbf{h}(\mathbf{x}) \tag{3.15}$$

Substituting (3.15) into (3.14) gives the following inequality:

$$\boldsymbol{\beta}^T\left[\,\mathbf{W}_i(\mathbf{A}_i\mathbf{A}_0^T\mathbf{h}(\mathbf{x}) - \mathbf{h}(\mathbf{x}) + \mathbf{A}_i\mathbf{v} - \mathbf{H}\boldsymbol{\varepsilon}) - \mathbf{W}_0(\mathbf{A}_0\mathbf{v} - \mathbf{H}\boldsymbol{\varepsilon})\right] \leq 0 \tag{3.16}$$

After re-arranging terms, (3.16) becomes:

$$\zeta_i \leq T_i \tag{3.17}$$

where

$$\zeta_i \equiv \boldsymbol{\beta}^T[(\mathbf{W}_i\mathbf{A}_i - \mathbf{W}_0\mathbf{A}_0)\mathbf{v} - (\mathbf{W}_i - \mathbf{W}_0)\mathbf{H}\boldsymbol{\varepsilon}]$$

$$T_i \equiv -\boldsymbol{\beta}^T\mathbf{W}_i(\mathbf{A}_i\mathbf{A}_0^T - \mathbf{I})\mathbf{h}(\mathbf{x})$$

The distribution of ζ_i is known:

$$\zeta_i \sim \mathrm{N}(0, \sigma_i^2) \tag{3.18}$$

where

$$\begin{aligned}\sigma_i^2 \equiv \boldsymbol{\beta}^T(\mathbf{W}_i\mathbf{A}_i - \mathbf{W}_0\mathbf{A}_0)\mathbf{V}(\mathbf{W}_i\mathbf{A}_i - \mathbf{W}_0\mathbf{A}_0)^T\boldsymbol{\beta} \\ + \boldsymbol{\beta}^T(\mathbf{W}_i - \mathbf{W}_0)\mathbf{H}\,\bar{\mathbf{P}}\,\mathbf{H}^T(\mathbf{W}_i - \mathbf{W}_0)^T\boldsymbol{\beta}\end{aligned}$$

Equation (3.17) can be used to evaluate the probability of the WA event occurring for a given i, for example for comparison with the expressions in (3.4) and (3.5).

In practice, $\mathbf{h}(\mathbf{x})$ is unknown; our best guess of $\mathbf{h}(\mathbf{x})$ is $\mathbf{h}(\bar{\mathbf{x}})$. A similar problem appeared for NIS, which was pointed out in (L2). Fortunately, the IP method offers a straightforward and efficient way to address the loose bound described in (L2). Substituting the equation $\mathbf{h}(\mathbf{x}) = \mathbf{h}(\bar{\mathbf{x}}) - \mathbf{H}\boldsymbol{\varepsilon}$ in T_i , substituting the result into (3.17), and rearranging terms, we obtain the following inequality:

$$\zeta_{N,i} \leq T_{N,i} \tag{3.19}$$

where

$$\zeta_{N,i} \equiv \boldsymbol{\beta}^T\left[(\mathbf{W}_i\mathbf{A}_i - \mathbf{W}_0\mathbf{A}_0)\mathbf{v} - (\mathbf{W}_i\mathbf{A}_i\mathbf{A}_0^T - \mathbf{W}_0)\mathbf{H}\boldsymbol{\varepsilon}\right]$$

$$T_{N,i} \equiv -\boldsymbol{\beta}^T \mathbf{W}_i (\mathbf{A}_i \mathbf{A}_0^T - \mathbf{I}) \mathbf{h}(\bar{\mathbf{x}})$$

The distribution of $\zeta_{N,i}$ is $\zeta_{N,i} \sim \mathrm{N}(0, \sigma_{N,i}^2)$, where:

$$\begin{aligned}\sigma_{N,i}^2 \equiv\ & \boldsymbol{\beta}^T (\mathbf{W}_i \mathbf{A}_i - \mathbf{W}_0 \mathbf{A}_0) \mathbf{V} (\mathbf{W}_i \mathbf{A}_i - \mathbf{W}_0 \mathbf{A}_0)^T \boldsymbol{\beta} \\ & + \boldsymbol{\beta}^T (\mathbf{W}_i \mathbf{A}_i \mathbf{A}_0^T - \mathbf{W}_0) \mathbf{H} \bar{\mathbf{P}} \mathbf{H}^T (\mathbf{W}_i \mathbf{A}_i \mathbf{A}_0^T - \mathbf{W}_0)^T \boldsymbol{\beta}\end{aligned}$$

For clarity of explanation and to limit the length of the paper, we use equations (3.1) to (3.5) for NIS and the inequality in (3.17) rather than (3.19) for the IP approach. We are able to do so in the Testing and Experimental Evaluation because reference truth is available. Even though this extra benefit of the IP methods ability to address (L2) is not leveraged, it will still outperform NIS. By definition of a WA in (3.11), we can write the following expression:

$$\begin{aligned}P(CA) = 1 - P(WA) &= 1 - P\left(\bigcup_{i=1}^{h} \boldsymbol{\beta}^T \boldsymbol{\gamma}_i \le \boldsymbol{\beta}^T \boldsymbol{\gamma}_0 \right) \\ &\ge 1 - \sum_{i=1}^{h} P(\zeta_i \le T_i) \ge 1 - \sum_{i=1}^{h} \Phi(T_i / \sigma_i)\end{aligned} \tag{3.20}$$

In (3.20), the probability of a union of events is upper-bounded by the sum of probabilities of each individual event. This will cause a loose bound in a cluttered environment when measurements and state predictions are highly uncertain, i.e., when the actual WA risk is high. The bound will be tight when it matters, i.e., when the actual risk is low enough to approach or meet safety-critical requirements.

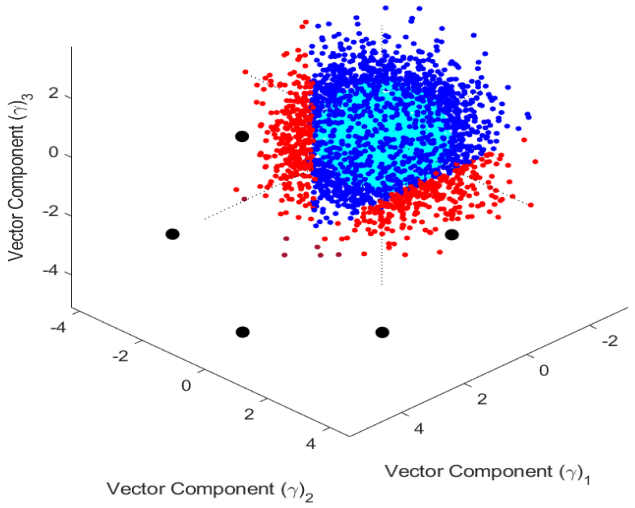

Figure 3.4: Three-dimensional normalized innovation-space representation of the association process. The ratio of blue-and-cyan samples over the total number of samples is the actual probability of correct association (CA). Only cyan samples are accounted for in the NIS lower-bound on the probability of CA, whereas both blue and cyan samples are accounted for using IP. A few maroon data points (bottom left of the sample ball) are double-counted using the IP bound.

3.3.3 One-dimensional two-target DA example using IP

We evaluated the IP method by direct simulation for the 1D example in Figure 3.1. For each association hypothesis, the IP criterion in equation (3.10) separates the innovation hyperspace, which is a plane in Figure 3.2, in a half-space for CA and the other half space for WA. In contrast, the NIS criterion in equation (3.2) identifies CA within a hypersphere (a circle in Figure 3.2) of radius the half-magnitude of the smallest mean innovation vector. The IP criterion produced the same WA red samples in Figure 3.2 as NIS, which means that the *actual* WA risk is the same using both methods. However, the IP CA bound in equation (3.20) gave 86.9%, which accurately estimated the actual sample CA probability of 87% (ratio of blue-&-cyan samples over all samples), much more so than the 26% NIS bound obtained using equation (3.4).

The 1D example in Figure 3.1 was extended to include a third landmark. The separation between pairs of adjacent landmarks was taken to be the same. Values of the actual distance between landmarks, measurement error, and state prediction variance, are inconsequential in this preliminary discussion. Thus, in Figure 3.4, the innovation space is three-dimensional ($n_T = 3$) and the number of innovation permutations is $n_T! = 6$. The 6 mean innovation vectors are represented with black dots. Red samples represent incorrectly associated cases, which again match for the NIS and IP approaches. Cyan dots representing the NIS CA bound are not easy to distinguish, but they are within a sphere centered at the origin. In contrast, the IP CA bound is more accurate because it can be represented as including both cyan and blue samples. Six maroon data points at the bottom left of the sample-ball are double or triple-counted using the IP bound because they lay in overlapping half-spaces as defined in equation (3.17) for $i = 1, \ldots, h$. In this example, the actual CA probability was 88.2%, well approximated by the IP bound with 88%, whereas the NIS bound gave 35.5%.

3.4 Risk Bound Analysis Using Simulated Data

This section compares NIS versus IP DA criteria in an example application of landmark-based LiDAR/IMU navigation, for a vehicle roving between landmarks. We assume that the initial rover position is known and that a map is available. The EKF-based algorithm is detailed in [Hassani et al. (2018)]. We use this simulation to illustrate how the IP method addresses the NIS limitations. A two-landmark scenario illustrates the difference in NIS versus IP DA risk bounds and assesses the looseness of the NIS bound as pointed out in (**L1**) to (**L3**).

In Figure 3.5, a rover whose location over time is shown with black triangles drives by two point-feature landmarks represented with black circles. The vehicle is equipped with a LiDAR/IMU system with specifications given in Table 3.1. We picked error model parameter

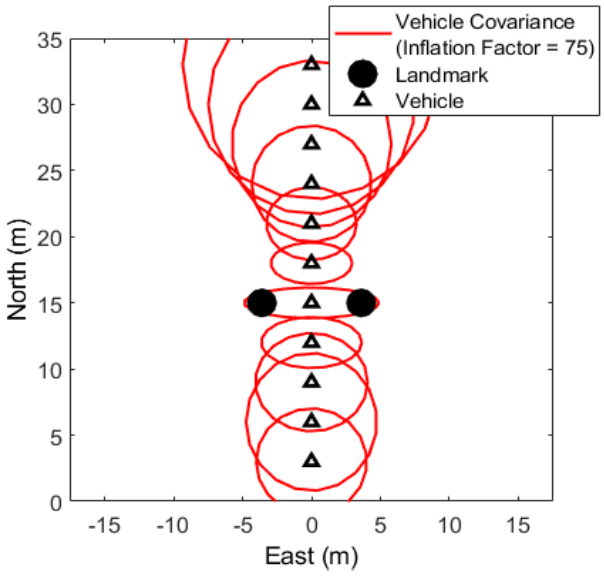

Figure 3.5: Vehicle and landmark positioning covariance analysis Using LiDAR/IMU in EKF-based simultaneous localization and mapping (SLAM) for the two-Landmark scenario.

values, in particular a large LiDAR range error standard deviation, in order to facilitate risk evaluation by direct simulations using a tractable number of random samples. The red ellipses in Figure 3.5 are inflated by a factor of 75 to facilitate visualization. They represent the rovers positioning errors. The ellipses shape and dimensions vary as the LiDAR-to-landmark geometry changes due to rover motion. The impact of geometry changes on lateral positioning deviations, which are of primary concern in this paper, are analyzed in detail in [Joerger and Pervan (2009)].

The covariance ellipses in Figure 3.5 assume that CA is always achieved. In contrast, the integrity risk accounts for *P(CA)*. Figure 3.6 shows $P(HMI_k)$ curves evaluated by direct simulation of random state prediction and measurement errors over 10,000 Monte Carlo (MC) trials. The actual risk curve for the IP method (red cross markers) matches that of the NIS approach (black circles). In parallel, -bounds are derived using equations (3.6) and (3.4) for NIS, and using equations (3.6) and (3.20) for IP, and are respectively shown in black and red. The two curves overlap for rover travel distances smaller than 15 meters and larger than 30 meters be-

Table 3.1: LIDAR and IMU simulation parameters

Systems Parameters	**Values**
Standard deviation of LiDAR feature range data	0.3 m
Standard deviation of LiDAR feature angular data	0.5 °
LiDAR data sampling interval	0.5 s
Accelerometer velocity random walk	$0.022\ \mathrm{m/s^2}/\sqrt{\mathrm{Hz}}$
Gyroscope angle random walk	$0.15\ ^\circ/\sqrt{\mathrm{Hz}}$
Accelerometer time constant	3600 s
Gyroscope time constant	3600 s
Standard deviation of accelerometer GMRP bias	$0.1\ \mathrm{m/s^2}$
Standard deviation of Gyroscope GMRP bias	0.2 °
Vehicle speed	1 m/s
Alert limit l	0.25 m

cause over these two ranges, the $P(HMI_k|CA_K)$ term dominates in equation (3.6). For IP, the $P(HMI_k)$-bound approaches the actual risk over most of the trajectory. For travel distances 15-to-30 meters, the conservative bound dominates the NIS bound, but this is not the case for the IP approach that achieves orders of magnitude lower $P(HMI_k)$-bound values.

3.5 Testing and Performance Analysis

In this section, we test the new DA IP-based method using actual data in a landmark-based navigation application using LiDAR/IMU. The LiDAR/IMU estimation method was derived in [Hassani et al. (2019)].

Figure 3.7 shows the experimental testbed that we designed to quantify [Hassani et al. (2019)]. The testbed comprises a sensor-equipped rover moving on a figure-eight track, and an infrared (IR) camera motion capture system providing truth reference trajectory. The rover can operate for hours unattended to collect LiDAR and IMU data over repeated trajectory passes. We use Velodynes VLP-16 Puck LTE LiDAR and NovAtels IMU-IGM-A1 coupled with NovA-

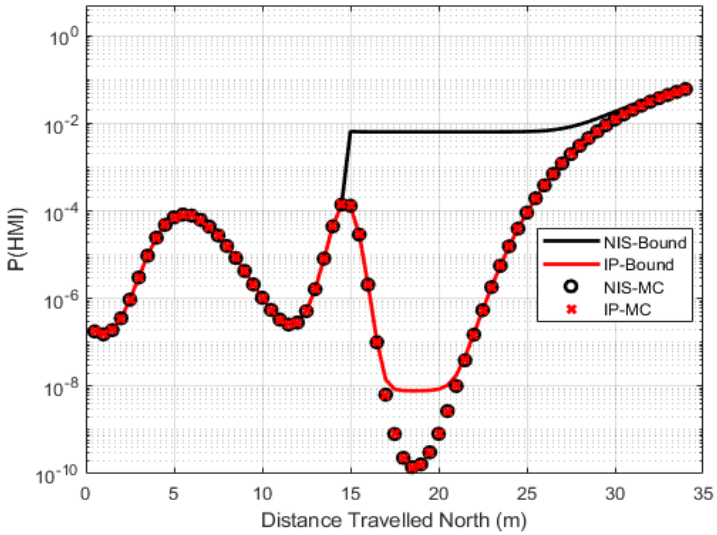

Figure 3.6: Integrity risk bounds using NIS versus IP-based data association for the two-landmark scenario.

tels ProPak6. The IMU is set to record at a 100 Hz sampling rate. The motion capture system includes twelve cameras, four VICON MX-T20s, and eight Vantage 5s, which record the locations of small retro-reflective markers placed on the sensors and landmarks, thus providing sub-centimeter level positioning and mapping at up to 200 Hz update rates. Data from all three sensors, IR cameras, LiDAR, and IMU, are time-tagged on a common computer clock and post-processed.

The landmarks used for navigation are four cylindrical landmarks. This simplistic test setup facilitates feature extraction and was chosen to avoid obscuring the analysis with extraction errors. In this case, the features are the coordinates in the navigation frame of the intersection between a cylinder axis and an arbitrary horizontal plane (e.g., the ground plane). In this implementation, we use a preset map of the cylinders. Our current feature extraction routine was evaluated in [Hassani et al. (2019)]. The test setup parameter values are listed in Table 3.2.

We evaluate the localization performance of an IMU-aided LiDAR localization system. The IMU helps maintain an accurate measurement prediction $\mathbf{h}(\bar{\mathbf{x}})$.

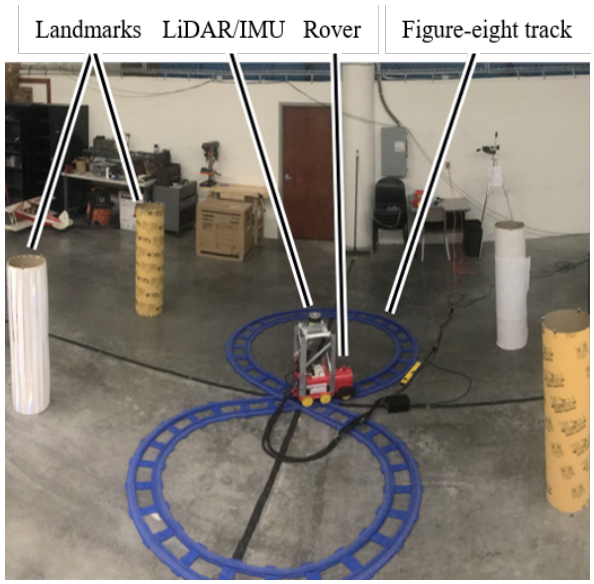

Figure 3.7: Testbed setup (VICON cameras at the ceiling are not shown).

In Figure 3.8, the true and estimated trajectories are respectively represented with a thin black line and a thick blue line. They are overlapping. Rover positioning uncertainty is represented with red covariance ellipses. An inflation factor of 5 is used to facilitate visualization. Background shades of gray are used consistently across figures to identify segments of the rover trajectory: the dark gray area designates straight segments while light-gray and white areas respectively designate the top and bottom loops of the trajectory.

Figure 3.9 displays $P(HMI_k)$-bounds using the NIS-based DA criterion in black, and using IP in red. The $P(HMI_k)$ bound is our safest estimate of the risk that the cross-track positioning error exceeds a 0.25 m alert limit. The NIS curve suggests that the term capturing the risk of WA quickly becomes prevalent in the NIS $P(HMI_k)$-bound, which thus increases monotonically and reaches $10^{-}1$ within the first 3 seconds. The bound stays at that level because *P(CA)* in equation (3.8) is computed as a product of contributions over time: this risk contribution can only increase. In contrast, the IP-based bound remains lower than $10^{-}5$. The red curves variations reflect changes in positioning variance due to changes in the vehicle-to-landmark

Table 3.2: Test settings and parameters

Systems Parameters	**Values**
Standard deviation of feature extraction ranging measurement	0.15 m
Standard deviation of feature extraction angular measurement	3°
Laser data sampling interval	0.1 s
Accelerometer velocity random walk	4.739 $m/s^2/\sqrt{Hz}$
Gyroscope angle random walk	17.244 $rad/\sqrt{s}$
Accelerometer bias GMRP correlation time constant	3600 s
Gyroscope bias GMRP correlation time Constant	3600 s
Standard deviation of accelerometer GMRP bias	0.67 m/s^2
Standard deviation of gyroscope GMRP bias	10°
IMU sampling time	0.01 s
Vehicle speed	0.6 m/s
Alert limit l	0.25 m

geometry as the rover moves.

3.6 Conclusion for Data Association Using Innovation Projections

In this paper, we develop a new approach to data association for multi-target tracking in autonomous vehicle landmark-based navigation using LiDAR/IMU. The new method determines correspondences between currently and previously observed targets using innovation projections (IP), as opposed to the more conventional criterion based on normalized innovation squared (NIS). The IP-based method provides a significant improvement in our ability to evaluate the risk of wrong associations (WA). We evaluated the new method using simulation and testing. The IP-based method demonstrated integrity risk levels orders of magnitude lower than the NIS method. Whereas the NIS risk bound inevitably increased as potential exposures to WA accumulated, the IP method stayed low.

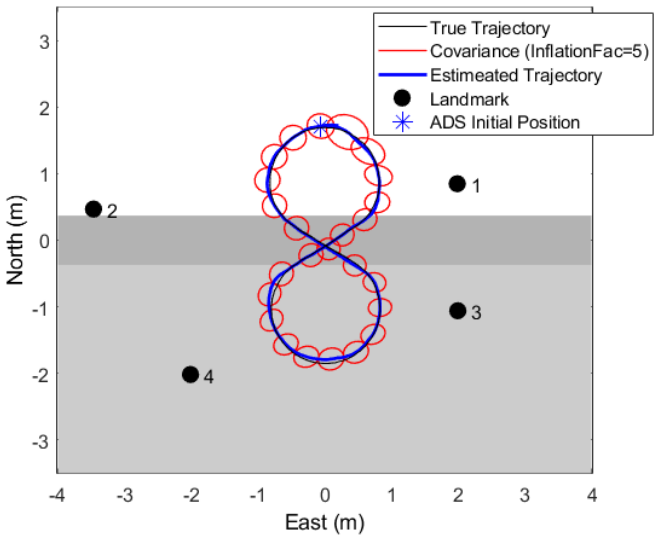

Figure 3.8: Estimated trajectory and covariance ellipses Using LiDAR/IMU.

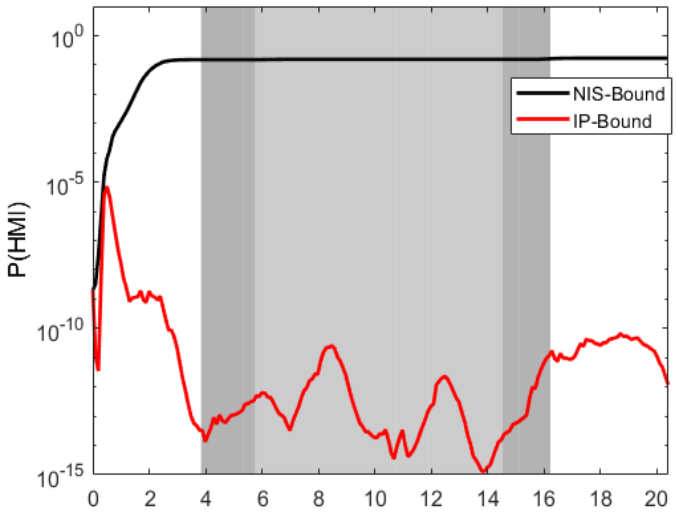

Figure 3.9: Integrity risk bounds for the NIS versus IP data association criteria using LiDAR/IMU.

Chapter 4

Spherical Grid-Based IMU/LiDAR Localization and Uncertainty Evaluation Using Signal Quantization

This paper describes the design, analysis, and experimental evaluation of a spherical-grid-based localization algorithm that leverages quantization theory to bound navigation uncertainty. This algorithm integrates data from Light Detection And Ranging (LiDAR) and inertial measuring units (IMU) in an iterative extended Kalman filter to estimate the position and orientation of a moving vehicle. An analytical bound is derived from the vehicles state estimation error, which accounts for both the random measurement noise and the loss of localization information caused by gridding. The performance of the proposed approach is analyzed and compared with that of a brute-force spherical grid-based method and a landmark-based method in an indoor environment while an outdoor experiment verifies the practicality of the method in a realistic driving scenario.

4.1 Introduction to Spherical Grid-Based IMU/LiDAR Localization

In this paper, we develop, implement, and evaluate a new point cloud (PC)-based localization algorithm integrating Light Detection And ranging (LiDAR) and inertial measuring units (IMU) using a signal quantizer and an iterative extended Kalman filter (IEKF). In prior work [Hassani and Joerger (2021)], we introduced a spherical grid-based localization (SGL) method to estimate position and orientation (or pose) corrections between a measured three-dimensional PC and a map-based predicted PC. These corrections were obtained by brute-force (BF) searching over candidate vehicle poses. In this work, we achieve SGL using an IEKF, which enables tight integration of LiDAR PC with IMU and prediction of pose estimation uncertainty. We develop an automated approach that locally adjusts the size of the grid cells to minimize the information loss due to gridding. In addition, we derive an analytical bound on the spherical gridding error and evaluate its impact on pose estimation error. These methods are tested using experimental data collected in both indoor and outdoor environments.

This research is intended for autonomous ground, air, and space vehicle navigation applications where localization uncertainty quantification is critical. In prior work [Hassani et al. (2019, 2018)], we developed and evaluated a landmark-based localization (LL) method, which required two intermediary pre-processing steps: feature extraction (FE) and data association (DA). FE finds viewpoint-invariant landmarks in the LiDAR PC, and DA assigns these extracted landmarks to mapped ones. FE and DA are computationally expensive and prone to faults in cluttered environments [Hassani et al. (2019); Joerger and Hassani (2020)].

LiDAR localization methods that do not require FE and DA include PC-matching algorithms, such as the widely-implemented iterative closest point (ICP) [Rusinkiewicz and Levoy (2001); Censi (2008); Diosi and Kleeman (2007)]. ICP can be computationally expensive and does not

enable reliable uncertainty prediction. We developed an SGL method to mitigate the computational burden of handling a three-dimensional LiDAR PCs thousands of high-update-rate data samples. The spherical grid in [Hassani and Joerger (2021)] is made of azimuth-elevation bins at regular angular intervals. In each bin, a point feature is selected and its distance to the spherical grids center point serves as range measurement. This gridding process is also applied to a PC map seen from the perspective of LiDAR's predicted pose. The measured PC can then be compared to the computed PC. The SGL's point-feature approach only provides a rough measure of navigation uncertainty [Hassani and Joerger (2021)]. Gridding and point selection can be improved, and rigorous error quantification has yet to be achieved.

In this paper, we develop a new PC spherical gridding approach that leverages a signal quantization technique used in data compression [Sayood (2017)]. This approach locally modifies grid spacing to reduce information loss and improve pose estimation without increasing computation cost. It also provides a deterministic bound on the range quantization error in each azimuth-elevation bin. In addition, we design an IEKF that tightly integrates IMUs with LiDAR SGL. The IMU facilitates the matching of measured versus computed PC whereas the SGL helps correct accelerometer and gyro biases. We validate these methods using experimental data collected on a sensor platform moving in both indoor and outdoor environments.

The first part of the paper aims at developing an advanced LiDAR PC spherical gridding process. We leverage quantization theory which is a well-studied topic in data transmission, compression, and classification [Sayood (2017); Max (1960)], information theory [Sabin and Gray (1986)], and finite element method for mesh generation [Du and Gunzburger (2002)]. We use it here to rearrange a spherical grid's discretized representation of the environment [Madisetti (2018); Gallager and Zheng (2006)]. The algorithm assigns a greater number of azimuth bins to parts of the environment that show larger geometric variations.

In the second part of the paper, we design an IEKF that incorporates the spherically gridded

LiDAR PC, IMUs, and their error models for the estimation and uncertainty quantification of a moving platform's pose, and of the IMU's accelerometer and gyroscope biases.

In the third part, we derive an upper bound on the impact of quantization errors on pose estimation uncertainty. In this preliminary algorithm, the estimated-state-level bound is achieved using a batch algorithm.

In the fourth part of the paper, we implement the IEKF-based IMU/LiDAR SGL algorithm by post-processing experimental data. In the indoor experiment, all objects in the environment are static, but they can get occluded or can get out of LiDAR's field of view as the sensor-platform moves. A probabilistic performance evaluation is conducted for the proposed IEKF-based SGL as well as for LL and brute-force SGL, to show the robustness of the new method in quantifying positioning uncertainty over multiple repeated trajectories. In the outdoor experiment, we drive a car equipped with IMU and LiDAR in a parking lot. Carrier phase differential GNSS (CPDGNSS) provides vehicle truth trajectory. We build an East-North-Up map of static sections of the environment using LiDAR measurements combined with CPDGNSS. Then, we use the map and the IEKF SGL for pose estimation and uncertainty quantification in a realistic driving scenario.

4.2 Spherical Gridding Using Signal Quantization

4.2.1 Quantization theory

Quantization is a process in which a large number of values is represented by a much smaller set of values [Sayood (2017)]. If the values that are quantized are scalars, then the process is called scalar quantization. The quantizer design aims at minimizing information loss. Figure 4.1 shows the parameters of a scalar quantizer.

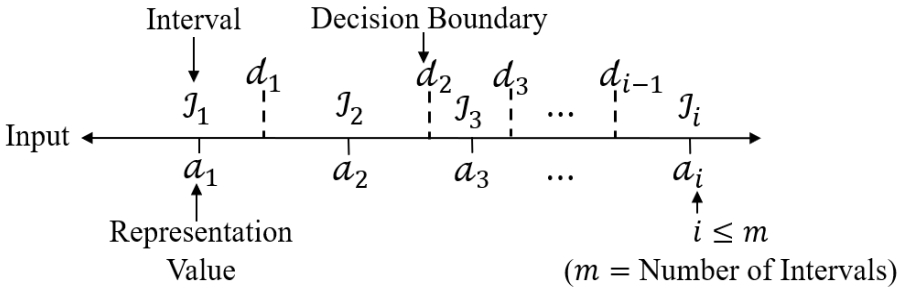

Figure 4.1: Scalar quantizer parameters

We define the following parameters:

Input: The input can be a set of deterministic or random values with an associated probability density function (PDF), i.e. R with PDF $f_R(r)$.

Interval: The interval partitions the input into separate ranges of values $\mathfrak{I} = \{\mathfrak{I}_i, \textit{ for } i = 1,\ldots,m\}$. Intervals are also known as Voronoi regions or encoders.

Representation value: The representation value is a single value selected for each interval. It is the output of the quantizer. Representation values are also known as decoders.

Decision Boundary: The limit value of an interval is a decision boundary. The number of decision boundaries is $m+1$, where m is the number of intervals.

The quantization process $Q(r)$ for an input r can be described as:

$$d_{i-1} < r < d_i \Longleftrightarrow Q(r) = a_i \tag{4.1}$$

In this research, the performance measure used to reduce information loss between quantizer input and output is the quantization distortion D defined as:

$$D = \frac{1}{M} \sum_{i=1}^{m} \sum_{r \in \Im_i} (r - a_i)^2 \tag{4.2}$$

where the right-hand side of equation (4.2) is the sum of the squared errors in each interval $\Im_i$ summed over all m intervals and divided by the total number of range measurements M. The number M is defined as $M = \sum_{i=1}^{m}$ where M_i is the number of range measurements per interval $\Im_i$, for $i = 1, \ldots, m$.

The quantization process can be described as follow. Given an input r and a number of intervals m find the values of d_i and a_i in each interval $\Im_i$, for $i = 1, \ldots, m$, that minimize the distortion D. There are two main categories of quantizers: uniform quantizers use fixed-size intervals, whereas non-uniform quantizers do not.

In this research, we use a Lloyd-Max quantizer, which is a practical non-uniform scalar quantizer. We will use LiDAR range measurements as input r, as further explained in Section 4.2.2. The Lloyd-Max quantization algorithm finds the values of a_i and d_i that minimize the distortion by taking the derivatives of D with respect to these parameters and setting them equal to zero. The values of a_i and d_i for a set of inputs r can be found using the following equations [Madisetti (2018)]:

$$a_i = \frac{1}{M_i} \sum_{r \in \Im_i} r \tag{4.3}$$

$$d_i = \frac{a_{i+1} + a_i}{2} \tag{4.4}$$

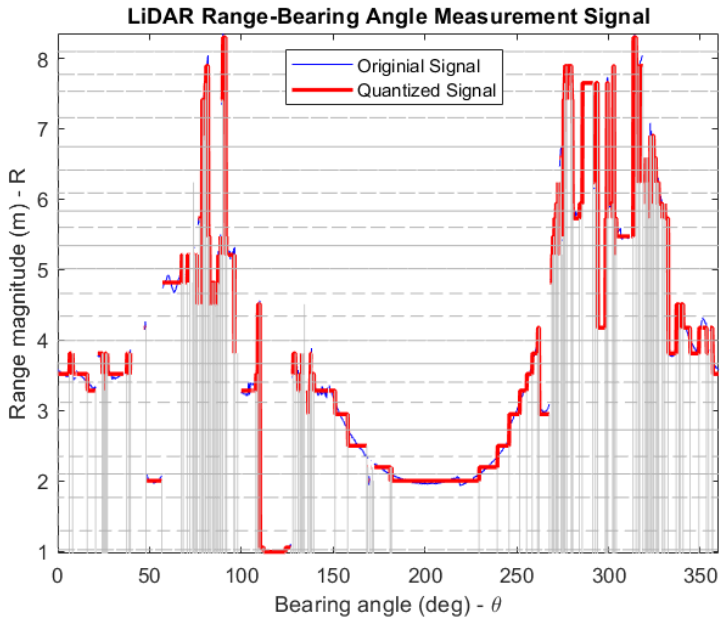

Figure 4.2: LiDAR scanned and quantized range measurements

For a Lloyd-Max quantizer, the representation values a_i in equation (4.3) are equal to the mean of the input values in interval i, and d_i in equation (4.4) is the mid-point of two neighboring representation values. Considering initial values for d_i and a_i, the minimization of D can be iteratively achieved [Sayood (2017); Madisetti (2018)].

4.2.2 Spherical grid design

In this section, we develop a novel approach that aims at applying quantization techniques borrowed from the signal processing field to LiDAR PCs. Data points are processed one elevation cone at a time using the approach described below. Instead of the traditional Cartesian representation of a LiDAR PC, we consider a range-versus-bearing-angle representation for a single elevation angle, and for 360-degree azimuth angles - which we call a single frame at that elevation. It is represented as a blue line in Figure 4.2, where the LiDAR scan (blue-colored curve) is interpreted as a range signal varying over azimuth angle.

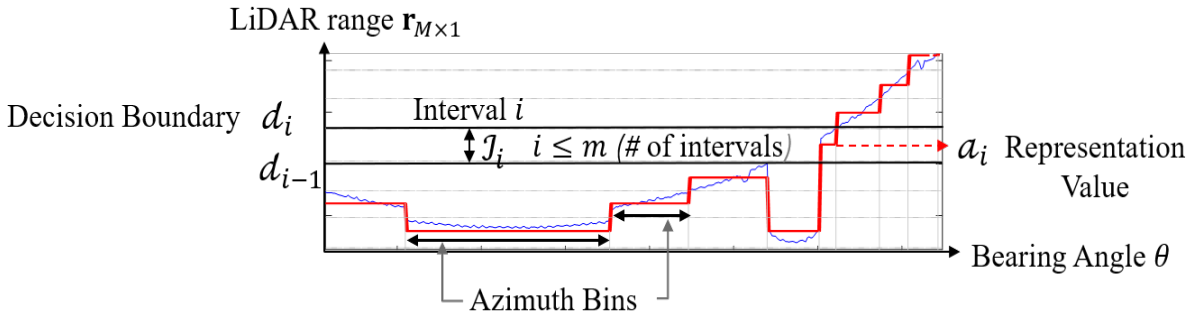

Figure 4.3: Quantizer parameter definition for LiDAR range vs. bearing angle measurements

Then, we use quantization theory to find the optimal decision boundaries d_i and representation values a_i, for $i = 1,\ldots,m$, which minimize the distortion D. These values are respectively represented in Figure 4.2 as horizontal dashed gray lines and red solid lines. The vertical solid gray lines show the boundaries of the azimuth bins, which are defined as bearing angle intervals with constant a_i-values (a change in a_i defines a new azimuth bin, even if that a_i-value defined a previous azimuth bin). Figure 4.3 shows the quantizer parameters and the azimuth bins in a zoomed-in region of the LiDAR range-versus-bearing-angle curve. Each azimuth bin provides a single range and bearing angle measurement. The range measurement is the value of a_i. In this implementation, we choose the bearing angle measurement to be that of the closest point to the LiDAR within that bin.

Figure 4.4 shows the output measurements in a cartesian coordinate system. This output is obtained after minor data trimming to exclude azimuth bins containing less than a minimum number of data points (which only seemed to add computation cost). The solid gray lines intersecting at the origin correspond to the vertical gray lines in Figure 4.2. In Figure 4.4, the LiDAR scan is represented with a blue curve, and the selected points after quantization are shown with red crosses. The zoomed-in window shows raw azimuth-range measurements in each bin and their corresponding quantized values. The azimuth bins in Figure4.4 are shown for a single elevation angle to facilitate visualization. However, in practice, we implement

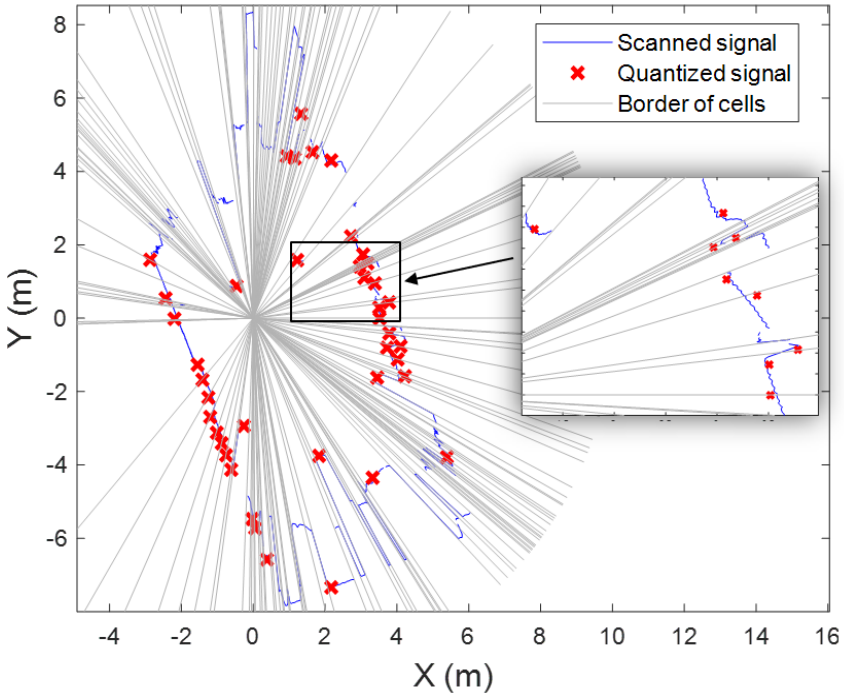

Figure 4.4: LiDAR scan and quantized signals (at 0-degree elevation; other elevation bins are not shown for clarity of exposition, but are quantized using the same process.)

azimuth binning at all elevations to construct a spherical grid.

4.2.3 Quantization error

The quantization error is defined as the difference between quantizer input r and output a_i. The quantization error b_i, for $i = 1, \ldots, m$, is defined as [Sayood (2017)]:

$$b_i = d_{i-1} - d_i \tag{4.5}$$

The decision boundaries d_i are given in equation (4.4). Quantization theory ensures that the following inequality is always satisfied:

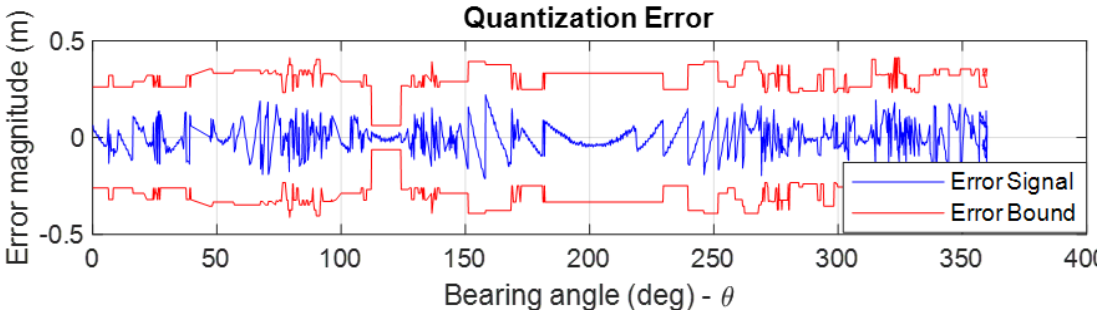

Figure 4.5: Quantization error and error bound for 360-degree measurements

$$|r - a_i| < b_i \tag{4.6}$$

Figure 4.5 shows quantization errors (blue) and error bounds (red) for all intervals in a frame. The red curve bounds the blue curve and is *known*.

The range measurement quantization errors bounding bias vector is defined as:

$$\mathbf{b}_k = [b_1 \ldots b_m \, \mathbf{0}_{1\times m}]^{\mathrm{T}} \tag{4.7}$$

where k is time epoch and b_i is a defined in equation (4.5). Zeros in equation (4.7) correspond to bearing angle measurements, which are not quantized in this work.

4.2.4 Applying a spherical grid to the map

We then apply the same spherical grid to the map PC. We first convert the map PC from the navigation frame to the sensor frame using the predicted state vector $\bar{\mathbf{x}}$ provided by the pose

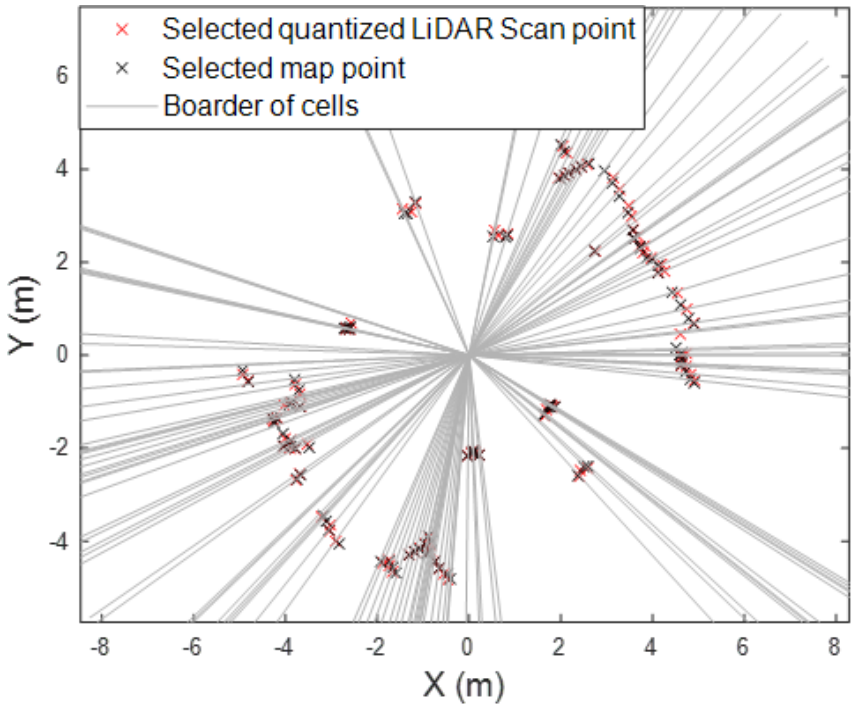

Figure 4.6: Applying the spherical grid to the map and selecting the points

estimation algorithm. Then, in each azimuth-elevation bin, we select the mapped point closest to the sensor. This approach automatically addresses occlusions of objects that may not be visible from the LiDARs current point of view. Figure 4.6 shows the LiDAR and map PCs after quantization. The azimuth bins are shown in gray.

4.3 Localization and Analytical Uncertainty Quantification

In this section, we design an IEKF which uses the mapped and sensed PCs output by the spherical gridding process. We also design a batch algorithm to bound the impact of range quantizer errors on pose estimation.

4.3.1 Vehicle linearized state propagation model

The localization algorithm uses the IMU measurements and error model to propagate vehicle pose between two LiDAR updates. The IMU states consist of vehicle position, velocity, orientation, and IMU biases. This section describes the continuous-time linearized state propagation model. The complete nonlinear continuous and discrete-time equations and sensor error models can be found in [Hassani et al. (2019); Titterton et al. (2004)]. In the following equations, the notation 'δ' indicates deviations of the state parameters relative to reference values about which linearization is performed.

$$\delta\dot{\mathbf{x}} = \mathbf{F}\delta\mathbf{x} + \delta\mathbf{w} \tag{4.8}$$

$$\delta\mathbf{x} = \begin{bmatrix} \delta\mathbf{x}_V^{\mathrm{T}} & \delta\mathbf{v}_V^{\mathrm{T}} & \delta\mathbf{e}_V^{\mathrm{T}} & \delta\mathbf{b}_{gy}^{\mathrm{T}} & \delta\mathbf{b}_{ac}^{\mathrm{T}} \end{bmatrix} \tag{4.9}$$

$$\mathbf{F} = \begin{bmatrix} \mathbf{0} & \mathbf{I} & \mathbf{0} & \mathbf{0} & \mathbf{0} \\ \mathbf{F}_{\mathrm{H2V}} & \mathbf{0} & [{}^{\mathrm{N}}\bar{\mathbf{f}}\times] & \mathbf{0} & \mathbf{C}_{\mathrm{B}}^{\mathrm{N}} \\ \mathbf{0} & \mathbf{F}_{\mathrm{V2T}} & -[{}^{\mathrm{N}}\boldsymbol{\omega}^{\mathrm{IN}}\times] & -\mathbf{C}_{\mathrm{B}}^{\mathrm{N}} & \mathbf{0} \\ \mathbf{0} & \mathbf{0} & \mathbf{0} & -\tau_{gy}^{-1}\mathbf{I} & \mathbf{0} \\ \mathbf{0} & \mathbf{0} & \mathbf{0} & \mathbf{0} & -\tau_{ac}^{-1}\mathbf{I} \end{bmatrix}, \quad \delta\mathbf{w} = \begin{bmatrix} \mathbf{0} \\ -\mathbf{C}_{\mathrm{B}}^{\mathrm{N}}\left((\delta\mathbf{S}_{ac} + \delta\mathbf{M}_{ac})\,{}^{\mathrm{B}}\bar{\mathbf{f}} + \mathbf{C}_{\mathrm{B}}^{\mathrm{N}}\boldsymbol{\nu}_{ac}\right) \\ \mathbf{C}_{\mathrm{B}}^{\mathrm{N}}\left((\delta\mathbf{S}_{gy} + \delta\mathbf{M}_{gy})\,{}^{\mathrm{B}}\bar{\boldsymbol{\omega}}^{\mathrm{IB}} + \boldsymbol{\nu}_{gy}\right) \\ \mathbf{n}_{gy} \\ \mathbf{n}_{ac} \end{bmatrix} \tag{4.10}$$

where

$\delta\mathbf{x}_V$ is the vehicle position expressed in navigation frame 'N',

$\delta\mathbf{v}_V$ is the vehicle velocity with respect to earth expressed in frame 'N',

$\delta\mathbf{e}_V$ is the attitude of the vehicle with respect to earth expressed in body frame 'B',

$\delta\mathbf{b}_{gy}$, $\delta\mathbf{b}_{ac}$ are the gyroscope's and accelerometer's time-varying bias vectors in frame 'B' respectively,

$\mathbf{F}_{\text{V2T}}$, $\mathbf{F}_{\text{H2V}}$ are defined in Appendix A,

${}^{\text{N}}\boldsymbol{\omega}^{\text{IN}}$ is the angular velocity vector of the inertial frame 'I' with respect to the frame 'N' expressed in frame 'N' [Hassani et al. (2018)],

${}^{\text{N}}\bar{\mathbf{f}}$ is the estimated specific force expressed in frame 'N',

$\mathbf{C}_{\text{B}}^{\text{N}}$ is the 3×3 rotation matrix from 'B' to 'N' [Titterton et al. (2004)],

${}^{\text{B}}\bar{\mathbf{f}}$ is the measured specific force vector at the IMU axis center w.r.t. frame 'I' expressed in frame 'B' [Titterton et al. (2004)],

${}^{\text{B}}\bar{\boldsymbol{\omega}}^{\text{IB}}$ is the measured angular velocity vector of frame B w.r.t frame 'I' expressed in frame 'B',

τ_{gy}, τ_{ac} are the gyroscope's and accelerometer's GMP time constants,

$\mathbf{S}_{gy}$, $\mathbf{S}_{ac}$ are the estimated gyroscope and accelerometer scale factors in frame 'B',

$\mathbf{M}_{gy}$, $\mathbf{M}_{ac}$ are the estimated gyroscope and accelerometer misalignment matrices in frame 'B',

$\boldsymbol{\nu}_{gy}$, $\boldsymbol{\nu}_{ac}$ are the gyroscope and accelerometer measurement white noise error components expressed in frame 'B',

$\mathbf{n}_{gy}$, $\mathbf{n}_{ac}$ are the gyroscope and accelerometer GMP time-uncorrelated driving noise vectors.

Considering the discrete-time expressions of the terms in equation (4.10) given in Appendix B, the discrete-time realization of equation (4.8) can be written as:

$$\delta \mathbf{x}_k + 1 = \mathbf{\Phi}_k \delta \mathbf{x}_k + \delta \mathbf{w}_k \tag{4.11}$$

where $\mathbf{\Phi}_k$ is the state transition matrix between time steps k and k+1 [Brown and Hwang (1992)].

4.3.2 Measurement models

In this section, we derive the nonlinear equations for the sensed and mapped PCs designed in Sections 4.2.2 and 4.2.4. Each mapped data point in navigation frame 'N' ${}^{\mathrm{N}}\mathbf{P}_j = [p_{E,j} \quad p_{N,j} \quad p_{U,j}]^{\mathrm{T}}$ for $j = 1 \dots N_m$, where N_m is the total number of mapped points, is projected in sensor frame using the following equations:

$${}^{\mathrm{S}}\mathbf{P}_j = \mathbf{C}_{\mathrm{N}}^{\mathrm{S}}({}^{\mathrm{N}}\mathbf{P}_j - \bar{\mathbf{x}}_V) \quad for \quad j = 1 \dots N_m \tag{4.12}$$

where deviations on $\mathbf{x}_V$ and $\mathbf{e}_V$ appear in the state error equation (4.9), and ${}^{\mathrm{S}}\mathbf{P}_j = [p_{1,j} \quad p_{2,j} \quad p_{3,j}]^{\mathrm{T}}$ is the mapped data point in sensor frame S, $\mathbf{C}_{\mathrm{N}}^{\mathrm{S}}$ is rotation matrix from navigation frame to sensor frame using $\bar{\mathbf{e}}_V$. We use the notations: $\bar{\mathbf{e}}_V = [\phi \quad \gamma \quad \psi]^{\mathrm{T}}$ and $\bar{\mathbf{x}}_V = [x_E \quad x_N \quad x_U]^{\mathrm{T}}$.

After applying the spherical grid to ${}^{\mathrm{S}}\mathbf{P}_{j=1\dots N_m}$, for each elevation range, we define the gridded points' ranges $\bar{r}_i$ and bearing angles $\bar{\theta}_i$, for i ranging from 1 to m, as:

$$\bar{r}_i = \sqrt{p_{1,j}^2 + p_{2,j}^2} + \nu_r \tag{4.13}$$

$$\bar{\theta}_i = \arctan\left(\frac{p_{2,j}}{p_{1,j}}\right) + \nu_\theta \tag{4.14}$$

where ν_r and ν_θ respectively are random range and bearing angle measurement errors,

We then stack the computed range and bearing angle measurements and define the mapped measurements at time step k as:

$$\mathbf{h}_k(\bar{\mathbf{x}})_k = [\bar{\mathbf{r}} \quad \bar{\boldsymbol{\theta}}]^{\mathrm{T}} \tag{4.15}$$

$$\bar{\mathbf{r}} = [\bar{r}_1 \ \dots \ \bar{r}_m]^{\mathrm{T}}, \quad \bar{\boldsymbol{\theta}} = [\bar{\theta}_1 \ \dots \ \bar{\theta}_m]^{\mathrm{T}}$$

The LiDAR range r_i and bearing angle θ_i are provided in the sensor frame. The $2m$ sensed measurement vector can be written as:

$$\hat{\mathbf{z}}_k = \mathbf{h}_k(\mathbf{x})_k + \nu_k \tag{4.16}$$

$$\hat{\mathbf{z}}_k = [r_1 \ \dots r_m \quad \theta_1 \dots \theta_m]^{\mathrm{T}} \tag{4.17}$$

$$\nu_k = [\, \nu_{r_1} \ldots \nu_{r_m} \quad \nu_{\theta_1} \ldots \nu_{\theta_m} \,]^{\mathrm{T}} \tag{4.18}$$

where

$\mathbf{x}_k$ is the state vector whose error vector is defined in equation (4.9),

$\boldsymbol{\nu}_k$ is the $2m \times 1$ measurement error vector modeled as a vector of zero-mean normally distributed random variables with covariance matrix $\mathbf{V}_k$. We use the notation: $\nu_k \sim \mathrm{N}(\mathbf{0}, \mathbf{V}_k)$.

We linearize equation (4.16) about our best pose prediction of the vehicle. The linearized range and angular measurement and measurement error vectors are respectively designated by $\delta\mathbf{R}$, $\delta\boldsymbol{\theta}$ and $\boldsymbol{\nu}_r$ and $\boldsymbol{\nu}_\theta$. The linearized LiDAR measurement equation can be written as:

$$\begin{bmatrix} \delta\mathbf{R} \\ \delta\boldsymbol{\theta} \end{bmatrix}_k = \begin{bmatrix} \mathbf{F}_{r,x} & \mathbf{0} & \mathbf{0} & \mathbf{0} & \mathbf{0} \\ \mathbf{F}_{\theta,x} & \mathbf{0} & -\mathbf{F}_{\theta,e} & \mathbf{0} & \mathbf{0} \end{bmatrix}_k \begin{bmatrix} \delta\mathbf{x}_V \\ \delta\mathbf{v}_V \\ \delta\mathbf{e}_V \\ \delta\mathbf{b}_{gy} \\ \delta\mathbf{b}_{ac} \end{bmatrix}_k + \begin{bmatrix} \boldsymbol{\nu}_r \\ \boldsymbol{\nu}_\theta \end{bmatrix}_k \tag{4.19}$$

where the coefficient matrices $\mathbf{F}_{r,x}$, $\mathbf{F}_{\theta,x}$ and $\mathbf{F}_{\theta,e}$ are determined using the state prediction vector as described in Appendix A.

4.3.3 Model-based estimator design

We develop an IEKF to tightly integrate LiDAR and IMU measurements and estimate vehicle pose. Figure 4.7 is a diagram of IEKF SGL including the spherical gridding and pose estimation processes. In the IEKF pose estimation block, the last term in the state vector estimation equa-

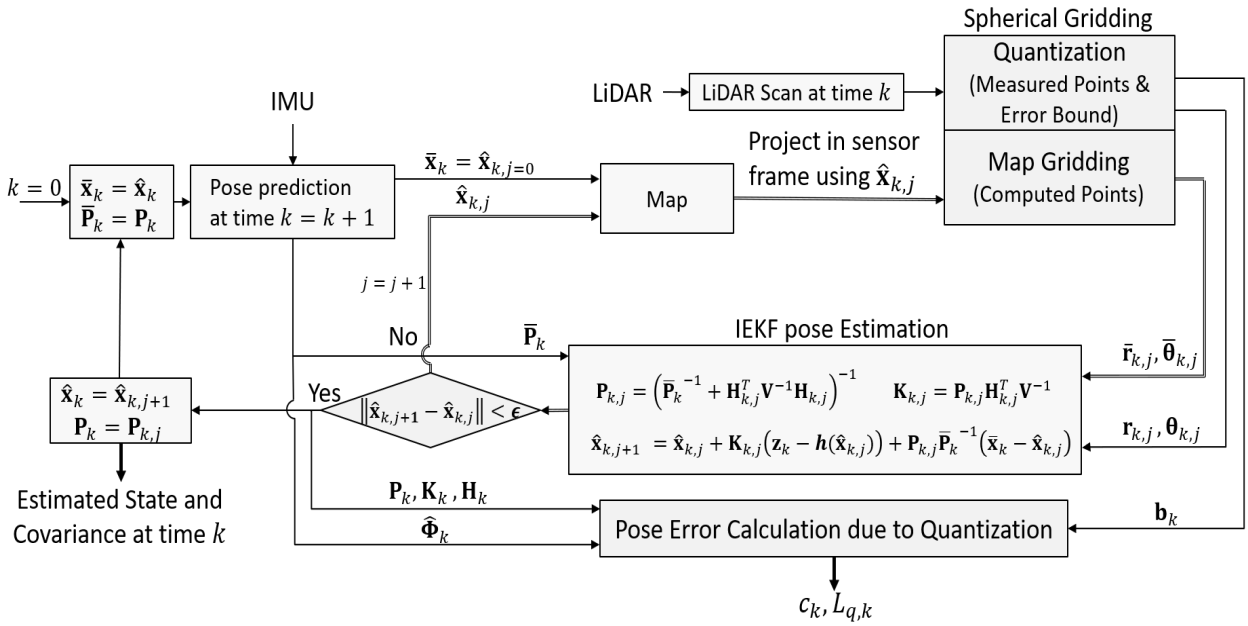

Figure 4.7: IEKF spherical grid-based localization diagram

tion improves the convergence of the iterative solution. The contribution to pose estimation error due to quantization is explained in section 4.3.4.

where

$\bar{\mathbf{x}}_k$ is the predicted state vector at time step k,

$\bar{\mathbf{P}}_k$ is the predicted covariance matrix at time step k,

$\hat{\mathbf{x}}_k$ is the estimated state vector at time step k,

$\mathbf{P}_k$ is the estimated covariance matrix at time step k,

$\mathbf{H}_k$ is the observation matrix defined in equation (4.19) at time step k,

$\mathbf{K}_k$ is the Kalman gain at time step k,

$\hat{\mathbf{\Phi}}_k$ is the discrete-time state transition matrix at time step k,

c_k is the expected error due to range quantization at time step k (explained in subsection 4.3.4),

$L_{q,k}$ is the estimation error bound for quantile q at time step k (explained in subsection 4.3.4),

4.3.4 Pose error due to quantization

In this section, we determine the impact of the quantization bias vector on state estimation error [Garcia Crespillo (2022)]. The expected value of the Kalman filter error in the presence of the bias $\mathbf{b}_k$ can be written as:

$$\mathrm{E}[\mathbf{x}_{k|k}] = (\mathbf{I} - \mathbf{K}_k \mathbf{H}_k)\, \hat{\mathbf{\Phi}}_k\, \mathrm{E}[\mathbf{x}_{k-1|k-1}] + \mathbf{K}_k \mathbf{b}_k \tag{4.20}$$

The impact of the quantization bias on the a-posteriori estimation of the state vector at time step k is [Tanl et al. (2018)]:

$$\mathrm{E}[\mathbf{x}_k] = [\mathbf{A}_{1k} \quad \dots \quad \mathbf{A}_{\mathrm{K}k}] \begin{bmatrix} \mathbf{b}_1 \\ \vdots \\ \mathbf{b}_k \end{bmatrix} = \mathbf{A}_{\mathrm{K}} \mathbf{b}_{\mathrm{K}} \tag{4.21}$$

where

$$\mathbf{A}_{mk} = \begin{Bmatrix} \left(\prod_{t=n}^{m+1} (\mathbf{I} + \mathbf{K}_n \mathbf{H}_n^{\mathrm{T}})\, \hat{\mathbf{\Phi}}_{k,m} \right) \mathbf{K}_m, & \text{if } m < n \\ \mathbf{K}_m & \text{if } m = k \end{Bmatrix} \tag{4.22}$$

In equation (4.21), bias vectors $\mathbf{b}_i$, for $i = 1, \dots, k$, are stacked from time step 1 to k in $\mathbf{b}_{\mathrm{K}}$, where K designates time steps $1, \dots, k$. We can express a bound on the impact of the range quantization bias on a state of interest, or a linear combination of states such as the cross-

track positioning coordinate for ground vehicle applications, as:

$$c_{s,k} = |\boldsymbol{\alpha}_s^{\mathrm{T}} \mathbf{A}_{\mathrm{K}}| \mathbf{b}_{\mathrm{K}} \tag{4.23}$$

where $\boldsymbol{\alpha}$ is a vector that extracts the state or state combination of interest from $\mathbf{x}_k$, i.e., consisting of a 1 for the desired state and zeros for all other states and '$|\bullet|$' is the element-wise absolute value operator. Calculating the c_k requires that we stack biases and estimator coefficients for time steps 1 to k. Appendix E shows the individual and total impacts of $|\mathbf{A}_{mk}|\mathbf{b}_k$ for $m = 1, ..., k$ on c_k projection in cross-track direction. Therefore, in future work, we will design a sliding time window or a recursive approach to address this problem.

The state estimation error variance for the state of interest is given by:

$$\sigma_{s,k}^2 = \boldsymbol{\alpha}_s^{\mathrm{T}} \mathbf{P}_k \boldsymbol{\alpha}_s \tag{4.24}$$

Both terms in equations (4.23) and (4.24) contribute to defining estimation error bounds for a desired confidence interval 'q'. The estimation error bound on a state of interest is defined as:

$$L_{q,k} = \lambda c_k + \kappa_q \sigma_k, \quad \text{with} \quad \lambda = \begin{cases} 1 & q \geq 50\% \\ -1 & q \leq 50\% \\ \textit{undef.} & q = 50\% \end{cases} \tag{4.25}$$

where κ_q is a confidence multiplier for selected quantile q $\left(\kappa_q = \Phi^{-1}(q)\right)$ and $\Phi^{-1}(\,)$ is the inverse of cumulative distribution function (CDF) for a standard normal distribution. For example, we can determine the 84% and 16% quantiles of the estimation error bounds as:

$$L_{84\%,k} = c_k + \sigma_k \tag{4.26}$$

$$L_{16\%,k} = -(c_k + \sigma_k) \tag{4.27}$$

where the impact of the quantization error c_k is accounted for in a worst-contributing manner to guarantee a bound on the actual error quantiles. If $c_k = 0$, then the range $L_{16\%,k}$ to $L_{84\%,k}$ defines a 1σ (68%) error envelope on the state of interest.

4.4 Experimental Evaluation of Spherical Grid-Based Localization

In this section, we carry out two sets of experiments: first, in a structured indoor environment with recognizable landmarks to facilitate performance comparisons between SGL and LL; then, in a realistic outdoor automotive navigation environment.

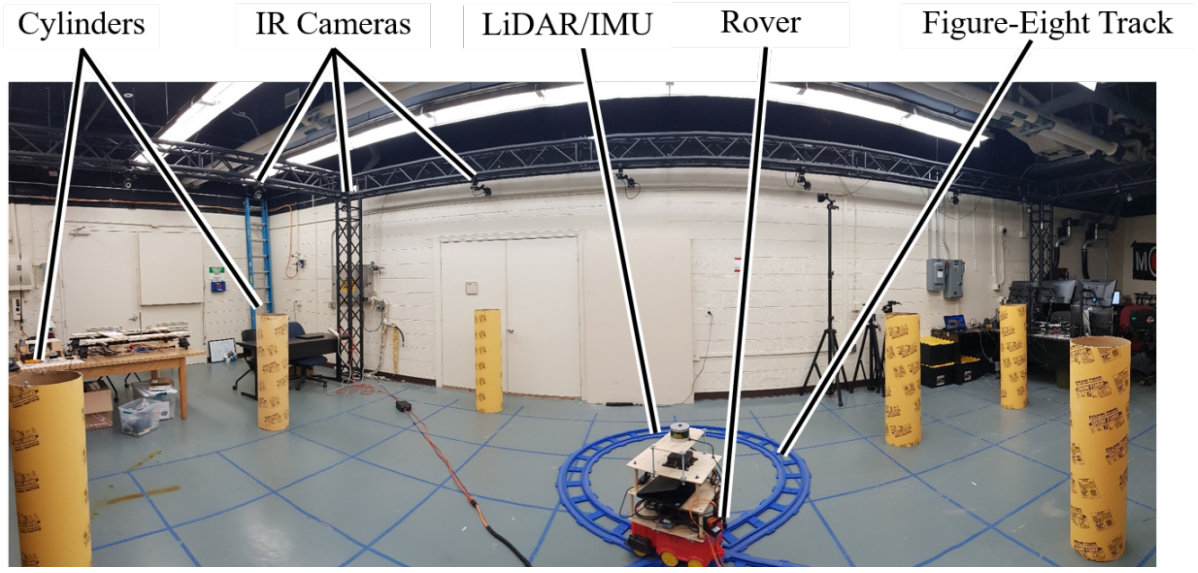

Figure 4.8: Indoor testbed overview

4.4.1 Indoor testing for experimental validation in a structured environment

We first process the experimental data collected using the testbed in Figure 4.8 [Hassani et al. (2019)]. It includes a sensor platform moving on a figure-eight track and equipped with a Velodyne VLP-16 Puck LTE LiDAR, and a NovAtel IMU-IGM-A1. Sixteen Optitrack Prime 13W infrared (IR) motion capture cameras provide sub-centimeter-level positioning by tracking retro-reflective markers fixed on the rover. Vertical cardboard cylinders surround the figure-eight track and occlude each other as the platform passes by. These cylinders' features are extracted to serve as landmarks for the LL method. In contrast, the IEKF SGL algorithm leverages most of the LiDAR PC, excluding returns from the lab floor but including returns from walls and furniture as well as cylinders. Testbed settings and parameter values are listed in Table 4.1.

Figure 4.9 shows a top view of the true-versus-estimated rover trajectories. The SGL trajectory is shown by a red line and the LL trajectory is shown by a dashed green line. All trajectories are

Table 4.1: Indoor experiment settings

Systems Parameters	**Values**
Range measurement standard deviation	0.04 m
Bearing angle measurement standard deviation	3 °
Initial position standard deviation	0.5 m
Initial velocity standard deviation	0.05 m/s
Initial heading standard deviation	10 °
Initial Roll/pitch standard deviation	1 °
Accelerometer velocity random walk	30 m/s/$\sqrt{\text{hr}}$
Gyroscope angle random walk	100 °/$\sqrt{\text{hr}}$
Accelerometer GMP bias correlation time constant	3600 s
Gyroscope GMP bias correlation time constant	3600 s
Standard deviation of accelerometer GMP bias	0.67 m/s^2
Standard deviation of gyroscope GMP bias	10°
IMU sampling time	0.01 s

overlapped for most of the time. The map used for LL comprises the center-point coordinates of the six cylindrical landmarks shown with black circles. In contrast, the map used for SGL uses the PC represented with blue crosses. A color-coded background is used to facilitate the interpretation of subsequent figures over time: the upper loops background is shown in white, the lower loop in light gray, and the straight segments in dark gray. The initial position of the rover is also shown with a black cross.

Figure 4.10(a) shows cross-track SGL errors over time for experimental data collected over 80 laps. The sample cross-track positioning error is color-coded in shades of gray, from white to black as the rover travels from the first to the last lap: slight differences in performance are observed in the early laps as compared to the later ones because of the sensor system's warm-up period. The blue-colored envelope represents the error bounds in equations (4.26) and (4.27). They are represented with an area whose boundaries are the minimum and maximum $L_{84\%,k}$ and $L_{16\%,k}$ values over the 80 laps at trajectory time k. The solid red line is the empirical 68%-error envelope (i.e., the 84% and 16% sample quantiles), which is bounded by the analytical

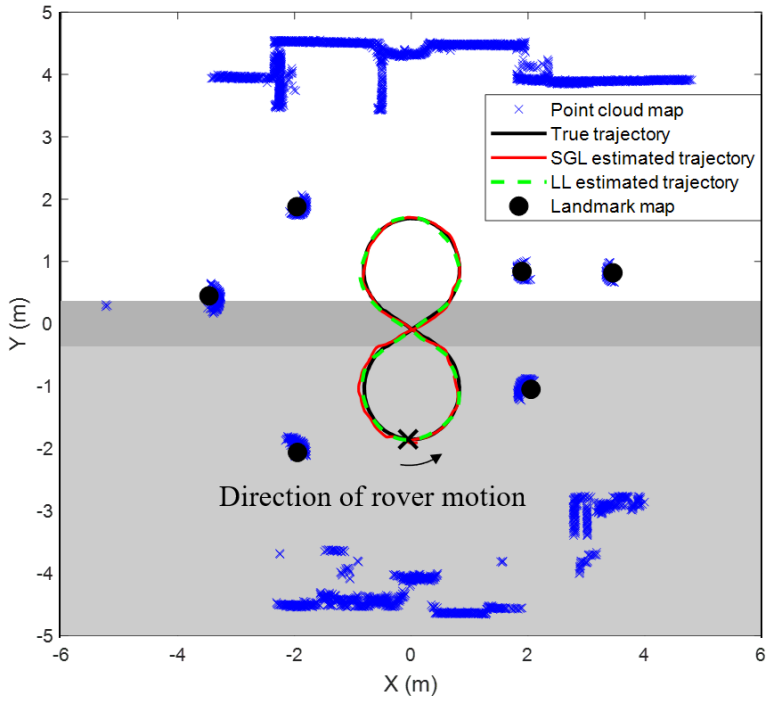

Figure 4.9: IEKF spherical grid-based localization performance for a single lap estimation of rover position

blue envelope for most of the 22-second-long trajectory. The looseness of the blue bound with respect to the red one captures our limited knowledge of the spherical grid quantization error.

Figure 4.10(b) shows error bounds for the rover's heading angle estimation. In this case, again, the analytical envelope bounds the sample error envelope for most of the trajectory. In addition, the smaller difference between the blue area and red line in the heading error in comparison with the cross-track error is because the range quantization mostly impacts the rover's position states and its impact on the heading error is due to the coupling of the rover's states. The LiDAR's bearing angle resolution error and the rover's heading prediction error have the main contributions to the analytical error envelope of the heading angle.

In Table 4.2, we compare the performance of landmark-based localization (LL), brute-force spherical-grid-based localization (BF-SGL) [Hassani and Joerger (2021)], and IEKF SGL. For

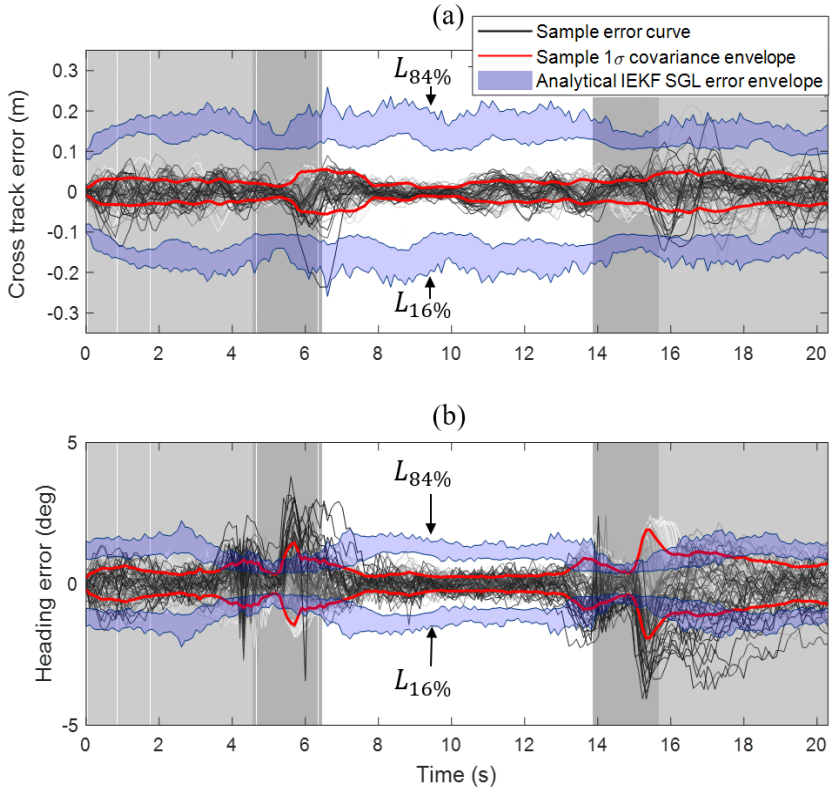

Figure 4.10: IEKF spherical grid-based localization errors and error bounds for the rover's (a) cross-track and (b) heading angle estimation performance

each approach, the table gives the cross-track error bounds derived from the maximum-over-the-trajectory of the 16%-to-84% quantile deviation; for LL, which is not affected by quantization/gridding errors, this metric is equal to the 1σ error bound. Table 4.2 also lists the single-lap-computation time, which was evaluated using a 4-GHz processor with 32-GB RAM under a 64-bit Windows operating system. The maximum error bound for LL is 5 cm: LL requires feature extraction (FE) and data association (DA) that introduce additional risks [Hassani and Joerger (2021); Hassani et al. (2019)]. These risks are not easily captured using the position-domain metrics in Table 4.2, and are therefore not accounted for in the Table. The BF-SGL error bound is also 5 cm. BF-SGL does not require FE and DA, but it only provides a 1-sigma bound with no means to account for gridding errors, which underestimates the localization

Table 4.2: Comparison of the 16%-to-84% quantile deviation bounds in cross-track and computation times over a single lap for three different localization algorithms.

Localization Method	Max of 16%-to-84% Quantile Dev.	Computation Time (Single Lap)
Landmark-bases	0.05 m*	4s
Brute Force SGB	0.05 m**	20s
IEKF SGB	0.26m	9s

*: does not account for feature extraction and data association errors
**: does not account for gridding errors

error. Finally, the IEKF SGL provides a maximum 84% quantile bound of 26 cm: in this case, spherical gridding errors are accounted for.

The longest computation time is needed for BF SGL. It is determined by the size and resolution of the vehicle pose candidate search space, and by that of the fixed-size azimuth-elevation grid. The automated grid size/resolution selection of IEKF SGL reduces the computation load to half that of BF SGL. The LL has the lowest computation time because it only processes a small subset of data points corresponding to extracted landmarks.

4.4.2 Outdoor testing in a realistic automotive environment

Figure 4.11 displays an outdoor sensor platform that includes the NovAtel IMU-IGM-A1 used in the indoor test, a NovAtel ProPack6 GNSS receiver and antenna, and an Ouster OS1-64 LiDAR. The sensor platform is mounted on a car's roof rack. A differential code and carrier phase GNSS reference station is installed at a nearby pre-surveyed location. Sensor data is collected on a laptop computer using ROS (the Robotic Operating System). We use ROS to time-tag and record sensor data for post-processing. "Truth" vehicle position and orientation are determined using NovAtel's synchronous position, attitude, and navigation (SPAN) solution, which tightly integrates IMU with carrier phase differential GNSS. This section evaluates the performance of an IEKF SGL algorithm using LiDAR/IMU; the test settings and LiDAR and

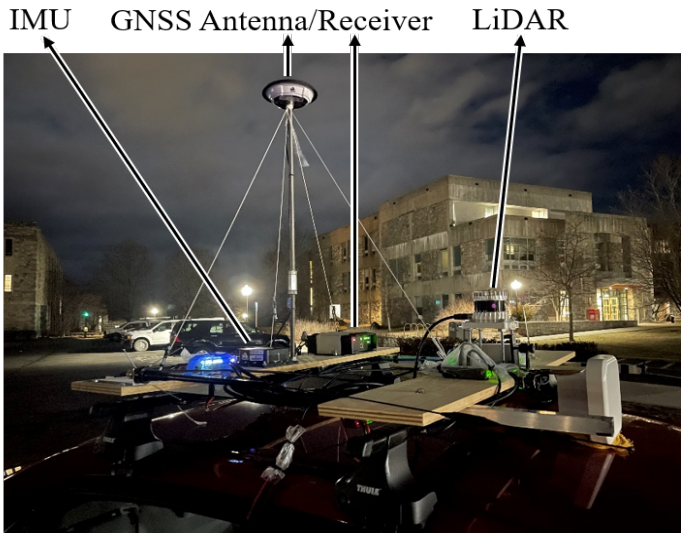

Figure 4.11: Outdoor test equipment overview

IMU parameter values are listed in Table 4.3.

Figure 4.12(a) is the 3D point cloud map of the test site where height is color-coded: measurements between 2-meter and 18-meter height were included. Figure 4.12(b) shows the test site, which is a parking lot on Virginia Tech's Blacksburg campus. The PC map is rough, which will accentuate localization errors and the need for realistic error bounds while achieving submeter-level accuracy. The map uses a limited subset of LiDAR measurements converted from the moving sensor frame to East-North-Up (ENU) navigation frame using the truth solution.

Mapping errors include deviations in the reference "truth" solution, imperfect sensor's time synchronization, errors caused by non-stationary objects (including vegetation), and poor, noisy, and inconsistent returns from surfaces with varying retro-reflectivity properties, in particular those we observed from window glass. In addition, in this first outdoor experiment, we did not implement motion compensation: we did not account for vehicle motion over 0.1-second-long 360-degree LiDAR scans. We will consider improving the map in future work; this is not essential in this paper because the emphasis is placed on error bounding rather than

Table 4.3: Outdoor experiment settings

Systems Parameters	**Values**
Ranging measurement standard deviation	0.4 m
Bearing angle measurement standard deviation	20°
Laser data sampling interval	0.1 s
Initial position standard deviation	0.5 m
Initial velocity standard deviation	0.05 m/s
Initial heading standard deviation	10 °
Initial Roll/pitch standard deviation	1 °
Accelerometer velocity random walk	30 m/s/$\sqrt{\text{hr}}$
Gyroscope angle random walk	140 °/$\sqrt{\text{hr}}$
Accelerometer GMP bias correlation time constant	3600 s
Gyroscope GMP bias correlation time constant	3600 s
Standard deviation of accelerometer GMP bias	0.67 m/s^2
Standard deviation of gyroscope GMP bias	10°
IMU sampling time	0.005 s

error reduction. The range and bearing angle measurement standard deviations in Table 4.3 are selected properly to address the mapping errors.

Figure 4.13 shows a top-view of the rover trajectory for a single lap in the parking lot. Vehicle pose is estimated using LiDAR and IMU data processed using the IEKF SGL algorithm. The true and estimated trajectories overlap. The initial position of the vehicle is indicated with a black cross.

Figure 4.13 also shows magenta covariance ellipses that roughly represent the two-dimensional positioning uncertainty for vehicle locations taken at regular 0.5 s intervals. Covariance ellipses are inflated by a factor of thirty to facilitate visualization. These ellipses are optimistic and underestimate localization errors because they do not account for gridding errors. The vehicle pose estimation performance depends on the geometry of the objects and buildings surrounding the LiDAR. Further testing is needed to capture the variety of geometries that a LiDAR may observe in its operating environment.

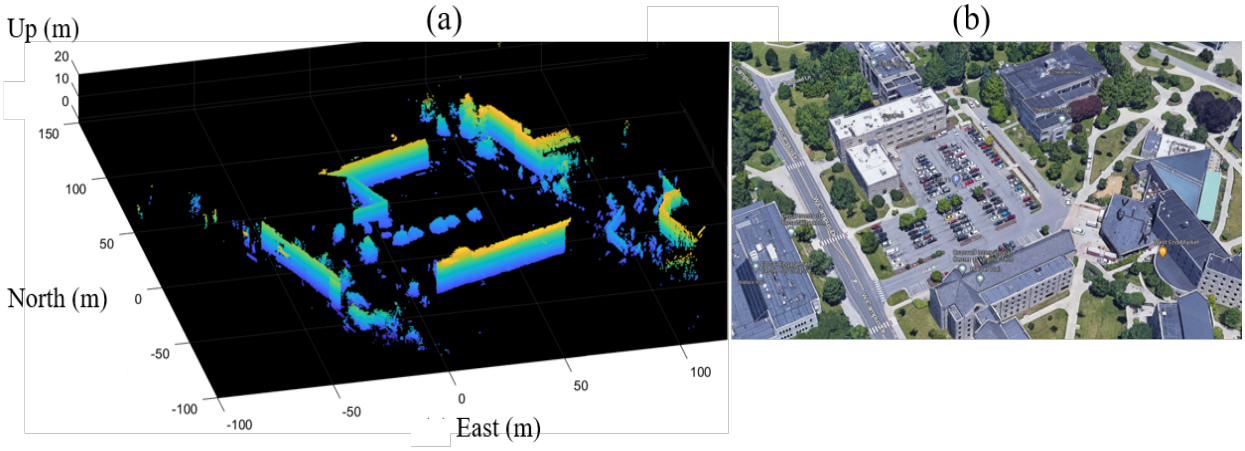

Figure 4.12: Three-dimensional point cloud map used in the outdoor experiment

Figure 4.14(a) shows the cross-track error over time. The sample cross-track positioning error is shown with black cross markers. The blue-colored curves represent the upper and lower IEKF SGL error bounds $L_{84\%,k}$ and $L_{16\%,k}$ in equations (4.26) and (4.27), respectively. The black sample error curve is bounded by the blue submeter analytical bounds over the 41-second-long trajectory. The magenta line is the 1σ (68%) error covariance envelope which grossly underestimates localization errors by not considering the uncertainty caused by gridding.

Figure 4.14(b) shows the error, error covariance envelope, and error bounds for the vehicle heading angle. In this case, again, the blue analytical IEKF SGL error bounds better represent the black sample errors than the magenta covariance envelope.

In Figure 4.14, the increase in cross-track position and heading angle estimation errors occurs as the vehicle turns as highlighted with a dashed white ellipse in Figure 4.13. During this time period, the errors due to lack of motion compensation are accentuated by the vehicle's rotation and are significantly higher as compared to other segments of the trajectory. This effect will be mitigated in future work by implementing motion compensation (Ollero et al., 2004; Li et al., 2016; Meng et al., 2021).

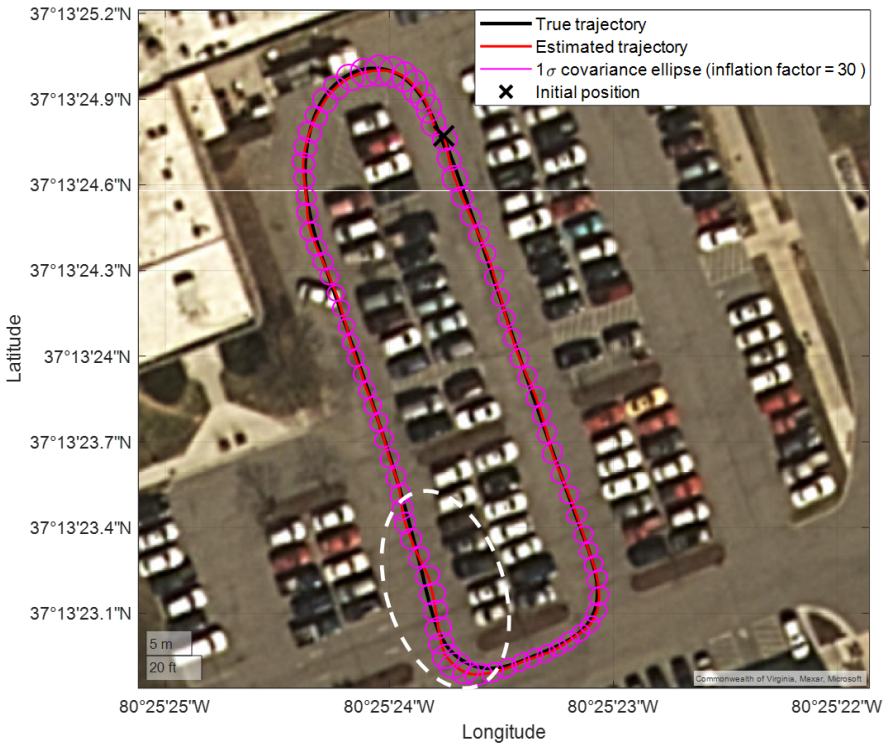

Figure 4.13: LiDAR/IMU-based IEKF spherical grid-based vehicle localization performance during testing in an outdoor environment

In addition, a smaller difference between the blue and magenta error covariance envelopes is observed for the heading angle as compared to the cross-track deviation. This is because range quantization mostly impacts the vehicle's position states. Its impact on heading estimation is indirect, through the coupling of the vehicle and heading angle states in matrix $\mathbf{A}_{\mathrm{K}}^{\mathrm{T}}$ in equation (4.23).

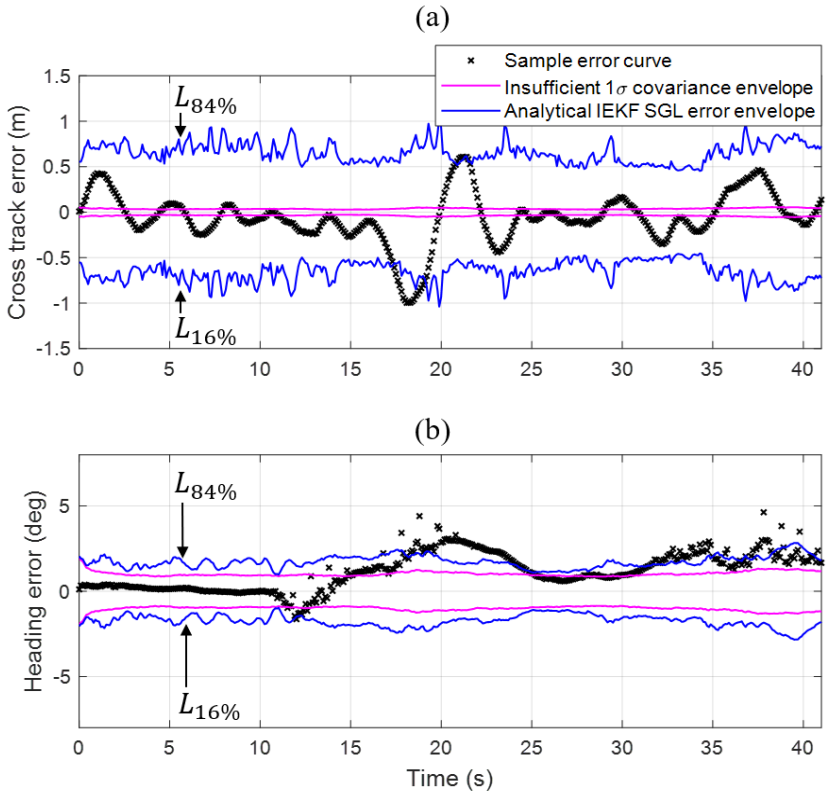

Figure 4.14: IEKF spherical grid-based localization error bounds for the vehicle (a) cross-track positioning error (b) heading angle estimation error estimation

4.5 Conclusion for Spherical Grid-Based IMU/LiDAR Localization

In this paper, we developed a tightly-integrated, spherical-grid-based LiDAR/IMU localization (SGL) algorithm that provides an analytical bound on the positioning error. The algorithm leverages signal quantization theory to limit the amount of LiDAR data processing while minimizing the loss of information. In addition, we designed an iterative extended Kalman filter (IEKF) to estimate vehicle pose and predict pose uncertainty. We derived an analytical bound on pose estimation errors that accounts for both the IEKF covariance and gridding errors.

Experimental evaluation was performed (a) in an indoor environment using data collected by a rover traveling 80 times along the same, repeated trajectory, and (b) in an outdoor parking lot using data collected by sensors installed on a car. Indoor testing showed that IEKF spherical grid-based localization provides a more realistic positioning error bound than landmark-based and brute-force spherical grid localization approaches without causing significant additional computation costs. Outdoor testing validated the IEKF-based SGL in a realistic driving environment.

Chapter 5

Conclusions and Future Work

5.1 Dissertation Conclusion

Ensuring the safety of automated driving systems (ADS) requires the quantification of navigation uncertainty. ADS testing is necessary, but insufficient to provide navigation safety guarantees because accumulating autonomously-driven road miles does not provide a statistically significant number of traveled miles as compared to manned driving incidents [Kalra and Paddock (2016); Kalra and Groves (2017)].

In response, we leverage prior work in aviation where navigation safety is measured in terms of 'integrity'. Integrity is a measure of trust in sensor information. Unfortunately, the same methods do not directly apply to ADS, because ground vehicles operate under sky-obstructed areas where GNSS signals can be altered or blocked by buildings and trees.

In prior work, we developed a new safety risk evaluation method for landmark-based localization (LBL), which requires feature extraction (FE) and data association (DA). First, FE finds recognizable landmarks with LiDAR-viewpoint-invariant features in the LiDAR Point cloud (PC). Then DA assigns these measured landmarks to the mapped ones. FE and DA are computationally expensive and, in the presence of sensor noise and cluttered environments, are prone to faults, which can cause an ADS to crash.

In response, we proposed new methods that could reduce the integrity risk by improving DA:

first, by integrating LiDAR and IMU; second, by exploiting LiDAR return-light intensity; third, by developing a new criterion based on extended Kalman filter (EKF) innovation projections to reduce the risk of wrong association.

In addition, we developed a spherical grid-based localization (SGL) method that leverages a signal quantization technique used in data compression. This SGL data processing pipeline is more direct than that of LBL, but it can be computationally expensive. Our approach locally modifies grid spacing to reduce computation cost while limiting information loss. In addition, it provides a deterministic bound on the range quantization error. We designed an iterative EKF that tightly integrates IMU with LiDAR SGL and provides an analytical error bound on ADS pose (position and orientation) estimation.

5.2 Summary of Achievements

We developed high-integrity IMU/LiDAR-based navigation algorithms that achieve the following objectives:

- Improving vehicle pose prediction, data association, and landmark-based localization (LBL) integrity evaluation using tight integration of LiDAR and IMU.
- Quantifying and reducing the risks of wrong associations and LBL integrity risks using LiDAR intensity measurements.
- Deriving a new data association criterion which uses the projections of the EKF innovation vector to provide tighter LBL integrity risk bounds as compared to using the normalized innovation squared (NIS) criterion.
- Developing a new spherical grid-based localization (SGL) method that enables uncer-

tainty quantification. This method leverages a signal quantization technique to reduce computation cost while limiting information loss and providing an analytical bound on pose estimation errors.

- Experimental testing to validate the above methods in controlled indoor lab environments and in realistic outdoor driving environments.

5.3 Future Work

Future work may include further improvements in localization and uncertainty quantification algorithms, and algorithm testing capabilities to strengthen algorithm validation.

Future research objectives include:

Improving our current testbeds: A short-term objective for future work could be the implementation of motion compensation in LiDAR point clouds, i.e., accounting for vehicle motion during the 0.1-second, 360-degree LiDAR scanning rotation. In this dissertation, the lack of motion compensation, especially during vehicle turns, impacted both mapping and vehicle pose estimation in indoor and outdoor experiments. This issue could be addressed as the next step of this research.

Developing other new multi-sensor integration schemes: Other tightly-integrated multi-sensor systems have yet to be explored. For example, we have not exploited carrier phase differential GNSS (CPDGNSS) other than to build the LiDAR point-cloud-map, and during testing, to determine the true vehicle trajectory. Another example is automotive RADARs. They provide high-update rate velocity measurements that are intended for collision warning and obstacle avoidance but could contribute to navigation performance if cleverly integrated. We have installed and synchronized a RADAR on the out-

door platform. However, its measurements are not yet integrated with LiDAR and IMU. We could, in the near-term future, evaluate tight CPDGNSS/LiDAR/IMU/RADAR integration and expand both LL and SGL methods to quantify the uncertainty reduction brought about by additional sensors.

Using vision and digital LiDAR images: Vision-based navigation is extremely popular in automotive and uncrewed air vehicle applications; early papers on vision-based integrity have even started appearing [Zhu et al. (2020)]. In addition, digital LiDARs provide fixed-resolution depth images, signal images, and ambient images in real-time. These images are derived from the point cloud that we are already using. If we were to use both the images and the point cloud, we would need to carefully consider their correlation. Still, using the images would let us leverage advanced vision-based algorithms, for example, vision-based feature extraction methods that could then help us identify landmarks in the point cloud. Uncertainty quantification incorporating this new technology is an open research area.

Advancing map quality and mapping technology: Simultaneous Localization and Mapping is an attractive and popular technology for autonomous LiDAR navigation. However, our experience shows that SLAM algorithm errors accumulate as localization errors build upon mapping errors–they grow unbounded without loop-closure or external reference points. Regardless of our own experience, if we cannot quantify safety when a map is available, then we will probably not be successful without a map. The starting point is to use maps. In this context, the SGL algorithm validation in Chapter 4 relied on a map. This map can be significantly improved. The quality of the map was degraded by imperfect time synchronization between the true pose data and LiDAR measurements, laser beam diffractions through building windows, and laser multipath due to the reflective objects. Therefore, developing new algorithms and exploiting new technologies to pro-

vide high-resolution, high-quality maps are necessary. Building and updating static or dynamic maps in different formats (i.e. point cloud or geometric features) and over large areas is challenging. Many autonomous driving system developers are looking for mapping engineers to address these challenges which makes it a topical long-term research direction for future work.

Bibliography

Guillermo Duenas Arana, Osama Abdul Hafez, Mathieu Joerger, and Matthew Spenko. Recursive integrity monitoring for mobile robot localization safety. In *Proceedings - IEEE International Conference on Robotics and Automation*, volume 2019-May, 2019. doi: 10.1109/ICRA.2019.8794115.

Guillermo Duenas Arana, Osama Abdul Hafez, Mathieu Joerger, and Matthew Spenko. Integrity monitoring for kalman filter-based localization. *International Journal of Robotics Research*, 39, 2020. ISSN 17413176. doi: 10.1177/0278364920960517.

Javier A Areta, Yaakov Bar-Shalom, and Ron Rothrock. Misassociation probability in m2ta and t2ta. *J. Adv. Inf. Fusion*, 2:113–127, 2007.

Tim Bailey. *Mobile robot localisation and mapping in extensive outdoor environments*. Doctoral dissertation, University of Sydney, 2002. URL https://www-personal.acfr.usyd.edu.au/tbailey/techreports/phdthesis.htm.

Yaakov Bar-Shalom, Fred Daum, and Jim Huang. The probabilistic data association filter. *IEEE Control Systems Magazine*, 29, 2009. ISSN 08880611. doi: 10.1109/MCS.2009.934469.

Yaakov BarShalom, Thomas E. Fortmann, and Peter G. Cable. Tracking and data association. *The Journal of the Acoustical Society of America*, 87(2):918–919, 1990. doi: 10.1121/1.398863.

Charlie T Bellows. *Leveraging external sensor data for enhanced space situational awareness*. Doctoral dissertation, AIR FORCE INSTITUTE OF TECHNOLOGY WRIGHT-PATTERSON AFB, 2015. URL https://scholar.afit.edu/etd/1926/.

Ola Bengtsson and Alert Jan Baerveldt. Robot localization based on scan-matching - estimating the covariance matrix for the idc algorithm. In *Robotics and Autonomous Systems*, volume 44, 2003. doi: 10.1016/S0921-8890(03)00008-3.

Borna Bicanic, Marin Orsic, Ivan Markovic, Sinisa Segvic, and Ivan Petrovic. Pedestrian tracking by probabilistic data association and correspondence embeddings. In *FUSION 2019 - 22nd International Conference on Information Fusion*, 2019. doi: 10.23919/fusion43075.2019.9011317.

Juan Blanch, Todd Walter, and Per Enge. Gaussian bounds of sample distributions for integrity analysis. *IEEE Transactions on Aerospace and Electronic Systems*, 55(4):1806–1815, 2019. doi: 10.1109/TAES.2018.2876583.

Guillaume Bresson, Thomas Féraud, Romuald Aufrère, Paul Checchin, and Roland Chapuis. Real-time monocular slam with low memory requirements. *IEEE Transactions on Intelligent Transportation Systems*, 16(4):1827–1839, 2015. doi: 10.1109/TITS.2014.2376780.

Robert Grover Brown and Patrick Y. C. Hwang. *Introduction to random signals and applied kalman filtering*, volume 2. John Wiley, 1992.

Han Cai, Yang Yang, Steve Gehly, Suqin Wu, and Kefei Zhang. Improved tracklet association for space objects using short-arc optical measurements. *Acta Astronautica*, 151, 2018. ISSN 00945765. doi: 10.1016/j.actaastro.2018.07.024.

Andrea Censi. An icp variant using a point-to-line metric. In *2008 IEEE International Conference on Robotics and Automation*, pages 19–25, May 2008. doi: 10.1109/ROBOT.2008.4543181.

Fang Cheng Chan, Mathieu Joerger, Samer Khanafseh, and Boris Pervan. Bayesian fault-

tolerant position estimator and integrity risk bound for gnss navigation. *Journal of Navigation*, 67, 2014. ISSN 14697785. doi: 10.1017/S0373463314000241.

Jaebum Choi, Simon Ulbrich, Bernd Lichte, and Markus Maurer. Multi-target tracking using a 3d-lidar sensor for autonomous vehicles. In *IEEE Conference on Intelligent Transportation Systems, Proceedings, ITSC*, 2013. doi: 10.1109/ITSC.2013.6728343.

Aron Jace Cooper. A comparison of data association techniques for simultaneous localization and mapping. Doctoral dissertation, Massachusetts Institute of Technology, 2005. URL https://dspace.mit.edu/handle/1721.1/32438?show=full.

Bruce DeCleene. Defining pseudorange integrity - overbounding. *Proceedings of the 13th International Technical Meeting of the Satellite Division of The Institute of Navigation (ION GPS 2000)*, September 2000.

Ayush Dewan, Tim Caselitz, Gian Diego Tipaldi, and Wolfram Burgard. Motion-based detection and tracking in 3d lidar scans. In *Proceedings - IEEE International Conference on Robotics and Automation*, volume 2016-June, 2016. doi: 10.1109/ICRA.2016.7487649.

Albert Diosi and Lindsay Kleeman. Laser scan matching in polar coordinates with application to slam. In *2005 IEEE/RSJ International Conference on Intelligent Robots and Systems, IROS*, 2005. doi: 10.1109/IROS.2005.1545181.

Albert Diosi and Lindsay Kleeman. Fast laser scan matching using polar coordinates. *The International Journal of Robotics Research*, 26(10):1125–1153, 2007. doi: 10.1177/0278364907082042. URL https://doi.org/10.1177/0278364907082042.

Ivan Dryanovski, Roberto G. Valenti, and Jizhong Xiao. Fast visual odometry and mapping from rgb-d data. In *2013 IEEE International Conference on Robotics and Automation*, pages 2305–2310, May 2013. doi: 10.1109/ICRA.2013.6630889.

Qiang Du and Max Gunzburger. Grid generation and optimization based on centroidal voronoi tessellations. *Applied Mathematics and Computation*, 133(2):591–607, 2002. ISSN 0096-3003. doi: https://doi.org/10.1016/S0096-3003(01)00260-0. URL https://www.sciencedirect.com/science/article/pii/S0096300301002600.

Guillermo Duenasarana, Mathieu Joerger, and Matthew Spenko. Local nearest neighbor integrity risk evaluation for robot navigation. In *Proceedings - IEEE International Conference on Robotics and Automation*, 2018. doi: 10.1109/ICRA.2018.8460762.

Alberto Elfes. Using occupancy grids for mobile robot perception and navigation. *Computer*, 22, 1989. ISSN 00189162. doi: 10.1109/2.30720.

Carlos Estrada, José Neira, and Juan D. Tardós. Hierarchical slam: Real-time accurate mapping of large environments. *IEEE Transactions on Robotics*, 21, 2005. ISSN 15523098. doi: 10.1109/TRO.2005.844673.

Hongqi Fan, Tomasz Piotr Kucner, Martin Magnusson, Tiancheng Li, and Achim J. Lilienthal. A dual phd filter for effective occupancy filtering in a highly dynamic environment. *IEEE Transactions on Intelligent Transportation Systems*, 19(9):2977–2993, 2018. doi: 10.1109/TITS.2017.2770152.

Robert Gallager and Lizhong Zheng. Principles of digital communications I. https://ocw.mit.edu/courses/6-450-principles-of-digital-communications-i-fall-2006/, 2006.

Omar Garcia Crespillo. *GNSS/INS Kalman Filter Integrity Monitoring with Uncertain Time Correlated Error Processes*. Doctoral dissertation, EPFL, 2022. URL http://infoscience.epfl.ch/record/292087.

J.E. Guivant and E.M. Nebot. Optimization of the simultaneous localization and map-building

algorithm for real-time implementation. *IEEE Transactions on Robotics and Automation*, 17 (3):242–257, 2001. doi: 10.1109/70.938382.

Jose Guivant, Eduardo Nebot, and Stephan Baiker. Localization and map building using laser range sensors in outdoor applications. *Journal of Robotic Systems*, 17, 2000. ISSN 07412223. doi: 10.1002/1097-4563(200010)17:10<565::AID-ROB4>3.0.CO;2-6.

Yulan Guo, Ferdous Sohel, Mohammed Bennamoun, Jianwei Wan, and Min Lu. An accurate and robust range image registration algorithm for 3d object modeling. *IEEE Transactions on Multimedia*, 16(5):1377–1390, 2014. doi: 10.1109/TMM.2014.2316145.

Osama Abdul Hafez, Guillermo Duenas Arana, Mathieu Joerger, and Matthew Spenko. Quantifying robot localization safety: A new integrity monitoring method for fixed-lag smoothing. *IEEE Robotics and Automation Letters*, 5, 2020. ISSN 23773766. doi: 10.1109/LRA.2020.2975769.

Jaehyun Han, Dongchul Kim, Minchae Lee, and Myoungho Sunwoo. Enhanced road boundary and obstacle detection using a downward-looking lidar sensor. *IEEE Transactions on Vehicular Technology*, 61, 2012. ISSN 00189545. doi: 10.1109/TVT.2012.2182785.

Ali Hassani and Mathieu Joerger. A new point-cloud-based lidar/imu localization method with uncertainty evaluation. In *Proceedings of the 34th International Technical Meeting of the Satellite Division of the Institute of Navigation, ION GNSS+ 2021*, pages 636 – 651, September 2021. doi: 10.33012/2021.17905.

Ali Hassani, Mathieu Joerger, Guillermo Duenas Arana, and Matthew Spenko. Lidar data association risk reduction using tight integration with ins. In *Proceedings of the 31st International Technical Meeting of the Satellite Division of the Institute of Navigation, ION GNSS+ 2018*, pages 2467–2483, September 2018. doi: 10.33012/2018.15976.

Ali Hassani, Nicholas Morris, Matthew Spenko, and Mathieu Joerger. Experimental integrity evaluation of tightly-integrated IMU/LiDAR including return-light intensity data. In *Proceedings of the 32nd International Technical Meeting of the Satellite Division of the Institute of Navigation, ION GNSS+ 2019*, pages 2637–2658, September 2019. doi: 10.33012/2019.17095.

Hong He, Kai Wang, and Lei Sun. A slam algorithm of fused ekf and particle filter. In *2018 WRC Symposium on Advanced Robotics and Automation (WRC SARA)*, pages 172–177, August 2018. doi: 10.1109/WRC-SARA.2018.8584219.

Wolfgang Hess, Damon Kohler, Holger Rapp, and Daniel Andor. Real-time loop closure in 2d lidar slam. In *2016 IEEE International Conference on Robotics and Automation (ICRA)*, pages 1271–1278, May 2016. doi: 10.1109/ICRA.2016.7487258.

Andinet Hunde and Beshah Ayalew. Automated multi-target tracking in public traffic in the presence of data association uncertainty. In *2018 Annual American Control Conference (ACC)*, pages 300–306, June 2018. doi: 10.23919/ACC.2018.8431852.

International Civil Aviation Organization. *Annex 10 to the Convention on International Civil Aviation Aeronautical Telecommunications, Radio Navigation Aids*, volume 1. ICAO, 6 edition, 2006. ISBN 5149548022.

Michael B. Jamoom, Mathieu Joerger, and Boris Pervan. Uas sense and avoid integrity and continuity for multiple intruders. In *Proceedings of the IEEE/ION Position, Location and Navigation Symposium, PLANS 2016*, 2016. doi: 10.1109/PLANS.2016.7479767.

Shau Shiun Jan and Yu Chun Kao. Radar tracking with an interacting multiple model and probabilistic data association filter for civil aviation applications. *Sensors (Switzerland)*, 13, 2013. ISSN 14248220. doi: 10.3390/s130506636.

Mathieu Joerger. *Carrier phase GPS augmentation using laser scanners and using low earth orbiting satellites*. Doctoral dissertation, Illinois Institute of Technology, 2009. URL https://www.proquest.com/docview/304898652?parentSessionId=FTJe%2FFsQQeE1mbVECg02TsE5CTCncFGMuML8LcxX9Xs%3D.

Mathieu Joerger and Ali Hassani. A new data association method using kalman filter innovation vector projections. In *2020 IEEE/ION Position, Location and Navigation Symposium (PLANS)*, pages 318–327, April 2020. doi: 10.1109/PLANS46316.2020.9110229.

Mathieu Joerger and Boris Pervan. Measurement-Level Integration of Carrier-Phase GPS and Laser-Scanner for Outdoor Ground Vehicle Navigation. *Journal of Dynamic Systems, Measurement, and Control*, 131(2), 2009. ISSN 0022-0434. doi: 10.1115/1.3072122. 021004.

Mathieu Joerger and Boris Pervan. Continuity risk of feature extraction for laser-based navigation. In *Proceedings of the 2017 International Technical Meeting of The Institute of Navigation*, pages 839–855, September 2017.

Mathieu Joerger and Boris Pervan. Quantifying safety of laser-based navigation. *IEEE Transactions on Aerospace and Electronic Systems*, 55(1):273–288, 2019. doi: 10.1109/TAES.2018.2850381.

Mathieu Joerger, Michael Jamoom, Matthew Spenko, and Boris Pervan. Integrity of laser-based feature extraction and data association. In *2016 IEEE/ION Position, Location and Navigation Symposium (PLANS)*, pages 557–571, April 2016. doi: 10.1109/PLANS.2016.7479746.

Mathieu Joerger, Guillermo Duenas Arana, Matthew Spenko, and Boris Pervan. Landmark data selection and unmapped obstacle detection in lidar-based navigation. In *30th International Technical Meeting of the Satellite Division of the Institute of Navigation, ION GNSS+ 2017*, volume 3, pages 1886–1903, September 2017. doi: 10.33012/2017.15406.

Mathieu Joerger, Guillermo Duenas Arana, Matthew Spenko, and Boris Pervan. A new approach to unwanted-object detection in gnss/lidar-based navigation. *Sensors (Switzerland)*, 18, 2018. ISSN 14248220. doi: 10.3390/s18082740.

Nidhi Kalra and David G. Groves. *The Enemy of Good: Estimating the Cost of Waiting for Nearly Perfect Automated Vehicles*. RAND Corporation, Santa Monica, CA, 2017. doi: 10.7249/RR2150.

Nidhi Kalra and Susan M. Paddock. Driving to safety: How many miles of driving would it take to demonstrate autonomous vehicle reliability? *Transportation Research Part A: Policy and Practice*, 94:182–193, 2016. ISSN 0965-8564. doi: https://doi.org/10.1016/j.tra.2016.09.010. URL https://www.sciencedirect.com/science/article/pii/S0965856416302129.

Gustavo Lee and Mathieu Joerger. Integrity and continuity of sensor-based collision warning systems using vehicle-to-vehicle communication. In *2018 IEEE/ION Position, Location and Navigation Symposium, PLANS 2018 - Proceedings*, 2018. doi: 10.1109/PLANS.2018.8373487.

John J. Leonard and Hugh F. Durrant-Whyte. *Directed Sonar Sensing for Mobile Robot Navigation*. Springer, 1992. doi: 10.1007/978-1-4615-3652-9.

John J Leonard and Hans Jacob S Feder. A computationally efficient method for large-scale concurrent mapping and localization. In *Robotics Research*, pages 169–176. Springer, 2000. doi: 10.1007/978-1-4471-0765-1{_}21.

Zhao Li, Stan E. Dosso, and Dajun Sun. Motion-compensated acoustic localization for underwater vehicles. *IEEE Journal of Oceanic Engineering*, 41, 2016. ISSN 03649059. doi: 10.1109/JOE.2015.2503518.

F. Lu and E. Milios. Globally consistent range scan alignment for environment mapping. *Autonomous Robots*, 4, 1997. ISSN 09295593. doi: 10.1023/A:1008854305733.

Zhongzhen Luo, Martin V. Mohrenschildt, and Saeid Habibi. A probability occupancy grid based approach for real-time lidar ground segmentation. *IEEE Transactions on Intelligent Transportation Systems*, 21(3):998–1010, 2020. doi: 10.1109/TITS.2019.2900548.

Vijay K Madisetti. *The Digital Signal Processing Handbook-3 Volume Set*. CRC press, 2018.

Ronald P S Mahler and Lockheed Martin. Multitarget bayes filtering via first-order multitarget moments. *IEEE TRANSACTIONS ON AEROSPACE AND ELECTRONIC SYSTEMS*, 39, 2003. doi: 10.1109/TAES.2003.1261119.

D. Maksarov and H. Durrant-Whyte. Mobile vehicle navigation in unknown environments: a multiple hypothesis approach. *IEE Proceedings: Control Theory and Applications*, 142, 1995. ISSN 13502379. doi: 10.1049/ip-cta:19951872.

J. Max. Quantizing for minimum distortion. *IRE Transactions on Information Theory*, 6(1): 7–12, 1960. doi: 10.1109/TIT.1960.1057548.

Qingyu Meng, Hongyan Guo, Xiaoming Zhao, Dongpu Cao, and Hong Chen. Loop-closure detection with a multiresolution point cloud histogram mode in lidar odometry and mapping for intelligent vehicles. *IEEE/ASME Transactions on Mechatronics*, 26, 2021. ISSN 1941014X. doi: 10.1109/TMECH.2021.3062647.

Michael Montemerlo and Sebastian Thrun. Simultaneous localization and mapping with unknown data association using fastslam. In *2003 IEEE International Conference on Robotics and Automation (ICRA)*, volume 2, pages 1985–1991, November 2003. doi: 10.1109/ROBOT.2003.1241885.

John Mullane, Ba Ngu Vo, Martin D. Adams, and Wijerupage Sardha Wijesoma. A random set formulation for bayesian slam. In *2008 IEEE/RSJ International Conference on Intelligent Robots and Systems, IROS*, 2008. doi: 10.1109/IROS.2008.4650815.

John Mullane, Ba Ngu Vo, Martin D. Adams, and Ba Tuong Vo. A random-finite-set approach to bayesian slam. *IEEE Transactions on Robotics*, 27, 2011. ISSN 15523098. doi: 10.1109/TRO.2010.2101370.

Esha D Nerurkar and Stergios I Roumeliotis. Power-slam: a linear-complexity, anytime algorithm for slam. *The International Journal of Robotics Research*, 30(6):772–788, 2011. doi: 10.1177/0278364910390539.

Dominik Nuss, Ting Yuan, Gunther Krehl, Manuel Stuebler, Stephan Reuter, and Klaus Dietmayer. Fusion of laser and radar sensor data with a sequential monte carlo bayesian occupancy filter. In *2015 IEEE Intelligent Vehicles Symposium (IV)*, pages 1074–1081, August 2015. doi: 10.1109/IVS.2015.7225827.

Aníbal Ollero, Joaquín Ferruz, Fernando Caballero, Sebastián Hurtado, and Luis Merino. Motion compensation and object detection for autonomous helicopter visual navigation in the comets system. In *Proceedings - IEEE International Conference on Robotics and Automation*, volume 2004, 2004. doi: 10.1109/robot.2004.1307123.

Roberto Opromolla, Giancarmine Fasano, Giancarlo Rufino, Michele Grassi, and Al Savvaris. Lidar-inertial integration for uav localization and mapping in complex environments. In *2016 International Conference on Unmanned Aircraft Systems (ICUAS)*, pages 649–656, June 2016. doi: 10.1109/ICUAS.2016.7502580.

Laura Pirovano, Gennaro Principe, and Roberto Armellin. Data association and uncertainty pruning for tracks determined on short arcs. *Celestial Mechanics and Dynamical Astronomy*, 132(1):1–23, 2020.

François Pomerleau, Francis Colas, Roland Y. Siegwart, and Stéphane Magnenat. Comparing icp variants on real-world data sets. *Autonomous Robots*, 34:133–148, 2013. doi: 10.1007/s10514-013-9327-2.

Gheorghii Postica, Andrea Romanoni, and Matteo Matteucci. Robust moving objects detection in lidar data exploiting visual cues. In *IEEE International Conference on Intelligent Robots and Systems*, volume 2016-November, 2016. doi: 10.1109/IROS.2016.7759185.

Sam Pullen and Mathieu Joerger. *Position, Navigation, and Timing Technologies in the 21st Century: Integrated Satellite Navigation, Sensor Systems, and Civil Applications*, volume 1, chapter GNSS Integrity and Receiver Autonomous Integrity Monitoring (RAIM), pages 591–617. John Wiley, 2020. doi: 10.1002/9781119458449.ch23.

Radio Technical Commission for Aeronautics (RTCA) Special Committee 159. Minimum Operational Performance Standards for Global Positioning System/Wide Area Augmentation System Airborne Equipment, 2006. URL https://www.techstreet.com/standards/rtca-do-229d?product_id=2200871.

Radio Technical Commission for Aeronautics (RTCA) Special Committee 159. Minimum operational performance standards for gps local area augmentation system airborne equipment, 2007. URL https://www.techstreet.com/standards/rtca-do-253b?product_id=2200903#jumps.

Akshay Rangesh and Mohan Manubhai Trivedi. No blind spots: Full-surround multi-object tracking for autonomous vehicles using cameras and lidars. *IEEE Transactions on Intelligent Vehicles*, 4, 2019. ISSN 23798858. doi: 10.1109/TIV.2019.2938110.

Tyler GR Reid, Sarah E Houts, Robert Cammarata, Graham Mills, Siddharth Agarwal, Ankit Vora, and Gaurav Pandey. Localization requirements for autonomous vehicles. *arXiv preprint arXiv:1906.01061*, 2019. doi: 10.4271/12-02-03-0012.

A. Reina and J. Gonzales. Characterization of a radial laser scanner for mobile robot navigation. In *Proceedings of the 1997 IEEE/RSJ International Conference on Intelligent Robot and Systems. Innovative Robotics for Real-World Applications (IROS)*, volume 2, pages 579–585 vol.2, September 1997. doi: 10.1109/IROS.1997.655070.

J. Rife, S. Pullen, P. Enge, and B. Pervan. Paired overbounding for nonideal LAAS and WAAS error distributions. *IEEE Transactions on Aerospace and Electronic Systems*, 42(4):1386–1395, 2006.

Robert M Rogers. *Applied mathematics in integrated navigation systems*, volume 1. American Institute of Aeronautics and Astronautics (AIAA), third edition, 2007. doi: 10.2514/4.861598.

I. T. Ruiz, Y. Petillot, D. M. Lane, and C. Salson. Feature extraction and data association for auv concurrent mapping and localisation. In *Proceedings of IEEE International Conference on Robotics and Automation (ICRA)*, volume 3, pages 2785–2790, May 2001. doi: 10.1109/robot.2001.933044.

Szymon M. Rusinkiewicz and Marc Levoy. Efficient variants of the icp algorithm. In *Proceedings Third International Conference on 3-D Digital Imaging and Modeling*, pages 145–152, May 2001.

Thomas Röfer. Using histogram correlation to create consistent laser scan maps. In *IEEE International Conference on Intelligent Robots and Systems*, volume 1, 2002. doi: 10.1109/irds.2002.1041461.

M. Sabin and R. Gray. Global convergence and empirical consistency of the generalized lloyd algorithm. *IEEE Transactions on Information Theory*, 32(2):148–155, 1986. doi: 10.1109/TIT.1986.1057168.

A Sappa, Andres Restrepo-Specht, and Michel Devy. Range image registration by using an

edge-based representation. In *Proceedings of th 9th International Symposium on Intelligent Robotic Systems (SIRS)*, volume 7, pages 167–176, January 2001.

S. Sato, M. Hashimoto, M. Takita, K. Takagi, and T. Ogawa. Multilayer lidar-based pedestrian tracking in urban environments. In *IEEE Intelligent Vehicles Symposium, Proceedings*, 2010. doi: 10.1109/IVS.2010.5548135.

Khalid Sayood. *Introduction to data compression*. Morgan Kaufmann, 2017.

Andrey Soloviev. Tight coupling of GPS, laser scanner, and inertial measurements for navigation in urban environments. In *2008 IEEE/ION Position, Location and Navigation Symposium (PLANS)*, pages 511–525, May 2008. doi: 10.1109/PLANS.2008.4570059.

Andrey Soloviev, Dustin Bates, and Frank Van Graas. Tight coupling of laser scanner and inertial measurements for a fully autonomous relative navigation solution. *Navigation, Journal of the Institute of Navigation*, 54, 2007. ISSN 00281522. doi: 10.1002/j.2161-4296.2007.tb00404.x.

Çaatay Tanl, Samer Khanafseh, Mathieu Joerger, and Boris Pervan. An ins monitor to detect gnss spoofers capable of tracking vehicle position. *IEEE Transactions on Aerospace and Electronic Systems*, 54(1):131–143, 2018. doi: 10.1109/TAES.2017.2739924.

Sebastian Thrun. Robotic mapping: A survey. *Science*, 298, 2002. ISSN 00368075.

Sebastian Thrun, Wolfram Burgard, and Dieter Fox. A probabilistic approach to concurrent mapping and localization for mobile robots. *Machine Learning and Autonomous Robots (joint issue)*, 31:29–53, 1998. ISSN 09295593. doi: 10.1023/a:1008806205438.

David Titterton, John L Weston, and John Weston. *Strapdown inertial navigation technology*, volume 17. The Institute of Engineering and Technology (IET), 2004.

U.S. DOT FHWA. Vehicle positioning trade study for its applications, 2017. URL https://highways.dot.gov/research/projects/vehicle-positioning-systems-trade-study-connected-vehicle-program-applications.

U.S. DOT NHTSA. Automated driving systems 2.0: A vision for safety, 2017. URL https://www.nhtsa.gov/sites/nhtsa.gov/files/documents/13069a-ads2.0_090617_v9a_tag.pdf.

Ba Ngu Vo and Wing Kin Ma. The gaussian mixture probability hypothesis density filter. *IEEE Transactions on Signal Processing*, 54, 2006. ISSN 1053587X. doi: 10.1109/TSP.2006.881190.

G. Vosselman and S. Dijkman. 3d building model reconstruction from point clouds and ground plans. In *Proceedings of the International Society for Photogrammetry and Remote Sensing (ISPRS) Workshop*, volume XXXIV-3/W4, pages 37–43, January 2001.

Stefan B. Williams, Gamini Dissanayake, and Hugh Durrant-Whyte. An efficient approach to the simultaneous localisation and mapping problem. In *Proceedings - IEEE International Conference on Robotics and Automation*, volume 1, 2002. doi: 10.1109/robot.2002.1013394.

Working Group C. ARAIM Technical Subgroup, Milestone 3 Report. Technical report, EU-US Cooperation on Satellite Navigation, 2016.

Cang Ye and J. Borenstein. Characterization of a 2d laser scanner for mobile robot obstacle negotiation. In *Proceedings 2002 IEEE International Conference on Robotics and Automation (ICRA)*, volume 3, pages 2512–2518, August 2002. doi: 10.1109/ROBOT.2002.1013609.

Bo Zheng and Zexu Zhang. An improved ekf-slam for mars surface exploration. *International Journal of Aerospace Engineering*, 2019, 2019. doi: https://doi.org/10.1155/2019/7637469.

Chen Zhu, Mathieu Joerger, and Michael Meurer. Quantifying feature association error in

camera-based positioning. In *2020 IEEE/ION Position, Location and Navigation Symposium, PLANS 2020*, 2020. doi: 10.1109/PLANS46316.2020.9109919.

Appendices

A - IMU and LiDAR Measurements and Coefficients

The IMU measurement coefficient matrices in equation (2.14) are defined as [Titterton et al. (2004)]:

$$\mathbf{F}_{\text{V2T}} = \begin{bmatrix} 0 & \frac{1}{R+h} & 0 \\ \frac{1}{R+h} & 0 & 0 \\ 0 & \frac{-\tan(\lambda)}{R+h} & 0 \end{bmatrix} \tag{1}$$

$$\mathbf{F}_{\text{H2V}} = \begin{bmatrix} 0 & 0 & 0 \\ 0 & 0 & 0 \\ 0 & 0 & \frac{2g_0}{R} \end{bmatrix} \tag{2}$$

where

R is the earths radius,

h is the vehicles altitude,

λ is the vehicles latitude,

g_0 is the acceleration of gravity at zero altitude.

The LiDAR measurement coefficient matrices in equations (2.17) and (4.19) are [Joerger (2009)]:

$$\mathbf{F}_{d,x} = \begin{bmatrix} -\frac{{}^{1}p_E - x_E}{\|{}^{1}\mathbf{p} - \bar{\mathbf{x}}_{EN}\|} & \cdots & -\frac{{}^{n_L}p_E - x_E}{\|{}^{n_L}\mathbf{p} - \bar{\mathbf{x}}_{EN}\|} \\ -\frac{{}^{1}p_N - x_N}{\|{}^{1}\mathbf{p} - \bar{\mathbf{x}}_{EN}\|} & \cdots & -\frac{{}^{n_L}p_N - x_N}{\|{}^{n_L}\mathbf{p} - \bar{\mathbf{x}}_{EN}\|} \\ 0 & \cdots & 0 \end{bmatrix}^{\text{T}}_{n_L \times 3}, \quad \mathbf{F}_{r,x} = \begin{bmatrix} -\frac{{}^{\text{N}}p_{E,1} - x_E}{\|{}^{\text{N}}\mathbf{p}_1 - \bar{\mathbf{x}}_{EN}\|} & \cdots & -\frac{{}^{\text{N}}p_{E,m} - x_E}{\|{}^{\text{N}}\mathbf{p}_m - \bar{\mathbf{x}}_{EN}\|} \\ -\frac{{}^{\text{N}}p_{N,1} - x_N}{\|{}^{\text{N}}\mathbf{p}_1 - \bar{\mathbf{x}}_{EN}\|} & \cdots & -\frac{{}^{\text{N}}p_{N,m} - x_N}{\|{}^{\text{N}}\mathbf{p}_m - \bar{\mathbf{x}}_{EN}\|} \\ 0 & \cdots & 0 \end{bmatrix}^{\text{T}}_{m \times 3} \tag{3}$$

$$\mathbf{F}_{a,x} = \begin{bmatrix} \frac{{}^{1}p_N - x_N}{\|{}^{1}\mathbf{p} - \bar{\mathbf{x}}_{EN}\|^2} & \cdots & \frac{{}^{n_L}p_N - x_N}{\|{}^{n_L}\mathbf{p} - \bar{\mathbf{x}}_{EN}\|^2} \\ -\frac{{}^{1}p_E - x_E}{\|{}^{1}\mathbf{p} - \bar{\mathbf{x}}_{EN}\|^2} & \cdots & -\frac{{}^{n_L}p_E - x_E}{\|{}^{n_L}\mathbf{p} - \bar{\mathbf{x}}_{EN}\|^2} \\ 0 & \cdots & 0 \end{bmatrix}^{\mathrm{T}}_{n_L \times 3} \quad \mathbf{F}_{\theta,x} = \begin{bmatrix} \frac{{}^{\mathrm{N}}p_{N,1} - x_N}{\|{}^{\mathrm{N}}\mathbf{p}_1 - \bar{\mathbf{x}}_{EN}\|^2} & \cdots & \frac{{}^{\mathrm{N}}p_{N,m} - x_N}{\|{}^{\mathrm{N}}\mathbf{p}_m - \bar{\mathbf{x}}_{EN}\|^2} \\ -\frac{{}^{\mathrm{N}}p_{E,1} - x_E}{\|{}^{\mathrm{N}}\mathbf{p}_1 - \bar{\mathbf{x}}_{EN}\|^2} & \cdots & -\frac{{}^{\mathrm{N}}p_{E,m} - x_E}{\|{}^{\mathrm{N}}\mathbf{p}_m - \bar{\mathbf{x}}_{EN}\|^2} \\ 0 & \cdots & 0 \end{bmatrix}^{\mathrm{T}}_{m \times 3} \tag{4}$$

$$\mathbf{F}_{a,e} = \mathbf{F}_{\theta,e} = \begin{bmatrix} 0 & 0 & 1 \\ & \cdots & \\ 0 & 0 & 1 \end{bmatrix}^{\mathrm{T}}_{(n_L \, or \, m) \times 3} \tag{5}$$

where $\bar{\mathbf{x}}_{EN} = \begin{bmatrix} x_E & x_N \end{bmatrix}^{\mathrm{T}}$ and $\mathbf{p} = {}^{\mathrm{N}}\mathbf{p} = \begin{bmatrix} p_E & p_N \end{bmatrix}^{\mathrm{T}}$

B - Discrete-Time Equations of IMU

The ADS specific force is measured with respect to the inertial frame I and expressed in body frame B as ${}^{\mathrm{B}}\mathbf{f}$. The specific force measurement is imperfect: it can be modeled in the continuous-time domain as:

$${}^{\mathrm{B}}\tilde{\mathbf{f}} = [\mathbf{I} + \mathbf{S}_{ac} + \mathbf{M}_{ac}]{}^{\mathrm{B}}\mathbf{f} + \mathbf{b}_{ac} + \boldsymbol{\nu}_{ac} \tag{6}$$

where

${}^{B}\mathbf{f}$ is the 3×1 true specific force vector of body B with respect to I expressed in body frame B,

${}^{B}\tilde{\mathbf{f}}$ is the measured specific force vector of body B with respect to I expressed in B,

$\mathbf{S}_{ac}, \mathbf{M}_{ac}$ are the true accelerometer calibration scale factor and misalignment matrices in B,

$\mathbf{b}_{ac}$ is the accelerometer time-varying bias vector in B,

$\boldsymbol{\nu}_{ac}$ is accelerometer measurement white noise error component expressed in B.

In equation 6, the measured specific force ${}^{B}\tilde{\mathbf{f}}$ is expressed in terms of the scale factor and misalignment matrices for which manufacturers provide estimates $\hat{\mathbf{S}}_{ac}$ and $\hat{\mathbf{M}}_{ac}$, respectively. The symbol ($\hat{}$) in $\hat{\mathbf{S}}_{ac}$ designates the estimate of parameter $\mathbf{S}$.

The accelerometer time-varying bias is modeled as a first order Gauss-Markov process (GMP) [Brown and Hwang (1992)]. We can write the corrected specific force ${}^{B}\bar{\mathbf{f}}$ and the continuous-time dynamics of the time-varying bias as:

$$ {}^{B}\bar{\mathbf{f}} = [\mathbf{I} + \hat{\mathbf{S}}_{ac} + \hat{\mathbf{M}}_{ac}]^{-1}({}^{B}\tilde{\mathbf{f}} - \hat{\mathbf{b}}_{ac}) \tag{7} $$

$$ \dot{\mathbf{b}}_{ac} = -\frac{1}{\tau_{ac}}\mathbf{b}_{ac} + \mathbf{n}_{ac} \tag{8} $$

where

τ_{ac} is the GMP time constant,

$\mathbf{n}_{ac}$ is a 3×1 vector of GMP time-uncorrelated driving noise.

The discrete form of equations (6-8) can be written as:.

$$^{\mathrm{B}}\tilde{\mathbf{f}}_k = [\mathbf{I} + \mathbf{S}_{ac} + \mathbf{M}_{ac}]^{\mathrm{B}}\mathbf{f}_k + \mathbf{b}_{ac,k} + \boldsymbol{\nu}_{ac,k} \tag{9}$$

$$^{\mathrm{B}}\bar{\mathbf{f}}_k = [\mathbf{I} + \hat{\mathbf{S}}_{ac} + \hat{\mathbf{M}}_{ac}]^{-1}(^{\mathrm{B}}\tilde{\mathbf{f}}_k - \hat{\mathbf{b}}_{ac,k}) \tag{10}$$

$$\mathbf{b}_{ac,k+1} = e^{-\frac{t_s}{\tau_{ac}}}\mathbf{b}_{ac,k} + \mathbf{n}_{ac,k} \tag{11}$$

where

t_s is the IMU sampling interval.

The gyroscope measures the body frame angular velocity with respect to the inertial frame and can be expressed in the body frame as $^{\mathrm{B}}\tilde{\boldsymbol{\omega}}^{\mathrm{IB}}$ [Titterton et al. (2004)]. We can derive equations similar to (7)-(11) for gyro measurements. These are given in [Hassani et al. (2019)].

Assuming that the IMU corrected specific force $^{\mathrm{B}}\bar{\mathbf{f}}$ and angular velocity $^{\mathrm{B}}\bar{\boldsymbol{\omega}}^{\mathrm{IB}}$ remain constant over the short IMU sampling interval t_s, between time steps $k-1$ and k, we can write the discrete-time form of equations (2.1) to (2.3) and the attitude equations as:

$$^{\mathrm{N}}\mathbf{v}^{\mathrm{E}}_{ADS,k} = {}^{\mathrm{N}}\mathbf{u} - (2[^{\mathrm{N}}\boldsymbol{\omega}^{\mathrm{IE}}\times]\,t_s + [^{\mathrm{N}}\boldsymbol{\omega}^{\mathrm{EN}}\times]\,t_s) \times {}^{\mathrm{N}}\mathbf{v}^{\mathrm{E}}_{ADS,k} + {}^{\mathrm{N}}\mathbf{g}\,t_s \tag{12}$$

$$^{\mathrm{N}}\mathbf{x}_{ADS,k} = {}^{\mathrm{N}}\mathbf{x}_{ADS,k-1} + \frac{^{\mathrm{N}}\mathbf{v}^{\mathrm{E}}_{ADS,k-1} + {}^{\mathrm{N}}\mathbf{v}^{\mathrm{E}}_{ADS,k}}{2}\,t_s \tag{13}$$

$$\mathbf{C}^{\mathrm{N}}_{\mathrm{B},k} = \mathbf{C}^{\mathrm{N}}_{\mathrm{B},k-1}\,\mathbf{B}_{k-1} \tag{14}$$

$$\mathbf{e}_{ADS,k} = \begin{cases} \dot{\phi}_k = \arctan\left(\frac{\mathbf{C}^{\mathrm{N}}_{\mathrm{B},k-1}(3,2)}{\mathbf{C}^{\mathrm{N}}_{\mathrm{B},k-1}(3,3)}\right) \\ \dot{\theta}_k = \arctan\left(\mathbf{C}^{\mathrm{N}}_{\mathrm{B},k-1}(3,1)\right) \\ \dot{\psi}_k = \arctan\left(\frac{\mathbf{C}^{\mathrm{N}}_{\mathrm{B},k-1}(2,1)}{\mathbf{C}^{\mathrm{N}}_{\mathrm{B},k-1}(1,1)}\right) \end{cases} \tag{15}$$

where

$${}^{\mathrm{N}}\mathbf{u} = \mathbf{C}^{\mathrm{N}}_{\mathrm{B},k-1}({}^{\mathrm{B}}\bar{\mathbf{f}}_k\, t_s + 0.5[{}^{\mathrm{B}}\bar{\boldsymbol{\omega}}^{\mathrm{IB}}_k\times]{}^{\mathrm{B}}\bar{\mathbf{f}}_k\, {t_s}^2)$$

$$\mathbf{B}_{k-1} = \mathbf{I} + [{}^{\mathrm{B}}\bar{\boldsymbol{\omega}}^{\mathrm{IB}}_k\times]t_s$$

The notation $\mathbf{C}^{\mathrm{N}}_{\mathrm{B},k-1}(i,j)$ in equation (15) designates the (i,j)th scalar component of matrix $\mathbf{C}^{\mathrm{N}}_{\mathrm{B},k-1}$, i.e., the component in the ith row and jth column.

Finally, we use the Van Loan algorithm to determine the discrete-time state propagation $\mathbf{\Phi}_{k-1}$ and process noise covariance matrices $\mathbf{W}_{k-1}$ based on the continuous-time matrices $\mathbf{F}$ and spectral density function of $\delta\mathbf{w}$, defined as $\mathbf{Q}$ [Brown and Hwang (1992)].

C - Overbounding of Measurement Error Distributions

This appendix describes a method to derive probabilistic models of the extracted feature measurements. This method is based on overbounding theory in [DeCleene (2000)]. Overbounding theory is used in aviation navigation to model non-Gaussian sample distributions, even where they are not symmetric, not unimodal, and not zero mean [Rife et al. (2006), Blanch et al. (2019)]. We collected LiDAR PC data for 4250 sensor-to-landmark geometries, processed them using our feature extractor, and stored the estimated point-feature range and bearing

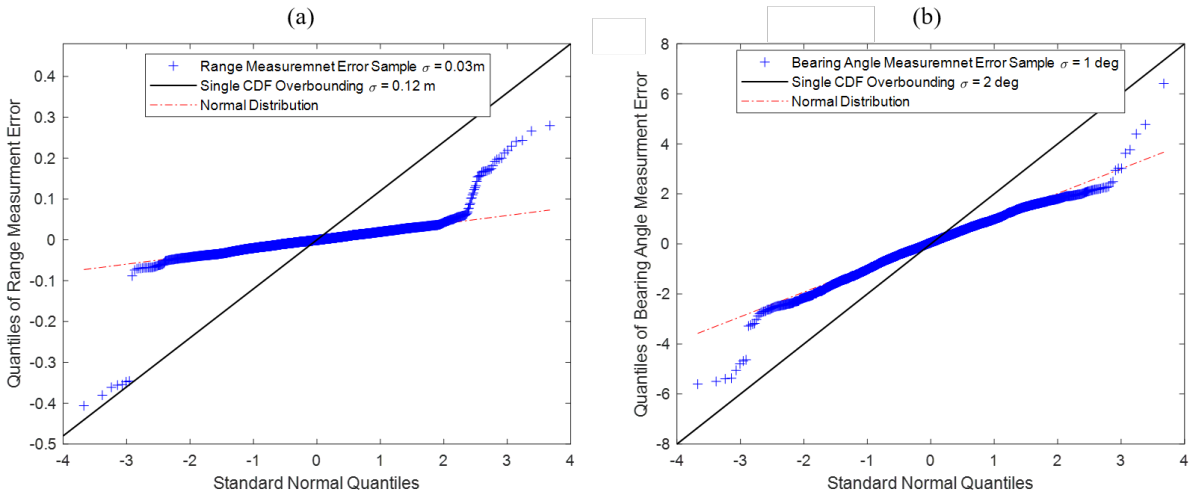

Figure C.1: Quantile-to-Quantile Plots of the LiDAR PC's Extracted Feature Error Distribution and Gaussian Overbounding Model for the (a) Range Measurement (b) Bearing Angle Measurement (4250 data points)

angle measurements. Figure C.1 shows the range and bearing angle measurement error CDF on quantile-to-quantile plots. The plots x-axis scales with theoretical standard normal distribution quantiles. The y-axis scales with the sample measurement error distribution quantiles. If the empirical measurement error distribution were a normal distribution, the sample points would lie on a straight line with a slope equal to the sample standard deviation, and with the y-intercept equal to the sample mean. Figure C.1 shows that the core of the distribution behaves like a normal distribution within $\pm 2\sigma$ on the x-axis, i.e., 95% of the time. However the sample distributions have wide tails. The black lines in Figure C.1 are overbounding Gaussian functions which account for errors occurring 99.5% of the time, i.e., out to '3σ'. The bounding standard deviations are 0.12 m for the range measurement error (versus 0.03 m for the sample standard deviation), and 2° for the bearing angle measurement error (versus 1° for the sample standard deviation). Thus, Gaussian overbounds are conservative as compared to sample measurement error distributions, which will impact the pose estimation error distribution.

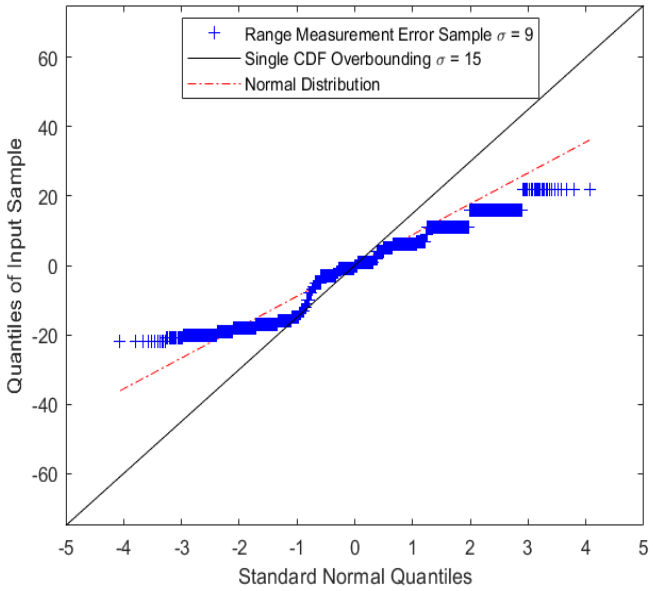

Figure D.1: Intensity Measurement Error Distribution and Gaussian Overbounding Model for the Retro-Reflective Surface with a 70-Degree Incidence Angle (17,500 data points)

D - LiDAR intensity measurements distribution

In this appendix, we follow the same methodology as in Appendix C to study the LiDAR intensity measurements error model. The return light intensity is a function of the object's surface property and of the light beam's incidence angle. The incidence angle is defined as the angle between the normal vector to the surface and the laser beam. Figure D.1 shows a quantile-to-quantile plot of 17,500 intensity samples of a retro-reflective object at a 70-degree incidence angle. This example is selected to illustrate the fact that overbounding theory can be used to define a Gaussian error models for discrete measurements of intensity.

Figure D.2 shows the mean values (thick lines) and standard deviations (thin lines, solid for 1σ envelopes, dashed for 3σ envelopes) of intensity measurement overbounding functions for three different surfaces at three different incidence angles. The mean values decrease with increasing incidence angle.

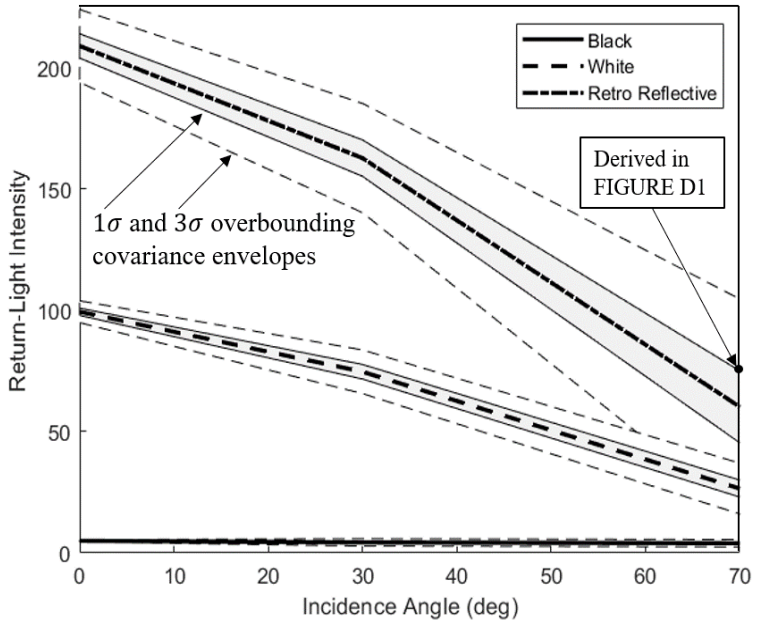

Figure D.2: Mean and Overbounding Standard Deviations ($\pm 1\sigma$ and $\pm 3\sigma$) of Intensity Measurements for Black, White and Retro-Reflective Surfaces at 0-Degree, 30-Degree, and 70-Degree Incidence Angles (total of 166,334 data points, approximately 18,480 data points per configuration over the nine configurations)

E - Time evolution of biases and estimator coefficients

In this Appendix, we study the time-dependent impact of the quantization biases on the a-posteriori estimation of the state vector at each timestep. This impact is governed by equations 4.21 and 4.22 which are rewritten below for better explanation.

$$\mathrm{E}[\mathbf{x}_k] = [\mathbf{A}_{1k} \quad \dots \quad \mathbf{A}_{kk}] \begin{bmatrix} \mathbf{b}_1 \\ \vdots \\ \mathbf{b}_k \end{bmatrix} = \mathbf{A}_{\mathrm{K}} \mathbf{b}_{\mathrm{K}} \tag{16}$$

where

$$\mathbf{A}_{mk} = \begin{Bmatrix} \left(\prod_{t=n}^{m+1} (\mathbf{I} + \mathbf{K}_n \mathbf{H}_n^{\mathrm{T}}) \hat{\mathbf{\Phi}}_{k,m} \right) \mathbf{K}_m, & \text{if } m < n \\ \mathbf{K}_m & \text{if } m = k \end{Bmatrix} \tag{17}$$

We are expanding equation 17 for a few timesteps (i.e. $k = 1, 2\ and\ 3$) to understand how the coefficients (weights) of a bias (i.e. $\mathbf{b}_1$ or $\mathbf{b}_2$ or $\mathbf{b}_3$) change by time. Tables in Figure E.1 show that the coefficients of each bias are a function of the current and past estimator parameters at each timestep. Figure E.2 shows the contribution of the past and current quantization biases on the current timestep (i.e. $k = 5$ and $k = 6$) cross-track error bound estimation with blue and red crosses. For example, the first and second blue crosses are the contribution of $\mathbf{b}_1$ and $\mathbf{b}_2$ on the cross-track error bound estimation at timestep $k = 5$. We can see the greatest contribution at each time step belongs to the quantization bias at the same timestep. Also, the summation of the contribution of all biases on the current cross-track error estimation is shown with blue and red circles. The gray curly bracket at timestep $k = 5$ demonstrates the reduction in the contribution of $\mathbf{b}_5$ on cross-track error bound estimation between timesteps $k = 5$ and $k = 6$.

Coefficients of $\mathbf{b}_1$

Timestep	$\mathbf{A}_{1k}$
$k=1$	$\mathbf{K}_1$
$k=2$	$(\mathbf{I}-\mathbf{K}_2\mathbf{H}_2)\widehat{\mathbf{\Phi}}_2\mathbf{K}_1$
$k=3$	$(\mathbf{I}-\mathbf{K}_3\mathbf{H}_3)\widehat{\mathbf{\Phi}}_3(\mathbf{I}-\mathbf{K}_2\mathbf{H}_2)\widehat{\mathbf{\Phi}}_2\mathbf{K}_1$

Coefficients of $\mathbf{b}_2$

Timestep	$\mathbf{A}_{2k}$
$k=1$	----------
$k=2$	$\mathbf{K}_2$
$k=3$	$(\mathbf{I}-\mathbf{K}_3\mathbf{H}_3)\widehat{\mathbf{\Phi}}_3\mathbf{K}_2$

Coefficients of $\mathbf{b}_3$

Timestep	$\mathbf{A}_{3k}$
$k=1$	----------
$k=2$	----------
$k=3$	$\mathbf{K}_3$

Figure E.1: Time variation of biases coefficients for the first three timesteps

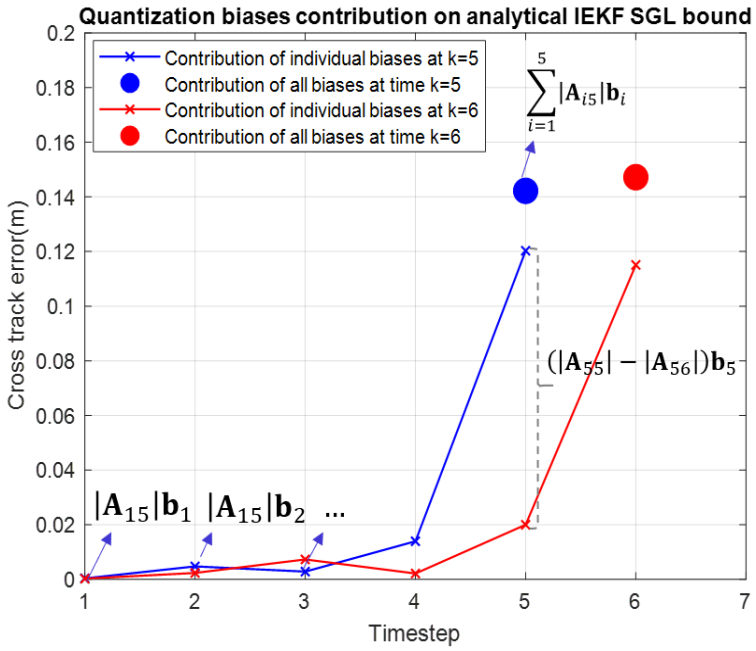

Figure E.2: Impact of previous and current quantization biases on IEKF SGL analytical cross track error bound

Figure E.3 shows the same curves as Figure E.2 for three well-seperated timesteps $k=10$, $k=100$ and $k=200$. This figure shows the weight of previous quantization biases decreases as time passes and only a few last biases are dominant in the error bound estimation. It is noteworthy that the contribution of biases is geometry and application dependent. In other words, a greater timestep is not necessarily equal to a greater contribution of biases due to accumulation, as we can see by comparing the blue and green circles.

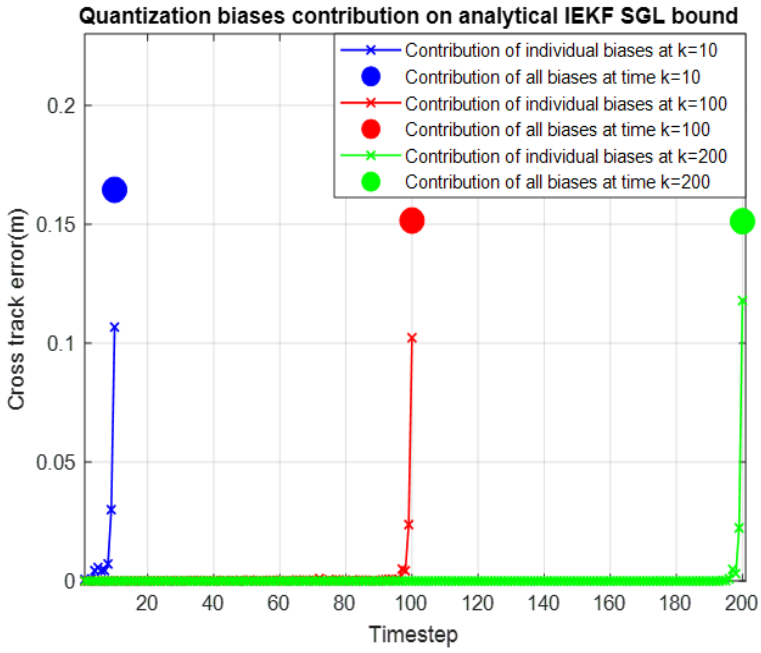

Figure E.3: Copmarison of the impact of quantization biases on IEKF SGL analytical cross track error bound